Science & Technology
Facilities Council

SCARF Annual Report 2016-2017

D Ross (editor)

July 2018

Enquiries concerning this report should be addressed to:

RAL Library
STFC Rutherford Appleton Laboratory
Harwell Oxford
Didcot
OX11 0QX

Tel: +44(0)1235 445384
Fax: +44(0)1235 446403
email: libraryral@stfc.ac.uk

Science and Technology Facilities Council reports are available online at: http://epubs.stfc.ac.uk

Neither the Council nor the Laboratory accept any responsibility for loss or damage arising from the use of information contained in any of their reports or in any communication about their tests or investigations.

SCARF Annual Report 2016-2017

Version: 1.0

Date: 19/07/2018

Edited by Derek Ross (derek.ross@stfc.ac.uk) 01235 445651

Content written by the respective authors

Date	Revision	Changes
24/11/17	0.1	Initial document
12/1/18	0.2	Inclusion of contributed science highlights
12/3/18	0.3	Draft for approval
13/7/18	1.0	Incorporate comments

Abstract

Annual Report on the Usage and Scientific Impact of the SCARF Service

Dissemination

This is a public document

1.   SCARF SERVICE

SCARF is a High Performance Cluster for STFC staff, Facilities (ISIS, DIAMOND, CLF) and their users. The SCARF Service was started in 2004 and has been upgraded year on year and now represents a significant capital investment in High Performance Computing. Overall SCARF now has over 10000 CPU cores, 58TB memory and 300TB of disk space (Details in Appendix 1).

This report covers the year 2016-17 and outlines the research that SCARF has enabled.

1.1   SCARF Usage by Department

Each time a researcher uses the SCARF service the CPU time used is recorded. Jobs submitted to SCARF used 36.1 million CPU Hours during 2016-17.

SCARF USAGE 2016-2017

RAL Space, 1.23%
Diamond, 4.87%
PPD, 0.04%
ISIS, 36.84%
CLF, 22.37%
SCD/Hartree, 34.66%
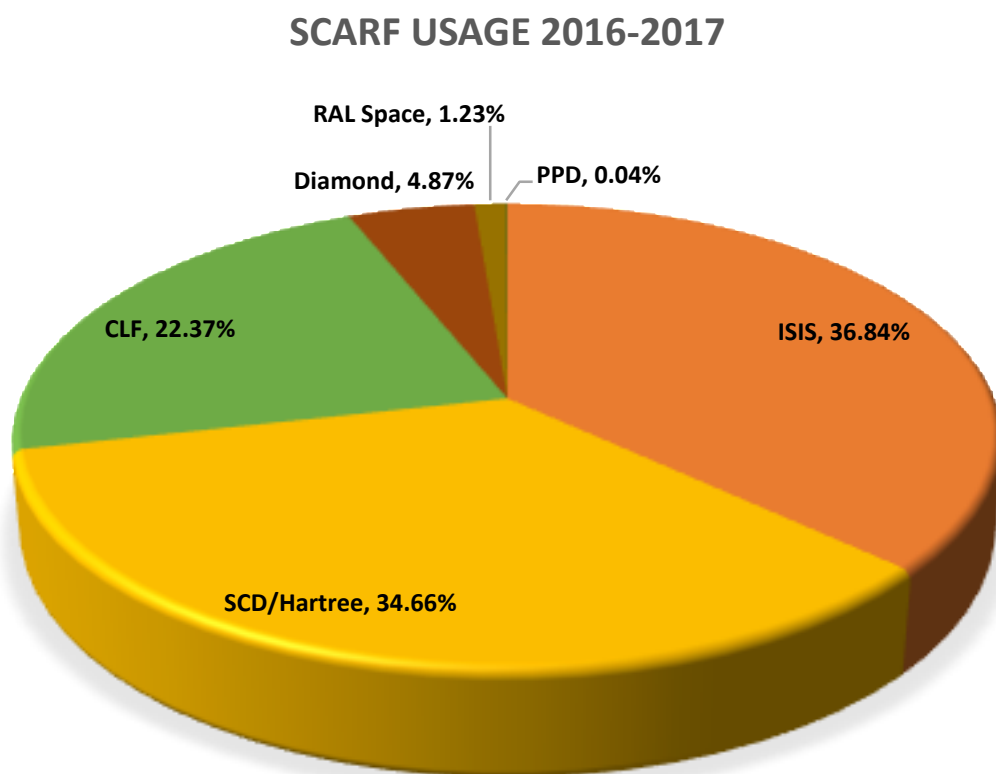
Figure 1.1.1: Pie chart showing percentage usage of the SCARF service by department

It is clear from the usage chart that ISIS, CLF and Scientific Computing are the heaviest users of SCARF. The table below shows the number of active users affiliated with e.g. Staff, collaborating with or using the facilities of various STFC departments and significant external facilities such as Diamond or CCFE. We have stopped counting External access users separately; instead they are now counted under the STFC Department they are collaborating with. The Hartree Centre has been moved from the Scientific Computing Department to its own department, but this is not yet reflected in the SCARF accounting configuration.

	2016-17			2015-16			2014-15		
Dept	Active Users	CPU hrs	%	Active Users	CPU hrs	%	Active Users	CPU hrs	%
SCD/Hartree	71	12229692.6	34.7	52	11394064.3	36.2	49	8210127.49	31.4
ISIS	61	12998061.7	36.8	54	10413282.5	33.1	31	4987828.88	19.1
External	n/a	n/a	n/a	n/a	n/a	n/a	37	6716465.17	25.7
CLF	56	7893198.1	22.4	43	6829135.47	21.7	19	5298080.49	20.3
DIAMOND	11	1717467.6	4.9	3	1653629.8	5.2	6	141874.42	0.54
ASTEC	0	0	0	2	58299.64	0.19	3	45641.77	0.17
RAL Space	4	432680.9	1.2	5	989267.1	3.1	4	718069.17	2.8
CCFE	0	0	0	1	81.59	0	0	0	0
PPD	3	15108.7	0.04	0	0	0	0	0	0
Totals	206	35286209	100	165	31451022	100	149	26118087	100

Figure 1.1.2: Table displaying detailed usage from 2016-17 comparing with 2015-16 and 2014-15

A significant amount of computational resource has been used on SCARF; section 3 highlights some of the scientific achievements that have been enabled.

1.1 SCARF Availability

The aim is to keep SCARF available to users as much as possible. SCARF was taken offline for 1 day due to a site-wide power outage at Rutherford Appleton Laboratory in November. A patch to fix an issue with nodes being unreachable was applied to the batch system requiring jobs to be suspended. Security patching occurred several times over the period, requiring downtimes on each frontend to reboot them.

1.2 SCARF Developments 2016-17

Major SCARF Developments are listed below. A more detailed list can be found in Appendix 5

- New capacity added in July 2017
    - 1608 Intel E5-2650v4 CPU cores for use by CLF Plasma Physics collaborators
    - 3216 Intel E5-2650v3 CPU cores for general use

1.3 Future Developments

The hardware procurement of SCARF18 is currently in progress, it is expected to be delivered by the end of March and to enter service in mid-2018. The existing 7 Panasas ActiveStor shelves have reached end of life, the procurement of the replacement is also in progress.

SCARF17 has been deployed as RHEL7, the program to migrate the remainder of SCARF to RHEL7 will continue in the coming year. Investigation will continue in to how to incorporate GPU resource into SCARF.

SCARF's application server will be replaced with a new service due to the existing hardware reaching end of life.

The network underlying SCARF will be replaced with a faster more resilient infrastructure, increasing the bandwidth between SCARF and STFC's core network

1.4   Help and Support

For any queries concerning the SCARF service, please email the SCARF Helpdesk

scarf@hpc-support.rl.ac.uk

1.4   Help and Support

2. PUBLICATIONS AND PRESENTATIONS

2.1 Publications

A list of publications is given in Section 6. A way of estimating the impact that SCARF has had is to analyse the Journal Impact Factor using the Journal Citation Reports published by Thomson Reuters (2016). The average Impact Factor for Journals published as a result of using SCARF is 7.2.

2.2 Presentations

Scientists have presented their work at 12 international conferences (See Section 6). This helps to demonstrate that the science enabled by SCARF is world class.

3.   SCIENCE HIGHLIGHTS

3.1   Using molecular dynamics simulation in the analysis of neutron and X-ray reflectivity

Andrew R. McCluskey[1,2], James Grant[3], Robert D. Barker[4], Andrew J. Smith[2], Jonathan L. Rawle[2], Stephen C. Parker[1], & Karen J. Edler[1]

[1] *Department of Chemistry, University of Bath, Bath.*

[2] *Diamond Light Source, Rutherford Appleton Laboratory, Harwell-Oxford.*

[3] *Computing Services, University of Bath, Bath.*

[4] *School of Physical Sciences, University of Kent, Canterbury.*

As the flux of neutron and X-ray sources increases, so does the complexity of science to which neutron and X-ray techniques can be applied – the more complex science will require more intelligent analysis procedures in order to make the most of the information available. This has led to the popularization of 'multi-modal analysis' methods, where other experimental and computational techniques are used to augment the neutron and X-ray experiments. This work is focused on the use of molecular dynamics simulations to complement neutron and X-ray scattering of soft matter systems. We have developed software to allow for the easy comparison between reflectivity experiments and simulation, and have applied this to the study of a biologically-relevant lipid monolayer, identifying the benefits of the molecular dynamics based approach to data analysis.
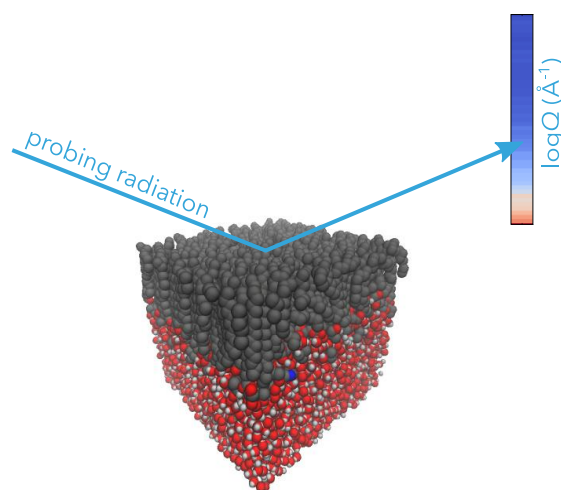
Figure 3.1.1: A schematic of a reflectivity experiment

Neutron (seven contrasts) and X-ray reflectivity profiles of the DSPC monolayer at the air-water interface were collected at four different surface pressures on SURF (ISIS) and I07 (Diamond Light Source). The monolayer system was simulated by placing the 100 lipid molecules at the interface between a vacuum and 10000 water molecules. The simulation was then subjected to an anisotropic barostat, such that simulation cell shrunk in the *x*- and *y*-dimensions but grew in the *z*-dimension – emulating the action of a Langmuir trough. Using the knowledge of the experimental area-per-molecule, starting structures for the production molecular dynamics simulations were then found where the simulation cell had an area per molecule that best matched the experiment. The production simulations were run for 50 ns on the SCARF computing cluster; to preserve the monolayer, a wall of dummy atoms was placed at the top and bottom of the simulation cell, with a

pressure of 1 atmosphere in the z-dimension and the x- and y-dimensions held constant. A 2-dimensional periodic boundary condition was also used to stop interactions across the dummy atom wall taking place.

The open-source C++ software falass [1,2] was developed to determine the neutron or X-ray reflectivity of a given simulation trajectory. This involves dividing the simulation cell into a series of layers of a user-defined width, going down the z-axis. The scattering length density of each layer is then found, by summing the scattering lengths of the individual atoms in the layer. The Abelès matrix formalism [3] is used to calculate the scattering from such a system, using the time-averaged scattering length densities. The calculated reflectivity is then matched to the experimental data by scaling the intensity and introducing a uniform background. Figure 3.1.2 shows a comparison between the experimental reflectivity and that determined from the molecular dynamics simulation. The good agreement between the experimental and the calculated reflectivity profile indicate the utility that this method has to offer in the analysis of reflectivity data from both neutron and X-ray experiments. The molecular dynamics simulation can be used to better understand details of the system understudy, such as headgroup hydration or chain tilt direction. This work is currently being written up into a publication that will discuss these benefits at length and draw comparison with other commonly used analysis methods [4].
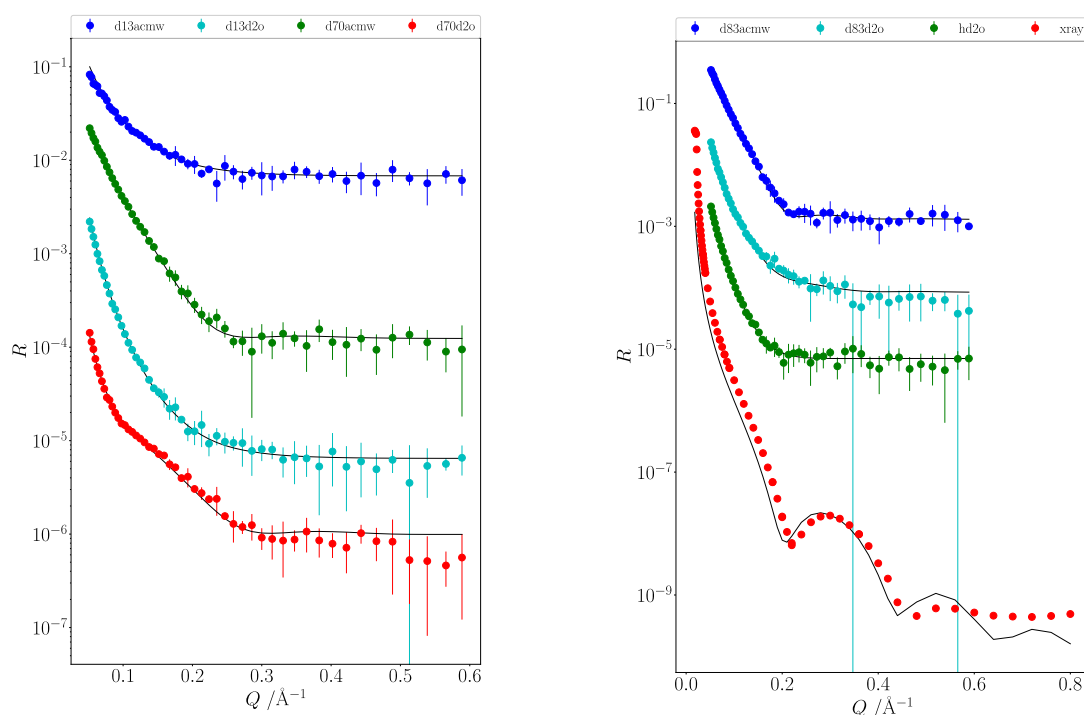
Figure 3.1.2: A comparison between the experimental reflectivity profiles and the reflectivity data calculated from molecular dynamics simulation, for each of the seven neutron contrasts and the X-ray data.

References

[1] McCluskey, A.R., *et al. J. Appl. Crystallogr.* (Submitted).

[2] McCluskey, A. R., (2017). falass. doi:10.5281/zenodo.832784. 0.1-beta.

[3] Abelès, F. (1950). Le Journal de Physique et la Radium, 11, 307–310.

[4] McCluskey, A.R., *et al.* (In Preparation).

3.2 Structure and Vibrational Spectra of 2,5-Diiodothiophene: a Model for Polythiophene.

Stewart F. Parker, Jack L. Parker and Marek Jura

ISIS Facility, STFC Rutherford Appleton Laboratory, Chilton, Didcot, Oxon OX11 0QX, UK,

Polymeric solar cells are a promising alternative for producing clean and renewable energy due to the possibility of fabricating them onto large areas of lightweight, flexible substrates by solution processing at low cost [1]. In this context, oligothiophenes and polythiophenes are attracting increasing interest because they offer a range of promising properties. In part, this arises because thiophene chemistry is well-developed [2] and functionalisation and derivatisation of the C_4H_4S core is possible in many different ways.

Alkyl-substituted polythiophenes are soluble and their use as a starting material allows thin film fabrication using conventional spin-coating methods. An alternative approach is to polymerise a monomer on a patterned surface. 2,5-Diiodothiophene (see inset to Figure 3.2.1) is a promising material for this method because the C–I bonds can be selectively dissociated by ultraviolet irradiation, generating thienyl radicals that polymerise [3].

Vibrational spectroscopy provides a valuable method to characterise the materials and, to this end, the spectra of polythiophene, oligothiophenes and thiophene have been assigned. However, the spectra of 2,5-diiodothiophene have been little investigated. The standard method for assigning the spectra, comparison with *ab initio* calculations, was hampered by the absence of structural information about the molecule. In the course of this work [4], we have carried out a structural characterisation of 2,5-diiodothiophene by single crystal X-ray diffraction and a complete assignment of the vibrational (infrared, Raman and inelastic neutron scattering (INS)) spectra of the molecule, with the assignments supported by periodic density functional theory (DFT) calculations.
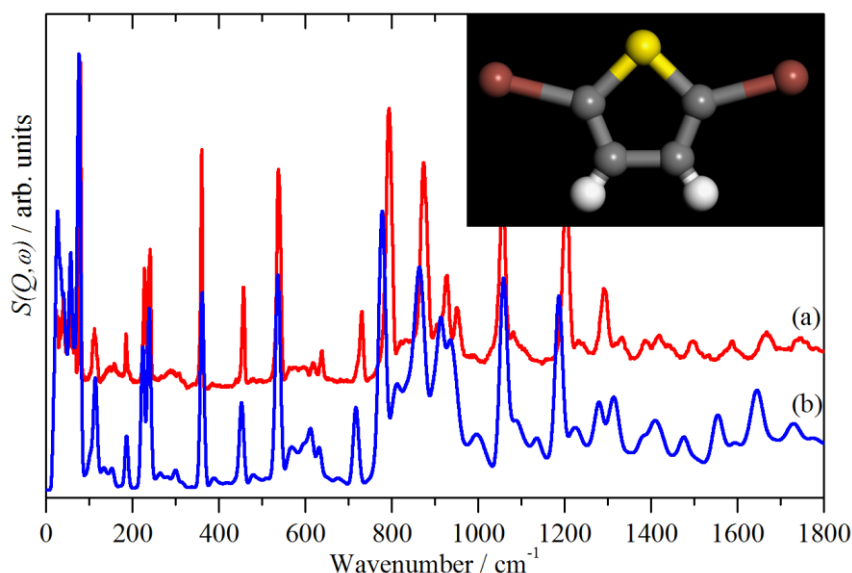
Figure 3.2.1: Observed (a) and CASTEP calculated (b) INS spectra of 2,5-diiodothiophene at 20 K. The inset shows the molecular structure (grey = carbon, yellow = sulfur, white = hydrogen, brown = iodine).

Figure 3.2.1 compares the observed and CASTEP calculated INS spectra of 2,5-diiodothiophene at 20 K. It can be seen that the agreement is essentially quantitative for both the transition energies and relative intensities. The experimental spectrum is noteworthy for the sharpness of the lines and the very weak phonon wings. Infrared and Raman spectra are measured at the Γ-point in the Brillouin zone *i.e.* (almost) zero wavevector. In contrast, INS spectra are measured at all wavevectors and the calculated INS spectrum in Figure 3.2.1 is generated from a calculation of the transition energies as a function of wavevector (dispersion) across the entire Brillouin zone. Figure 3.2.2 shows the dispersion plot for 2,5-diiodothiophene. The modes are noticeable for being almost dispersionless: even the optic whole-body (external) modes are almost flat, Figure 3.2.2a. This is particularly apparent for the C–H stretch modes, Figure 3.2.2b, and the in-plane ring deformation modes, Figure 3.2.2c, where the dispersion is less than the factor group splitting. This is the spectral consequence of the absence of any significant intermolecular interaction that is apparent from the structural determination. The result is that the INS modes are very sharp and on many instruments are resolution limited, (although not on TOSCA). This has led to 2,5-diiodothiophene becoming the compound of choice for both resolution and wavenumber calibration of INS spectrometers.
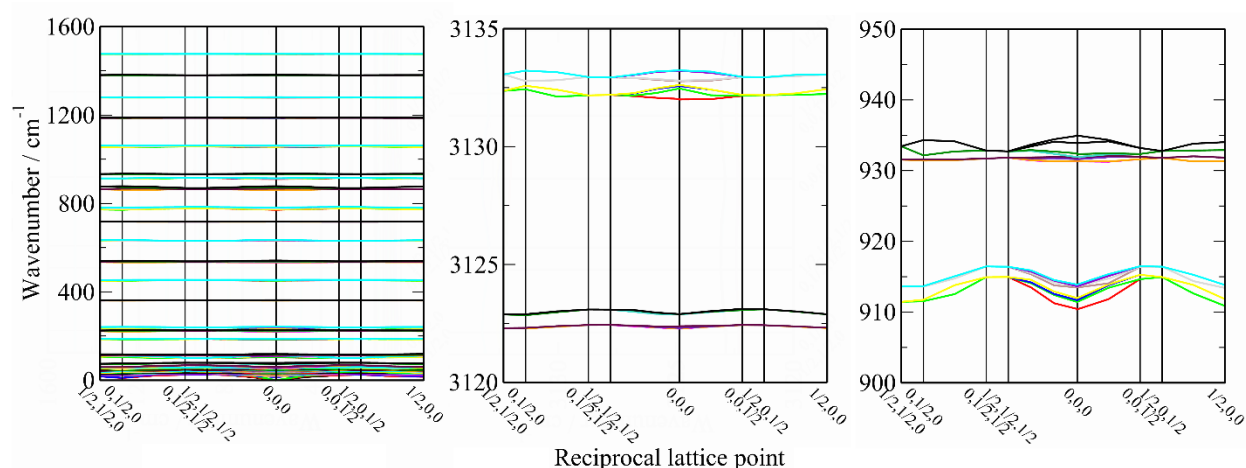
Figure 3.2.2: CASTEP calculated dispersion curves of 2,5-diiodothiophene: (a) the fingerprint region, (b) C–H stretch region and (c) expanded view of the in-plane ring deformation modes.

Comparison to the INS and Raman spectra of polythiophene (for which 2,5-diiodothiophene may be used as a monomer [3]), shows that the INS spectrum of polythiophene is dominated by the C–H bending modes, which are unchanged on polymerisation. In contrast, the Raman spectrum of polythiophene is dominated by the changed electronic environment which results in strong electron-phonon coupling and a significant upshift of the C=C stretch modes.

References

[1] Mazzio, K. A.; Luscombe, C. K. The future of organic photovoltaics. *Chem. Soc. Rev.* 2015, *44*, 78-90.

[2] Gronowitz, S.; Hörnfeldt, A.-B. *Thiophenes*; Elsevier Academic Press: San Diego, CA, 2004.

[3] Natarajan, S.; Kim, S. H. Maskless fabrication of polythiophene patterns by photochemical conversion of regioselectively condensed 2,5-diiodothiophene. *Langmuir* 2005, *21*, 7052-7056.

[4] Parker, S.F.; Parker, J.L.; Jura, M. *Journal of Physical Chemistry C* 2017, *121*, 12636-12642.

3.3   Peptide-membrane interaction characterized with atomistic MD simulation

Ya-Wen Hsiao

Scientific Computing Department, STFC Daresbury Laboratory, Keckwick Lane, Daresbury, Warrington, U.K.

Antimicrobial peptides (AMPs) are part of the innate defense system. They demonstrate antimicrobial, anticancer, anti-HIV, etc. activities, and thus pose as prominent future drug candidates.

Understanding the mechanism behind the activity is certainly vital for designing AMPs into drugs of the right efficacy. There are many proposed modes of action that are mostly addressing the pathogen membrane disruption by AMPs. However, the understanding of underlying mechanisms at atomistic level is still incomplete to support hypotheses and clarify experimental observations, and experiments cannot, e.g. capture the onset of the pore formation, MD simulations may be instrumental in filling up the knowledge gap.

We performed all-atom MD study as well as free energy explorations starting with cecropin B. Cecropins from the Cecropia moth (Hyalophoru cecropia) form a family of AMPs and demonstrate a broad spectrum antibacterial activity on both Gram-negative and Gram-positive bacteria. By gaining understanding on mechanism of cecropin B (and maybe more AMPs) interacting with membrane, we aim to put forward designing ideas for AMPs.
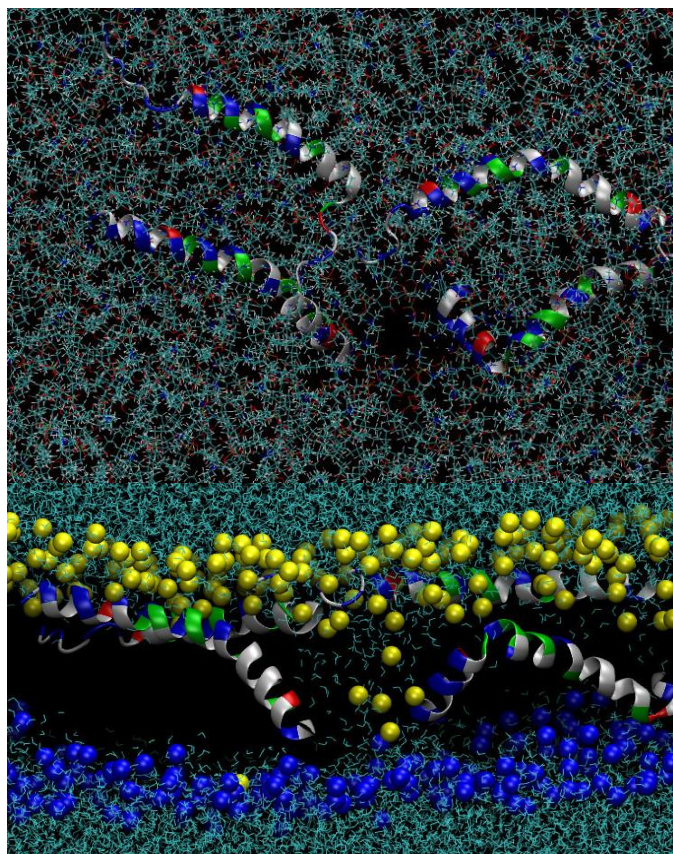
Figure 3.3.1: Antimicrobial peptide cecropin B forming a pore on membrane: top and side views. Yellow and blue spheres are phospholipid headgroups from upper and lower membrane leaflet, respectively. Water molecules are shown in cyan (lower panel).

3.4 Inelastic neutron scattering spectra of cellulose forms

C. Araujo,[1] M. Nolasco,[1] P. Ribeiro-Claro, [1] P. D. Vaz, [2,3] S. Rudić, [2] A. Silvestre, [1] C. Freire[1]

[1] CICECO – Aveiro Institute of Materials, Departamento de Química, Universidade de Aveiro, 3810-193 Aveiro, Portugal
[2] ISIS Neutron & Muon Source, STFC Rutherford Appleton Laboratory, Chilton, Didcot, Oxfordshire, UK
[3] CQB, Departamento de Química e Bioquímica, Faculdade de Ciências da Universidade de Lisboa, 1749-016 Lisboa, Portugal

Inelastic Neutron Scattering (INS) spectroscopy provides a new tool for the study of structure and properties of cellulose and cellulose-based materials.

Cellulose (Figure 3.4.1), described as a "fascinating biopolymer and sustainable raw material" [1] is attracting increasing attention due to its structural properties, its broad chemical modifying capacity, and its formation of versatile semicrystalline fiber morphologies, with high potential in the development of innovative materials.
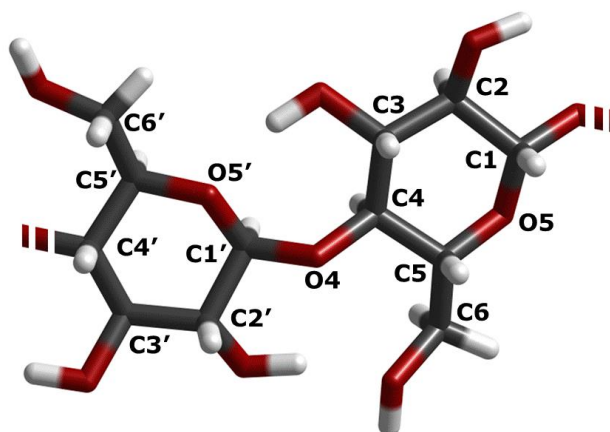
Figure 3.4.1: Atom labelling for cellulose unit according to the IUPAC recommendation for cellobiose.

Both the efficiency of chemical transformations and the properties of cellulose-derived materials depend on the nanometer scale morphology of cellulose microfibrils Therefore, methods to characterize the structure and packing of cellulose microfibrils and their bundles are highly desirable.

Both the efficiency of chemical transformations and the properties of cellulose-derived materials depend on the nanometer scale morphology of cellulose microfibrils Therefore, methods to characterize the structure and packing of cellulose microfibrils and their bundles are highly desirable.

Among the techniques used to study and characterize cellulose structure, vibrational spectroscopy plays a relevant role. Reports on the vibrational spectra of cellulose samples can be traced back to 1940, and both infrared and Raman spectroscopies are currently used has major tools to assess the composition of cellulose samples, the nanometer scale morphology of cellulose fibers and the mechanical properties of cellulose-based materials.

Inelastic Neutron Scattering (INS) spectroscopy is a vibrational spectroscopic technique which provides information not amenable from its optical counterparts (IR and Raman). In short, in INS there are no selection rules for the activity of vibrational modes, and the signal intensity is proportional to nuclei displacement and nuclei cross-section, both of which are particularly high for hydrogen atoms. This turns the technique particularly suitable to study the dynamics of hydrogen atoms and hydrogen-bond networks. In addition, INS can probe the structural changes induced by functionalization of cellulose chains and formulation of composite materials with cellulose fibers

SCARF is making possible the use of periodic density functional theory (periodic-DFT) calculations were carried out using the plane wave pseudopotential method as implemented in the CASTEP code. Exchange and correlation were approximated using the PBE functional. The plane-wave cut-off energy was 830 eV. Brillouin zone sampling of electronic states was performed on 8 × 4 × 4 Monkhorst-Pack grid. The equilibrium structure, an essential prerequisite for lattice dynamics calculations was obtained by BFGS geometry optimization after which the residual forces were converged to zero within 0.005 eV·A^{-1}. Phonon frequencies were obtained by diagonalization of dynamical matrices computed using density-functional perturbation theory. The atomic displacements in each mode that are part of the CASTEP output, enable visualization of the modes to aid assignments and are also all that is required to generate the INS spectrum using the program aCLIMAX. It is emphasised that for all the calculated spectra shown the transition energies have not been scaled (Figure 3.4.2).
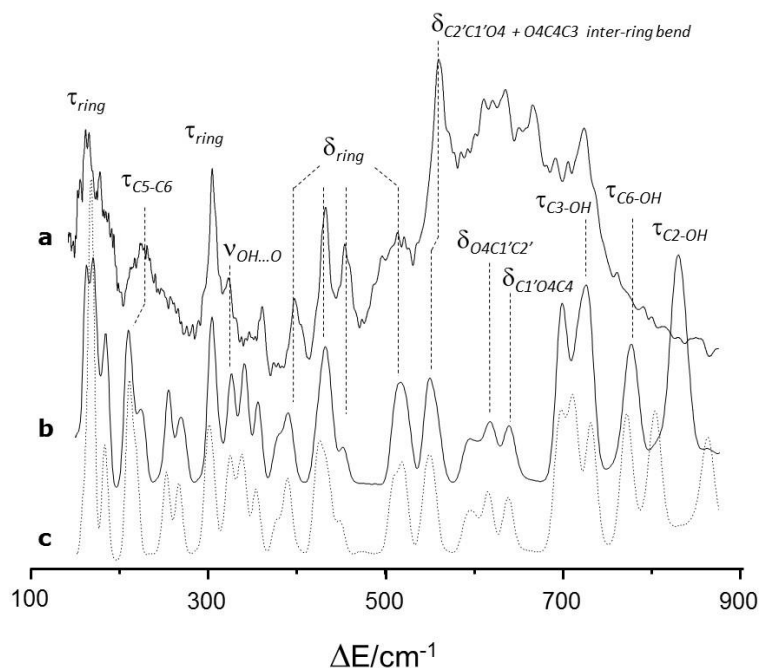
Figure 3.4.2: Comparison of the experimental INS spectrum of cotton (a) with CASTEP calculated spectra of cellulose I$_\beta$ (b) and I$_\alpha$ (c), in the 150-900 cm^{-1} region. The assignments are shown for the most relevant bands (ν = stretching; δ = angle deformation; τ = torsion)

References

[1] Klemm, D., Heublein, B., Fink, H.-P. and Bohn, A., Cellulose: Fascinating Biopolymer and Sustainable Raw Material, *Angewandte Chemie International Edition*, 44 (2005): 3358–3393.DOI:10.1002/anie.200460587

### 3.5   Vibrational profile of next generation biodegradable polymers: polyethylene furanoate

C. Araujo,[1] M. Nolasco,[1] P. Ribeiro-Claro, [1] P. D. Vaz, [2,3] S. Rudić, [2] A. Silvestre, [1] A. F. Sousa [1]

[1] *CICECO – Aveiro Institute of Materials, Departamento de Química, Universidade de Aveiro, 3810-193 Aveiro, Portugal*

[2] *ISIS Neutron & Muon Source, STFC Rutherford Appleton Laboratory, Chilton, Didcot, Oxfordshire, UK*

[3] *CQB, Departamento de Química e Bioquímica, Faculdade de Ciências da Universidade de Lisboa, 1749-016 Lisboa, Portugal*

The second half of the 20th century witnessed the rise of oil-based synthetic polymers, whose outstanding properties led to a veritable increase in the standards of living and technological advancement. Their monopoly grew unabated until the dawn of the 21st century when depletion of fossil resources, along with the environmental impact of plastic waste, called for a paradigm shift in polymer production, bringing forth a new class of sustainable materials derived from renewable resources which will gradually phase out their petrochemical counterparts. An example of this new paradigm is the replacement of poly(ethylene terephthalate) (PET), an ubiquitous packaging material produced from olefins, with poly(ethylene 2,5-furandicarboxylate) (PEF). This is an analogue polyester based of 2,5-furandicarboxylic acid (FDCA) and ethylene glycol (EG), Figure 3.5.1, which can be obtained from sugars. PEF has drawn a great deal of interest from food and beverage industries as PET replacement, not only due to PEF's lower carbon footprint but also due to its improved properties.
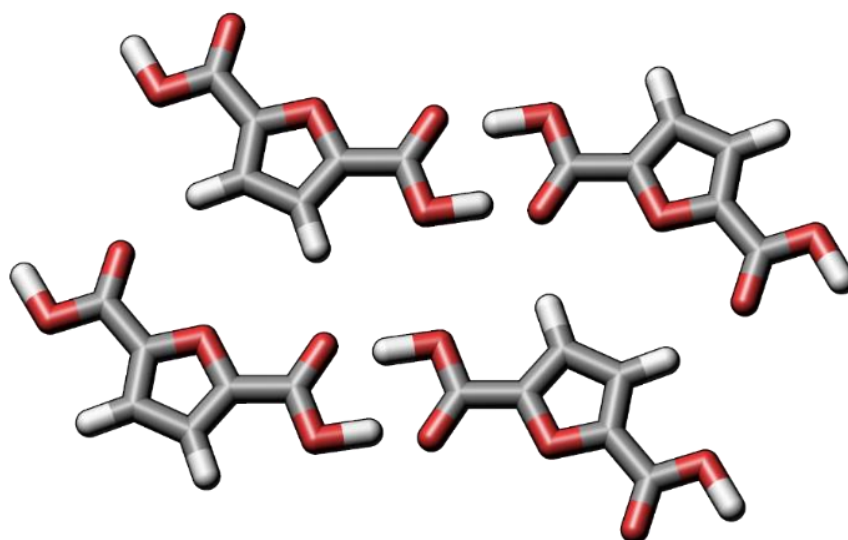
Figure 3.5.1: PEF structural unit, where an intricate H-bond network can be identified.

Compared to PET, PEF offers improved thermal stability, good mechanical performance and increased barrier properties – it is 10 times less permeable to oxygen and 20 times less permeable to carbon dioxide, despite its higher free volume. It is then prime time to better understand PEF's properties. A series of studies have dealt with its thermal, mechanical and barrier properties, kinetics and dynamics of crystallization and crystal structure.

The inelastic neutron scattering (INS) profile of PEF has been measured (Figure 3.5.2) at ISIS and is under analysis using the INS profile of PET as benchmark in view of drawing spectrum-structure-property correlations. INS is a powerful technique for studying polymers, as it allows probing the low frequency region of vibrational spectra – informing on their 3D spatial arrangement -, is especially sensitive to the motions of hydrogen atoms and has no selection rules – all vibrational modes are permitted. The assignment of PEF's INS spectrum herein presented may serve as a guide for future INS studies on PEF's composites or analogue polymers.
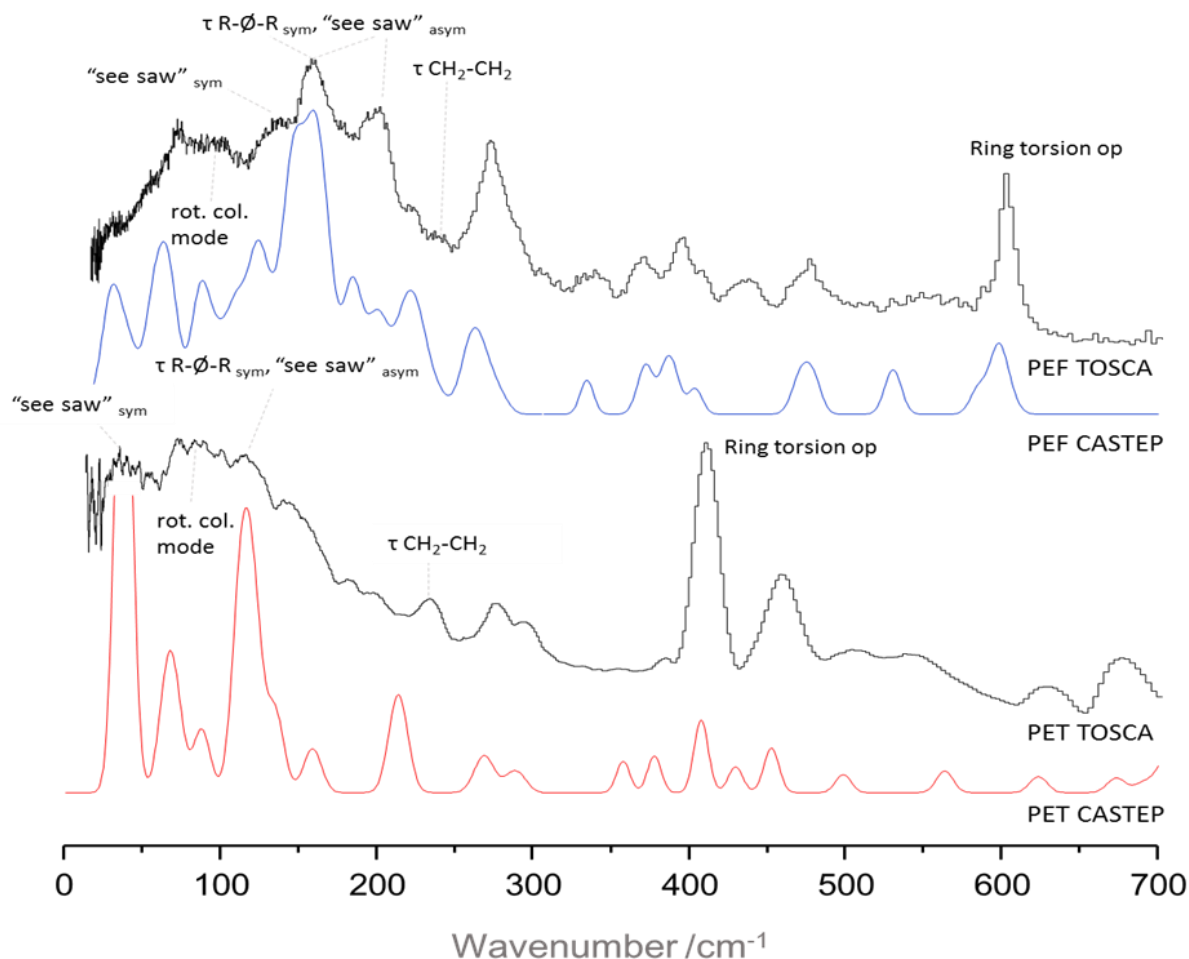
Figure 3.5.2: Comparison of the experimental INS spectrum (TOSCA) of PET and PEF with CASTEP calculated spectra in the 20-700 cm^{-1} region. The assignments are shown for the most relevant bands (τ = torsion)

3.6   Solventless oxidation of olefins by Mo@surface of carbon waste material

Cécile Petit,[1] Miguel V. Silva[1], Ana S. Mestre[1], Ana P. Carvalho, [1] Pedro D. Vaz, [1,2] Carla D. Nunes[1]

[1] CQB, Departamento de Química e Bioquímica, Faculdade de Ciências da Universidade de Lisboa, 1749-016 Lisboa, Portugal
[2] ISIS Neutron & Muon Source, STFC Rutherford Appleton Laboratory, Chilton,Didcot, Oxfordshire, UK

Reusable heterogeneous catalysts have attracted a great deal of interest from laboratory and industrial points of view [1]. Since most of the catalysts are expensive and contaminate the environment, the development of efficient methods for recovery and reuse of the catalysts is a very important aspect from an economical point of view. In recent years, to overcome these problems, heterogenization of homogeneous catalysts has attracted much attention because it combines the best properties of both homogeneous and heterogeneous counterparts [2]. Among the various approaches for immobilizing soluble catalysts, covalent attachment has been the most frequently used strategy, as the resulting heterogeneous catalysts have good stability during the catalytic reactions. In this approach, catalyst leaching from the support is minimized and thus, provides a way to prepare site isolated catalysts. In this manner, different soluble complexes have been immobilized on various supports such as silica, organic polymers, carbon nanotubes, metal–organic frameworks, etc.

Carbons are the most versatile materials used in the modern fields of renewable energy, environmental science and catalysis. However, there is a need and indeed a desire to develop increasingly more sustainable variants of classical carbon materials particularly when the whole life cycle is considered. Therefore, the synthesis and application of sustainable carbon materials are receiving increasing levels of interest, particularly as supports of catalysts. Selective olefin epoxidation is a very important process since epoxides are relevant building blocks across many areas. In this context, Mo-catalyzed olefin epoxidation has received interest from both academic and industrial research laboratories. Continuing research on the development of stable, active and selective catalysts for olefin epoxidation, in this work we describe the preparation of a sisal derived carbon material inspired in literature that was further derivatized with a Mo complex – $[MoI_2(CO)_3(MeCN)_2]$. The resulting material was subsequently evaluated for its catalytic potential in olefin epoxidation reactions of cis-cyclooctene (cy8), styrene (sty) and R(+)-limonene (R-lim). The reaction scope has been assessed by varying relevant parameters such as temperature, solvent and oxidant ratio. As will be discussed the methodology followed proved to be a good strategy since the use of the carbon material as support leads to enhanced conversion and selectivity of products.

However, given its disordered nature, a proper structural characterization of these materials is always hard and defying. In this way, using literature data that established some structural models [3] we are performing DFT calculations to assess the structure of the carbon materials used in this work. The selection of the initial structure was based on the experimental C, H, N elemental analysis data. The optimized structure using Gaussian 09 code is displayed in Figure 3.6.1.
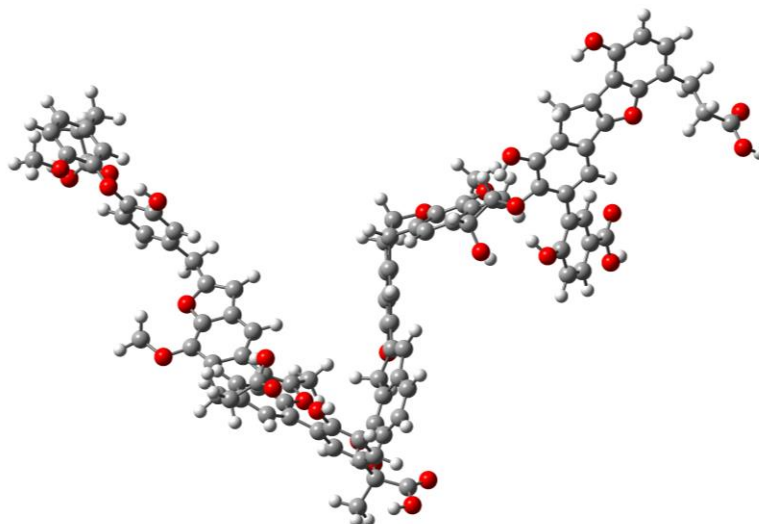
Figure 3.6.1: Structural unit of the carbon material used as catalyst support

We have then carried out simulation of both the vibrational (FTIR) and of the NMR spectra, and compared with the experimental data. According to Figure 3.6.2,
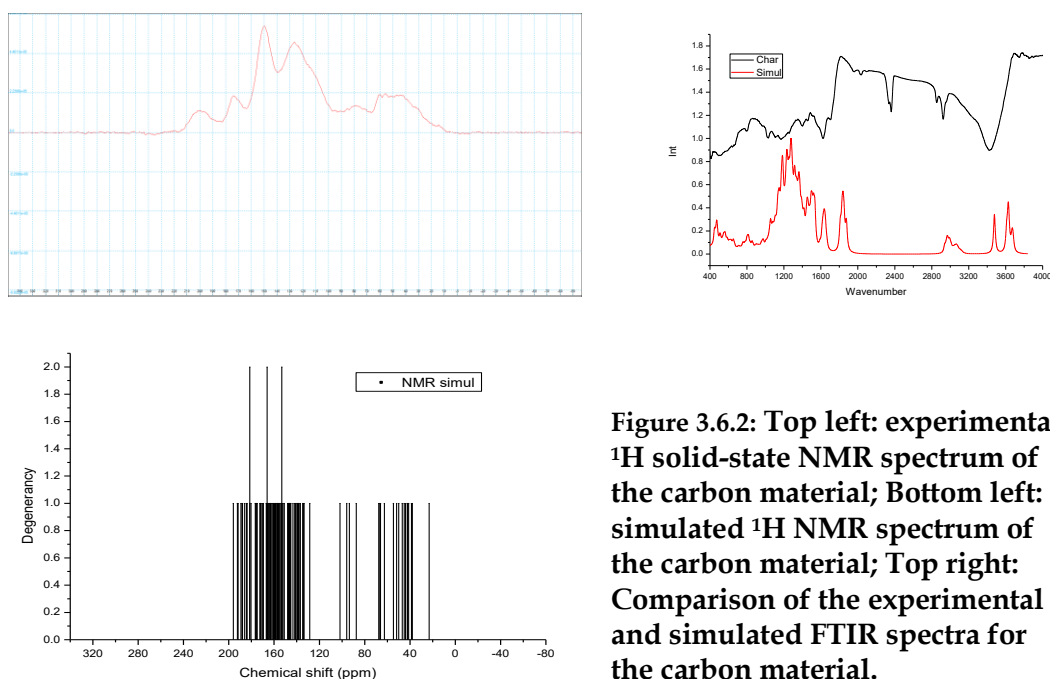
Figure 3.6.2: Top left: experimental ^{1}H solid-state NMR spectrum of the carbon material; Bottom left: simulated ^{1}H NMR spectrum of the carbon material; Top right: Comparison of the experimental and simulated FTIR spectra for the carbon material.

As can be seen, for this material, both the ^{1}H NMR and the FTIR spectra agree to a good level validating the choice of this structure as a model for the carbon material described in this work.

References

[1] A. Corma, M. Domine, J.L. Jorda, M.T. Navarro, F. Rey, J. Perez-Pariente, J. Tsuji, B. Mc Culloch, L.T. Nemeth, *Chem. Commun.*, (1998), 2211

[2] G. A. Barf, R. A. Sheldon, *J. Mol. Catal. A: Chem.*, 102 (1995), 23

[3] J.P. Mathews, A.L. Chaffee, *Fuel*, 96 (2012), 1

3.7 Solvent Accessibility and Water Binding in Native Copper Nitrite Reductases

Kakali Sen[1,2], Michael A. Hough[1], Richard W. Strange[1], Chin W. Yong[2], Thomas W. Keal[2]

[1] *School of Biological Sciences, University of Essex, Wivenhoe Park, Colchester, Essex, UK*
[2] *Scientific Computing Department, STFC Daresbury Laboratory, Warrington, Cheshire, UK*

Microbial copper-containing nitrite reductases (CuNiRs) are enzymes that catalyze the reduction of NO_2^- to NO, a key denitrification step in the global nitrogen cycle. This process involves a proton-coupled electron transfer reaction involving the two copper sites, the electron donating T1Cu site and the catalytic T2Cu site. The T1Cu site in turn receives electron from a redox partner in two-domain (2D) CuNiR and from an integrated redox unit in three-domain (3D) CuNiR. Figure 3.7.1 shows a typical 2D CuNiR; *Ac*NiR and 3D CuNiR; *Rp*NiR with its electron transfer cytochrome domain. In this project, we used the SCARF computing facilities to carry out multiscale computer modelling on the above two mentioned CuNiRs, the *Ac*NiR and *Rp*NiR. Our aim is to investigate the pathways of proton and electron transfer and the reductive mechanisms at the T2Cu site.
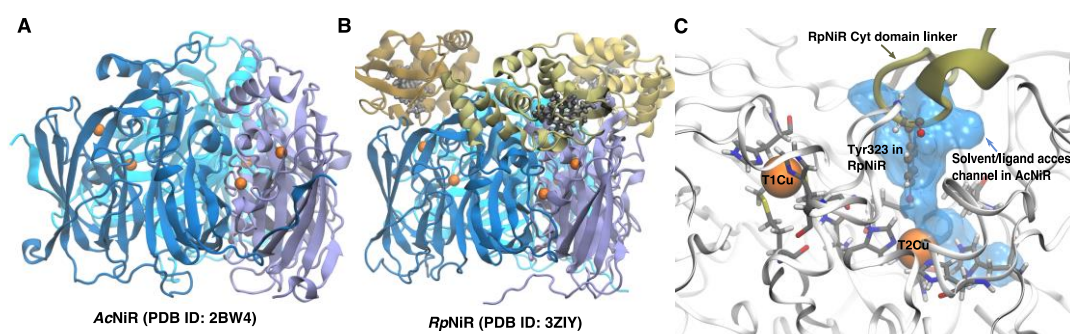

Figure 3.7.1: A) AcNiR, a 2D CuNiR from Achromobacter cycloclastes and B) RpNiR, a 3D CuNiR from Ralstonia picketti. The Cu atoms are shown in orange and the heme units of the cytochrome domain of RpNiR are in black. C) Structural overlap of AcNiR and RpNiR. The backbone and active site residues from AcNiR are shown for clarity. Only the key T232 from the cytochrome domain of RpNiR that blocks the otherwise solvent/ligand access channel is shown.

The T2Cu active site residues Asp_CAT and His_CAT are known to facilitate water and proton accessibility to the active site of NO_2^- reduction (T2Cu). Classical all-atom MD simulations starting from crystal structures of two-and three-domain CuNiRs in their native state were carried out with the massively parallel NAMD software installed in SCARF. All possible protonation states of Asp_CAT and His_CAT were taken into consideration for *Ac*NiR. Two experimentally observed orientations of Asp_CAT, proximal and gatekeeper, were reproduced in the long MD runs only on protonation of the Asp_CAT and were independent of the protonation state of His_CAT. (Figure 3.6.2) This flexibility of Asp_CAT further facilitates water and proton accessibility to the active site of NO_2^- reduction (T2Cu) in AcNiR. [Sen, et. al. 2017]
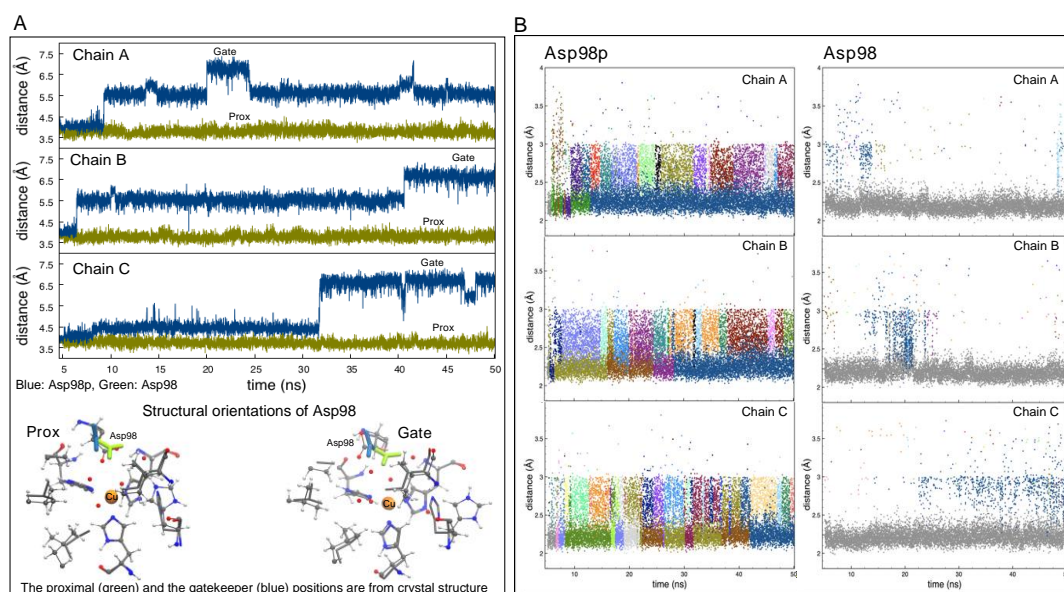
Figure 3.7.2: A) Time evolution of distance between T2Cu and center of mass of Asp98 carboxyl group in protonated Asp98 protein (Asp98p, blue) and deprotonated Asp98 protein (Asp98, green) in AcNiR. The two Asp98 orientations observed in crystal structures as well as in MD simulations are shown below. B) Solvent accessibility at the active-site pocket during MD simulations for both Asp98p and Asp98 systems. Water molecules within 3.0 A of the T2Cu in each monomer of the AcNiR trimer are shown in different colors, with the bound water in the original crystal structure shown in grey.

The picture is however, slightly different in case of 3D *Rp*NiR. The Tyr323 residue from the ET domain occupies the otherwise solvent/ligand accessible channel in 2D CuNiR thereby blocking the solvent/ligand accessibility as well as locking Asp_CAT in proximal orientation via hydrogen bonding. (Figure 3.7.1) This H-bond is maintained along the 80 ns MD simulations and is transiently broken when Asp_CAT is protonated. (Figure 3.7.3) Unlike *Ac*NiR, no further enhancement of solvent accessibility with protonation of Asp_CAT was observed in case of *Rp*NiR.
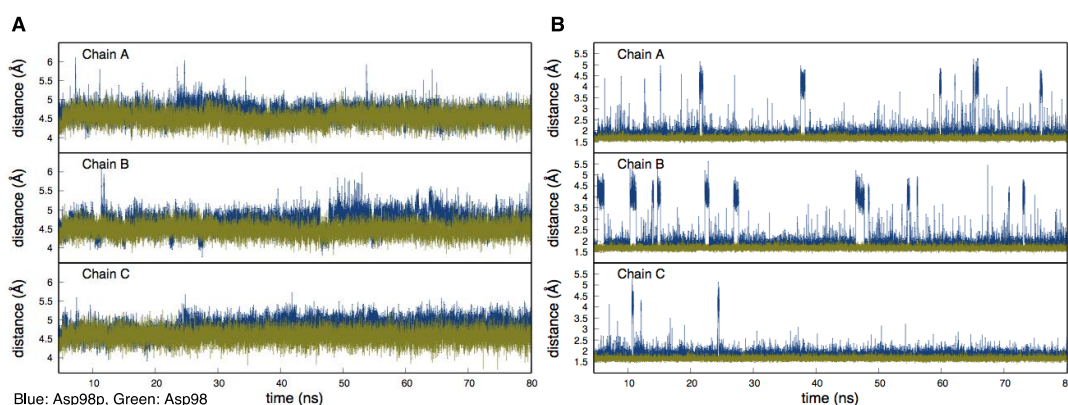
Figure 3.7.3: A) Time evolution of distance between T2Cu and center of mass of Asp98 carboxyl group for protonated Asp98 protein (Asp98p, blue) and deprotonated Asp98 protein (Asp98, green) in RpNiR. B) Time evolution of the H-bond distance between Asp98 carboxylic group and Tyr323 hydroxyl group.

A correlation between the copper oxidation state and the conformational orientation of water molecules bound at the T2Cu site was determined using standalone QM and hybrid QM/MM

studies. Hybrid QM/MM studies were carried out with the modular code Chemshell installed in SCARF using Orca and DL_POLY as the QM and MM drivers, respectively. Both QM/MM (Figure 3.7.4) and QM results corroborate closely to our serial crystallography observations of loss of one water in native state on reduction of Cu at T2Cu site. [Sen, et. al. 2017] This correlation between oxidation state and waters at T2Cu site is valid for both *Ac*NiR and *Rp*NiR.

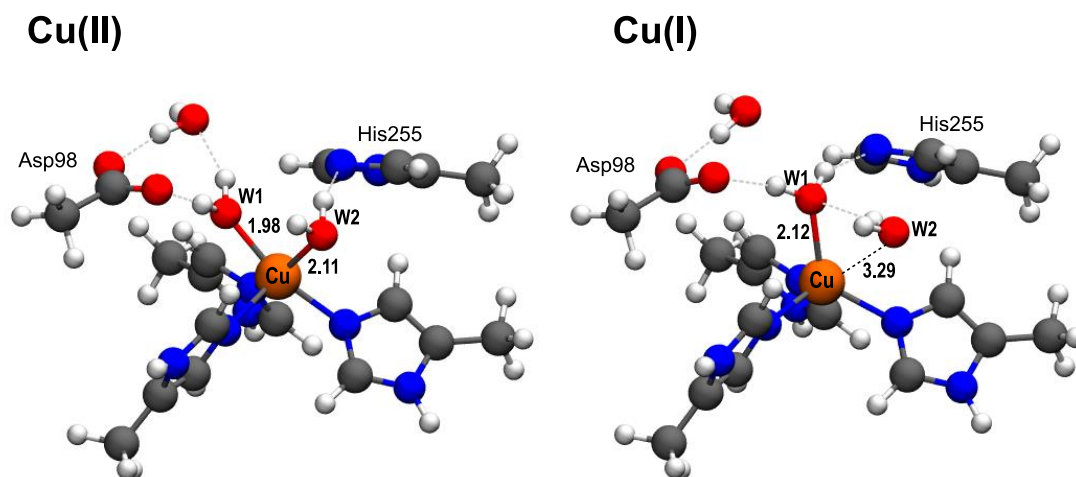**Figure 3.7.4: QM/MM optimized structures of the T2Cu site in AcNiR starting from a random MD snapshot of Asp98 system. Oxidized state (left) shows two waters coordinated and the reduced state (right) with one water lost from the coordination sphere.**

References

[1] K. Sen, S. Horrell, D. Kelilli, C. W. Yong, T. W. Keal, H. Atakisi, D. W. Moreau, R. E. Thorne, M. A. Hough, R. W. Strange, *IUCrJ* 4, 495 (2017)

3.8 Detecting Molecular Rotational Dynamics Complementing the Low- Frequency Terahertz Vibrations in a Zr-Based Metal-Organic Framework

Matthew R. Ryder et al.

Department of Engineering Science, University of Oxford, Parks Road, Oxford, United Kingdom.

Terahertz (THz) vibrations play a central role in the identification of the structural flexibility of framework materials, such as metal-organic frameworks (MOFs) [1-3]. MOFs are crystalline inorganic-organic materials with long-range ordered porosity at the nanoscale, which have garnered immense scientific and technological interest for engineering innovative applications targeting carbon capture, smart sensors, opto- and micro-electronics, biomedicine, and energy conversion devices [4].

In this work, we report the low-frequency THz dynamics present in a porous Zr-based MOF, designated as MIL-140A. To gain a complete insight into the complicated co-operative framework dynamics, we employed inelastic neutron scattering (INS), synchrotron radiation far-infrared (SR-FIR) spectroscopy, and Raman spectroscopy, all in conjunction with density functional theory (DFT) calculations. This allowed for the discovery of three interesting physical phenomena predicted by quantum mechanical simulations, specifically at under 3 THz (< 100 cm-1): (i) hindered rotational dynamics, (ii) co-operative trampoline-like motions, and (iii) coordinated shearing dynamics.
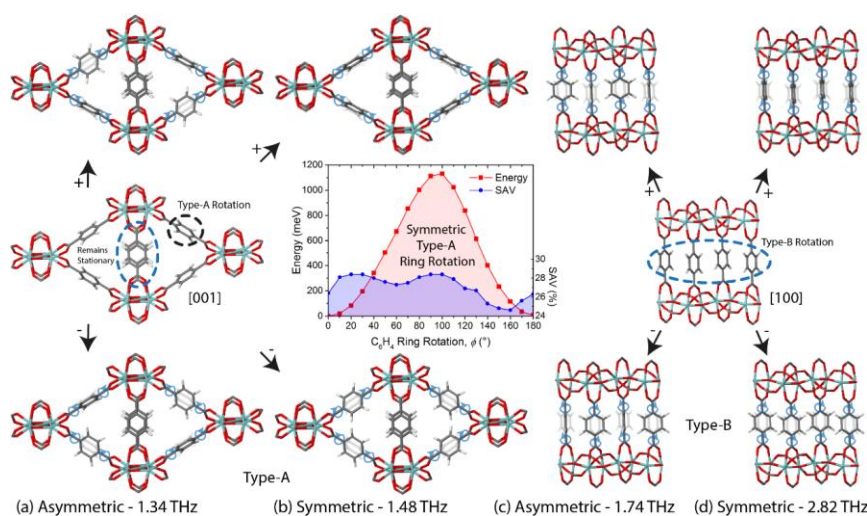
Figure 3.8.1: Hindered phenyl rotations of MIL 140A. (a) Asymmetric and (b) symmetric Type- A rotor-like motions along with (inset) the energy barrier and change in solvent assessable volume (SAV) for the 180o ring rotations during the symmetric Type-A motion. (c) Asymmetric and (d) symmetric Type-B rotor-like motions.

References

[1] M. R. Ryder, B. Civalleri, T. D. Bennett, S. Henke, S. Rudic, G. Cinque, F. Fernandez-Alonso, and J. C. Tan, Phys. Rev. Lett. 113, 215502 (2014).

[2] M. R. Ryder, B. Civalleri, G. Cinque, and J. C. Tan, CrystEngComm 18, 4303 (2016).

[3] M. R. Ryder, B. Van de Voorde, B. Civalleri, T. D. Bennett, S. Mukhopadhyay, G. Cinque, F. Fernandez-Alonso, D. De Vos, S. Rudic, and J. C. Tan, Phys. Rev. Lett. 118, 255502 (2017).

[4] M. R. Ryder and J. C. Tan, Mater. Sci. Technol. 30, 1598 (2014).

### 3.9   DFT simulations of low-dimensional hydrogen-bonded organic crystals

Dominic Fortes

ISIS Crystallography

Following a series of successful CASTEP studies, done using SCARF in 2016 (Fortes *et al.*, 2017a, 2017b, 2017c), my work has diversified to include weakly bonded sulfur-halogen compounds that are likely to be important minerals on the surface of Jupiter's moon Io, and also a range of organic substances. With respect to the latter, the main focus has been on organic crystals in which the hydrogen bonding is confined principally to one or two dimensions. Examples include the dicarboxylic acids, where head-to-tail H-bonding produces 1D chains with only van der Waals interactions between the chains, and compounds based on triazine rings in which interlocking H-bonds form 2D molecular sheets. The consequence of this low-dimensional H-bonding is highly anisotropic elastic properties, these materials being quite stiff along the 1D chain or in the plane of the 2D sheet and highly compressible perpendicular to these directions.

In order to support beam-time proposals, DFT calculations in CASTEP have been done to characterise the elastic anisotropy of candidate materials as a function of pressure at zero K.

For the dicarboxylic acids, single crystal X-ray diffraction from 120 to 300 K shows how the thermal expansion anisotropy varies with chain length and odd/even carbon numbers (Bhattacharya *et al.*, 2013); thus far, a comprehensive series of DFT simulations on succinic acid confirm the extreme elastic anisotropy and its relationship to the molecular packing.

For the layered ring-like organics, simulations have been done on melamine and the co-crystal of melamine with cyanuric acid; the latter is a well-known structural archetype for DNA base pair-like H-bonding motifs (Prior *et al.*, 2013). Additional studies have been done on the carbon-sulfur ring molecule known colloquially as sulflower – octathio[8]circulene, $(C_2S)_8$.
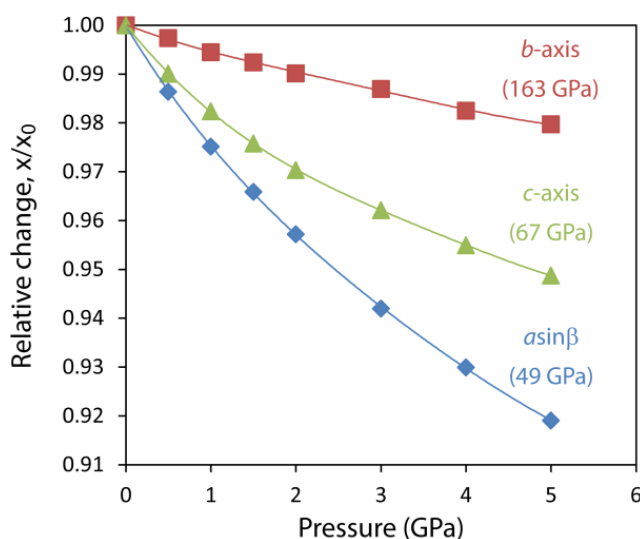
Figure 3.9.1: Relative compression of orthogonal crystallographic directions in melamine from DFT calculations in CASTEP. The zero-pressure linear incompressibilities are indicated.

Due to the interest in melamine as a potential precursor to superhard C–N compounds (Ma *et al.*, 2002), or N-doped carbon nanotubes (Wu *et al.*, 2006), a number of studies have been made to

characterise its high-pressure behaviour. The earliest of these (Ma *et al.*, 2003) observed what was interpreted as a phase transition from the ambient-pressure monoclinic phase to a triclinic phase at 1.3 GPa and then to an orthorhombic phase at 8.2 GPa. Subsequent work has proven contradictory: Raman spectroscopy by Liu *et al.* (2010) and Odake *et al.* (2013) sees no evidence of a phase transition up to 60 GPa; XRS and XRD done by Pravica *et al.* (2010) supports the notion that there are two phase transitions in melamine below 24 GPa. In a subsequent EDXRD study, Pravica *et al.* (2011) made measurements principally at high P <u>and</u> high T, but also collected data at room temperature at 3.5 GPa, which they assert can be indexed with the $P\bar{1}$ cell of Ma *et al.* (2003). All of these interpretations appear to rest on quite subtle peak splittings, or disappearance of shoulders or single small peaks. Given the highly anisotropic elastic properties of melamine (Haussuhl, 2001) and the large pressure increments, I consider it plausible that the so-called phase transitions simply reflect anisotropic peak shifts. The purpose of the DFT calculations (Fig. 1) is to aid in fitting of powder diffraction data from a proposed high-pressure neutron diffraction experiment on PEARL.

References

[1]   Bhattacharya *et al.* (2013) *Cryst. Growth Des*. 13, 3651.
[2]   Fortes *et al.* (2017a) *Acta Cryst. B* 73(1), 33.
[3]   Fortes *et al.* (2017b) *Acta Cryst. B* 73(1), 47.
[4]   Fortes *et al.* (2017c) *Phys. Chem. Min*. 39(5), 419.
[5]   Haussuhl (2001) *Z. Krist*. 216, 339.
[6]   Liu *et al.* (2010) *J. Phys. Conf. Ser*. 215, article 012045.
[7]   Ma *et al.* (2002) *J. Phys. Cond. Matt*. 14, 11269.
[8]   Ma *et al.* (2003) *Chem. Phys. Lett*. 368, 668.
[9]   Odake *et al.* (2013) *High Press. Res*. 33, 392.
[10]   Pravica *et al.* (2010) *High Press. Res.* 30, 65.
[11]   Pravica *et al.* (2011) *Diamond Rel. Matt.* 20, 1090.
[12]   Prior *et al.* (2013) *CrystEngComm* 15, 5838.
[13]   Wu *et al.* (2006) *Diamond Rel. Matt.* 15, 164.

3.10 Arrest of Landau damping in the Vlasov–Poisson system

J. T. Parker[1] and P. J. Dellar[2]

[1] *Science and Technology Facilities Council, Rutherford Appleton Laboratory, Harwell Campus, Didcot, UK*

[2] *OCIAM, Mathematical Institute, University of Oxford, Andrew Wiles Building, Radcliffe Observatory Quarter, Woodstock Road, Oxford, UK*

Introduce an infinitesimal sinusoidal perturbation into the electric field of a electron plasma and the perturbation will decay, even in the absence of explicit collisions or dissipation. This is Landau damping, a fundamental result in plasma physics. In the long time limit, the electric field behaves like $E \sim e^{-i\omega t}$, where the complex frequency $\omega = \omega_L + i\gamma_L$ satisfies a linear dispersion relation derived by Landau [3]. The frequency depends on the wavenumber of the initial perturbation, k, but damping is always observed, $\gamma_L < 0$ (except for $\gamma_L = 0$ for $k = 0$).

This scenario is described by the Vlasov–Poisson equations, a partial differential equation system for the distribution function $F(x,v)$ – the number density of electrons with a given position x and velocity v – and a consistent electric field. The behaviour changes when finite perturbations are considered, and the nonlinearity in the Vlasov equation becomes significant. There is still an initial phase where the electric field decays as in linear Landau damping. But then after a time $t \sim 1/|\gamma_L|$, the system enters a secondary phase where the behaviour depends on the initial amplitude of the electric field perturbation, ε. For very small ε, the electric field continues to decay at the Landau rate. For slightly larger perturbations, the electric field still decays, but with a decay rate smaller than the Landau rate. The decay rate decreases with increasing ε, until the "critical amplitude", $\varepsilon*$, is reached, and the long-time behaviour of the system is a pure oscillation, without growth or decay. For ε yet larger, the electric field grows in the secondary phase, before saturating and performing nonlinear oscillations. The electric field for four ε corresponding these behaviour are shown in Figure 3.10.1(a), for a set of nonlinear simulations performed on SCARF with the code SpectroGK [4, 5].

The behaviour of the Vlasov–Poisson system around the critical amplitude $\varepsilon*$ is the topic of much recent study. Various properties are known, such as power laws relating $(\varepsilon - \varepsilon*)$ to saturation amplitude [1, 2] and to the extrema of the electric field envelope and the times that these are attained [7]. But hitherto there was no quick, accurate way of determining the critical amplitude $\varepsilon*$ without performing a series of expensive nonlinear simulations.

We have developed a quasilinear theory for the Vlasov–Poisson equations based on properties observed in our numerical solutions. The Fourier spectrum is steep, so one can approximate the spatial dependence of the distribution function with only two Fourier modes: $F_1(v)$, the mode corresponding to the initial perturbation, and $F_0(v)$, the mode corresponding to $k = 0$ which experiences no Landau damping. Moreover, we show (and verify in simulations) that in the long time limit $F_0(v) \rightarrow F(v)/\varepsilon^2$ where $F(v)$ is the same function for all $\varepsilon < \varepsilon*$. This allows us to reduce the two-mode system to a linear system for $F_1(v)$. This system has a dispersion relation which is the same as the Landau dispersion relation, but with an additional term that depends on ε and $F(v)$.

Therefore, we need only one nonlinear simulation to determine F(v) – after this, we solve a simple dispersion relation to find the growth rate for each ε. The growth rates produced by our dispersion relation method are in excellent agreement with growth rates taken from Vlasov–Poisson simulations, as shown in Figure 3.10.1(b). Our method also allows us to quickly perform parameter scans, and we have verified that it continues to work varying parameter of the system, like the wavenumber of the initial perturbation, k, and the electron thermal velocity. Moreover, the quasilinear theory we have developed can be extended in future work to investigate more complicated nonlinear regimes.
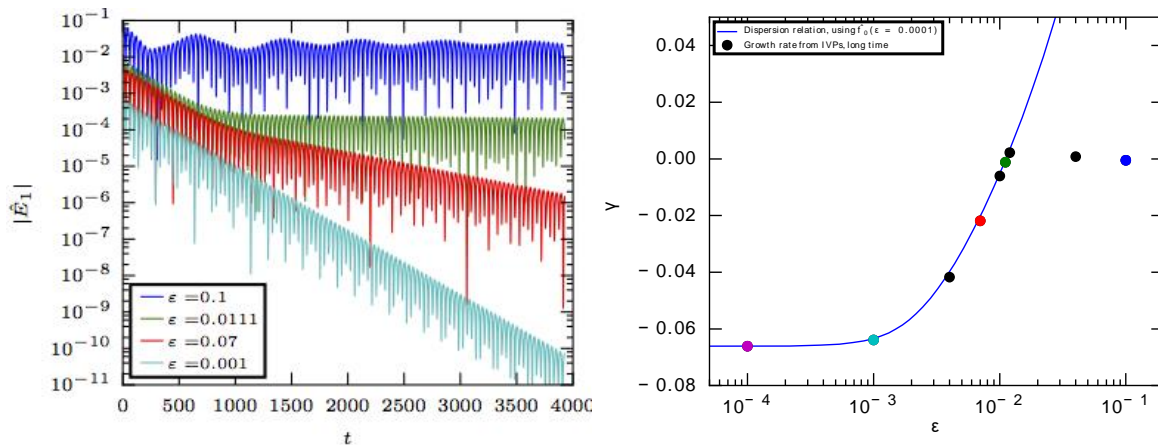
Figure 3.10.1: Evolution of the electric field for four perturbation amplitudes ε. Small perturbations (e.g. ε = 0.001) decay at the Landau rate, while large perturbations (e.g. ε = 0.1) exhibit nonlinear oscillation. The value ε = 0.011 is around the critical amplitude where Landau damping is arrested. (b) The growth rate of the secondary phase γ against initial perturbation ε calculated with our dispersion relation method (line) and from nonlinear Vlasov–Poisson simulations (points). There is excellent agreement up to the critical amplitude ε$_*$ = 0.0111. Each point in (b) took the same computing time to produce as the whole dispersion relation line.

References

[1] M. Brunetti, F. Califano, and F. Pegoraro. Asymptotic evolution of nonlinear Landau damping. Phys. Rev. E, 62:4109–4114, 2000.

[2] C. Lancellotti and J. J. Dorning. Critical initial states in collisionless plasmas. Phys. Rev. Lett., 81:5137–5140, 1998.

[3] L. D. Landau. On the vibrations of the electronic plasma. J. Phys.-U.S.S.R., 10(25):25–34, 1946.

[4] J. T. Parker. Gyrokinetic simulations of fusion plasmas using a spectral velocity space representation. DPhil Thesis,   University of Oxford, arXiv:1603.04727, 2015.

[5] J. T. Parker and P. J. Dellar. Fourier–Hermite spectral representation for the Vlasov–Poisson system in the weakly collisional   limit. J. Plasma Phys., 81(2), 2015.

[6] J. T. Parker and P. J. Dellar. Arrest of Landau damping in the 1+1D Vlasov–Poisson system, 2017. In preparation.

[7] C. F. Rupp, R. A. López, and J. A. Araneda. Critical density for landau damping in a two-electron-component plasma.   Phys. Plasmas, 22(10):102306, 2015.

3.11   Modelling catalysts for the decomposition of ammonia in sustainable energy applications.

Phillip Marks[1], Keith Refson[2,3] and Bill David[1,3]

[1] *Inorganic Chemistry, University of Oxford, South Parks Road, UK.*

[2] *Department of Physics, Royal Holloway, University of London, Egham Hill   Egham, Surrey, UK.*

[3] *ISIS Facility, STFC Rutherford Appleton Laboratory, Chilton, Didcot, UK.*

The development of energy storage materials is a key scientific challenge of this century, with an ever increasing energy demand which must be met while reducing our reliance on fossil fuels. Hydrogen is an excellent option for replacing fossil fuels because of its high gravimetric energy density and zero CO_2 emission combustion. However, the practicality of storing hydrogen both reversibly and at low cost at high volumetric energy density, is a key technical challenge. Ammonia can be used as a carbon-free energy vector for hydrogen, the compound's high gravimetric (17.8 wt. %) and volumetric (121 kg/m3) hydrogen densities, coupled with moderate conditions required for storage, make it a promising energy storage material. Low-cost, high activity catalysts are needed to crack ammonia and liberate hydrogen in order to enable its widespread use. This project aims to use computation to further the development and understanding of these catalyst materials.

A new class of low-cost catalysts for cracking ammonia based on lightweight metal imide/amide has been identified [1,2]. While in-situ powder diffraction and isotope exchange methods have provided valuable insights into the active form of these catalysts, an atomic-scale mechanistic understanding of how ammonia interacts and decomposes with these materials can only be obtained from simulation. Metal hydrides have been shown to be of central importance to the decomposition of NH_3 in of Li-N-H systems [2] and LiH has also recently been shown to promote ammonia synthesis catalysis as a N transfer catalyst [3]. In this work we developed a simple model using CASTEP in order to characterize the different bulk and surface behaviours of various metal hydrides (M=Li,Na,K,Rb, Cs), and from this, low energy configuration of materials were identified. Trends in these configurations have been identified and subsequently we are investigating how structure affects the reactivity. Preliminary interactions have shown ammonia to interact in a highly localized manner with the catalyst materials, Fig. 3.10.1. refers to the direction of displacement associated with the individual elemental movement.

(a)   (b)
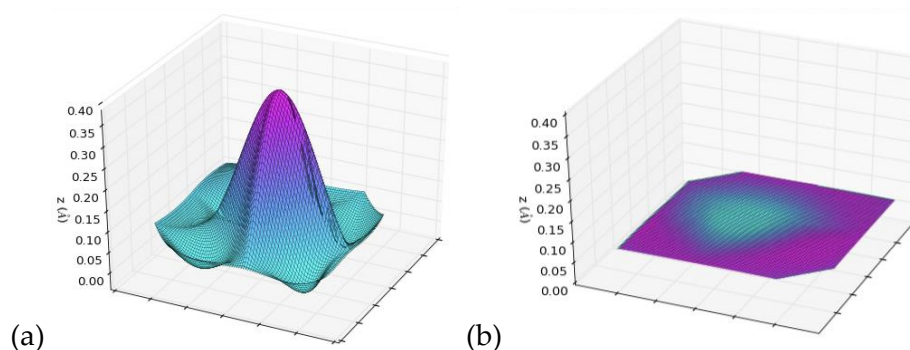
Figure 3.11.1: Lithium hydride surface layer, separated into (a) lithium and (b) hydrogen atoms using an interpolated mesh to show atomic movement. The major peak in lithium corresponds to a localised displacement of the metal towards ammonia (not shown, directly above the major

peak). The z-axis corresponds to the atomic displacement from the relaxed surface without ammonia and colour-map

Reactions of ammonia on the surface of a range of lightweight catalyst materials based on group I and II metals are to be investigated through both simple line minimization algorithms and ab initio molecular dynamics. It is hoped this work by providing a better understanding of the mechanisms for ammonia cracking will inform the experimental development of catalysts, in the pursuit of practical energy applications for ammonia. This work would not be possible without the resources made available by SCARF.

References

[1] W. I. F. David et al., J. Am. Chem. Soc., 2014, 136, 13082-13085.

[2] J. W. Makepeace et al., M, Phys. Chem. Chem. Phys., 2014, 16, 4061-4070.

[3] P. Wang et al., Nat. Chem., 2017, 9, 64-70.

3.12   The electronic structure and magnetic properties of Ca3MnNiO6

W. Wu

University College London

Quasi-one-dimensional spin chains can be found in Ca_3MnNiO_6 (CMNO), which is of fundamental interest for condensed matter physics. The magnetic structure includes spin- Ω`spin interactions and spin-orbit interactions (SOI), which will determine the magnetic properties of the materials, i.e., whether CMNO has one-dimensional or three-dimensional magnetic structure. Inelastic Neutron scattering (INS) and other experimental techniques can be used to observe the spectra showing different types of interactions among spins. Recently, the INS spectra have been measured by Dr. T. Adroja (my long-term collaborator) at Rutherford Appleton Laboratory, which have shown rich physics, qualitatively bearing intra-chain, inter-chain, and even spin anisotropy (arising from SOI). However, this is not sufficiently clear until we have performed first-principles calculations for the electronic structure and magnetic properties of CMNO, combined with INS simulations using SpinW software.

In the last few months I have been performing first-principles calculations for CMNO using Quantum Espresso code on SCARF. Two types of calculations have been done for this compound, including (i) collinear (without SOI) and (ii) non-collinear (with SOI). The calculation results are in agreement with the previous experimental results on CMNO. The table attached shows that we have analyzed the electronic structure and magnetic properties by using different Hubbard-U and Hubbard-J0 parameters in method (i), and (ii). The computed anti-ferromagnetic intrachain nearest-neighboring (NN) exchange interaction without SOI range between 150 and 245 K (in contrast with a very weak inter-chain coupling), which is in a good agreement with the recent INS experiments. The computed intrachain NN exchange interaction with SOI is 360 K (anti-ferromagnetic), which is still qualitatively in agreement with experiments.
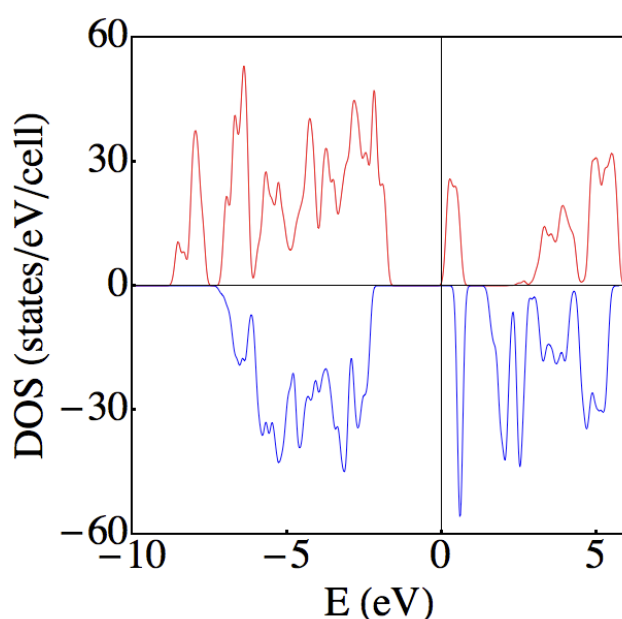

Figure 3.12.1: Density of states of CMNO FM state

3.13   The electronic structure and magnetic properties of Ba6Cr2S10

W. Wu

University College London

Compounds formed by quasi-one-dimensional (1D) spin chains have attracted much attention in the past few decades mainly because of their exotic magnetic properties arising from reduced dimensionality; the nature of magnetic excitations are drastically different from the three-dimensional (3D) system. AMX_3 and $Ae_3MM'O_6$ are spin-chain systems that have been extensively studied, in which A is alkali metal, Ae alkali earth metal, M/ M′ transition metals, and X halogen atom. In these systems, the intra-chain exchange interaction is usually more than one orders of magnitude larger than the inter-chain exchange interaction, thereby exhibiting quasi 1D character. In a 1D spin chain, there exists no long-range magnetic order as predicted by the Mermin-Wagner theorem. However, in a quasi 1D spin chain system, the three-dimensional magnetic ordering can occur because of the weak inter-chain interacting, which governs the magnetic phase transition. Above the phase transition temperature, although the long range order has not formed, the short range order within the chains has gradually developed due to the intra-chain interaction. For example, in $CsNiCl_3$, the intra-chain interaction (1.43 meV) is 57 times larger than inter-chain (0.025 meV). It undergoes a antiferromagnetic transition with $T_{N1} \sim 4.4K$ and $T_{N2} \sim 4.84K$ with the help of weak inter-chain interaction. In its disordered phase (above T_N), it is a good approximation to a 1D Heisenberg antiferromagnet, and the Haldene gap for integer-spin chains has been evidenced by the spin wave measurement.

We report a new spin chain compound $Ba_6Cr_2S_{10}$. The distance of adjacent spin chains is 9.1125 Å, larger than the above two systems. Thus, it further approaches to one dimensionality in the view of crystal structure. $Ba_6Cr_2S_{10}$ undergoes a canted antiferromagnetic phase transition at 43K and presents large magnetic frustration. The spins are confined within ab-plane and ferromagnetic ordered, which avoids the magnetic frustration arising from triangular lattice.

I have been computing the electronic structure and magnetic properties by using the non-collinear module in Quantum Espresso code. Based on the current calculations, the lowest spin alignments show the spins on Cr are all in the xy plane (as shown in the figure below, 90 degrees (the lowest energy) correspond to in the xy plane), which is in a good agreement with the magnetic measurements carried out at Rutherford Appleton Laboratory led by Prof. Wang and Dr. Adroja. The exchange interactions have been calculated by comparing the energy differences between a set of spin configurations. The intrachain couplings have been computed, which turns out to be anti-ferromagnetic (~160 K) with spins in the xy plane. The computed inter-chain coupling turns to be ferromagnetic (~ 2 K), which is much weaker than the intra-chain couplings (two orders smaller). These calculations are in a good agreement with the current experimental observations that show a strong 1D behavior of this compound.
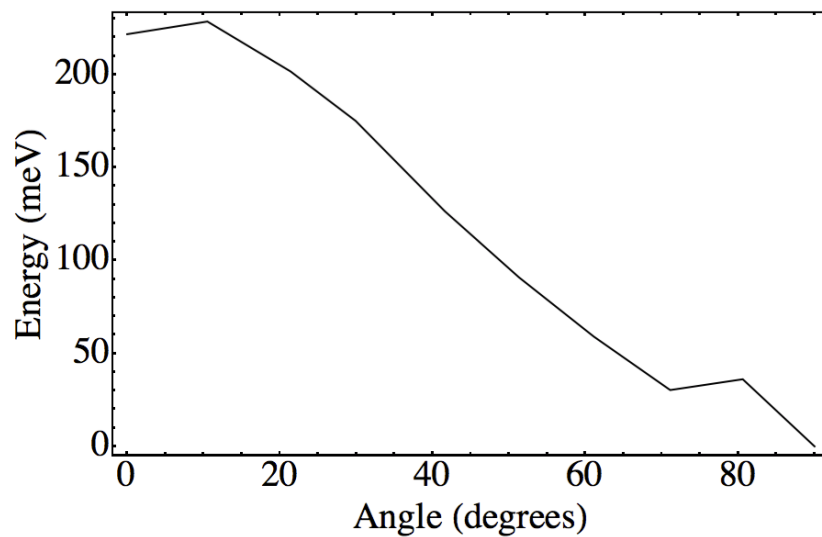
Figure 3.13.1: Total energies as a function of polar angles, which suggests the lowest-energy spin configuration is in-plane (x-y).

3.14 Muon implantation sites and contact hyperfine field with density functional theory based simulations.

Ifeanyi John Onuorah, Pietro Bonfà, Roberto De Renzi

Dipartimento di Scienze Matematiche, Fisiche e informatiche, Università di Parma, Parco Area delle Scienze, 7/A 43124 Parma, Italy

Density functional theory (DFT) based computational methods for the calculation of the muon stopping sites and local fields are of great value in the experimental data analyses of positive Muon spin rotation and relaxation spectroscopy experiments. The implanted muon thermalizes at interstitial sites in lattices. The local magnetic field at these points is acquired in muSR experiments by collecting Larmor precession frequencies and microscopic information on the magnetic properties of the material under the study can be gathered.

Over the years, we have continued to use Density Functional Theory for the calculation and identification of muon stopping sites in magnetic and superconducting materials [1-6] employing the Quantum Espresso suite of codes [7].

Particularly, for the current year, we have employed the SCARF cluster for the identification of the possible implantation sites for $NaFe_{1-x}Cu_xAs$(x=0 and x = 0.5), where the possible microscopic coexistence of magnetism and superconductivity was studied with muon spin rotation and relaxation spectroscopy [9,10]. Within plane-wave based approach and using opportunely sized supercells, the possible interstitial positions occupied by the muon have been identified by relaxing the lattice structure in the presence of the charged impurity. The outcome of this work is shown in Figure 3.14.1. The search for muon sites in each of the structures was carried out independently resulting in similar candidate sites for both the stoichiometric and the Copper substituted structures, except for a slight drift away from the high symmetry positions in the Cu-doped sample. The local field calculations of some of the candidate muon stopping sites are consistent with the experimental observation of various precession frequencies in the zero field µSR spectra in low-doped $NaFe_{1-x}Cu_xAs$. The candidate site locations do not all directly correspond to observed muon sites, since the muon localization is a metastable epithermal kinetic phenomenon that cannot be determined by a mere minimum energy criterion, further calculations including the effect of the muon light mass are needed. In addition, DFT calculations allowed us to confirm the experimental findings in the structure of the pnictides involving a shift away from the high symmetry positions of the Na and As atoms as the Fe-Cu stripes are formed. A similar study was conducted in two compositions of $Yb_2Pd_2In_{1-x}Sn_x$ [D].
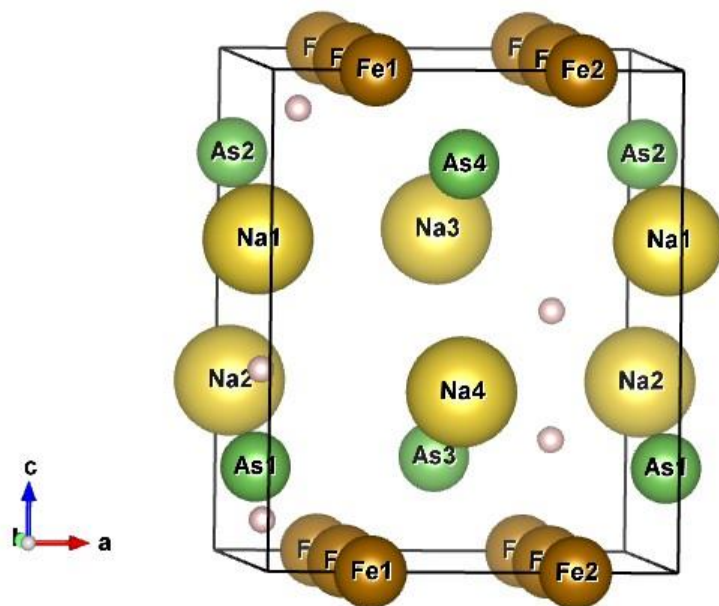
Figure 3.14.1: Showing the five candidate muon stopping sites (pink balls) in NaFeAS

Also the computational resource at SCARF has allowed us to benchmark and set out a systematic approach for the estimation of the muon contact hyperfine field in metals [8, B, C]. The contact field is one of the contributions describing the magnetic interaction between the muon and the magnetic electronic ground state and it originates from a net electronic spin polarization at the muon interstitial site. The contact hyperfine contribution to the muon local field for the transition elemental metals and some of the cubic B20 itinerant chiral magnets (MnSi [4] and MnGe[5]), which are of current interest for skyrmion phase identification, has been calculated. The DFT approach allows us to quantify, in good agreement with experiment (see Figure 3.14.2), the spin density and in turn contact field at the muon interstitial site for these materials.
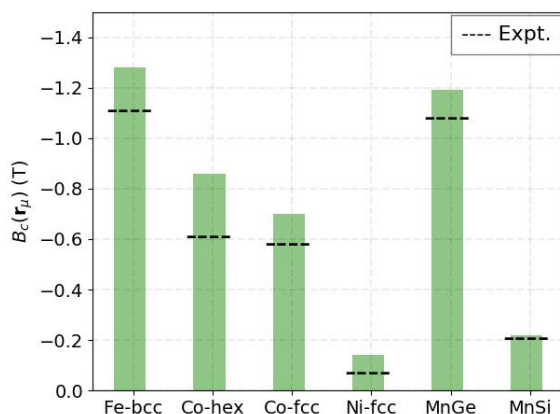
Figure 3.14.2: Calculated Contact hyperfine field at muon interstitial sites Bc(rμ) in Tesla (green bars), with black dotted lines indicating experimental results. The little over-estimation in the contact field, is due to the effect of the light mass of the muon which is not included yet.

References

[1] P. Bonfà, et al, J. Phys. Chem. C119, 4278 (2015).

[2] J.S. Möller, et al, Phys. Rev. B 87, 121108R (2013).

[3] P. Bonfà, et al, J. Phys. Soc. Jpn. 85, 091014 (2016).

[4] A. Amato, et al, Phys. Rev. B 89, 184425 (2014).

[5] N. Martin, et al, Phys. Rev. B 93, 174405 (2016).

[6] R. Khasanov, et al, Phys. Rev. B93, 180509(r) (2016).

[7] http://www.quantum-espresso.org

[8] I. J. Onuorah, et al. Hyperfine field prediction in metals by DFT (in preparation)

[9] D. R. Parker, et al. Phys. Rev. Lett. 104, 057007

[10] S. C. Cheung, et al. Disentangling superconducting and magnetic orders in NaFe 1−x Ni x As using muon spin rotation(in preparation)

3.15 Combining AIMD and Neutron Scattering Data based EPSR Simulations to uncover Water Participation in Catalysis

Nicole Holzmann[1], Silvia Imberti[2], Franco Scalambra[3], Antonio Romerosa[3], Leonardo Bernasconi[1]

[1] SCD, STFC Rutherford Appleton Laboratory, Harwell Oxford, Didcot, UK
[2] ISIS, STFC Rutherford Appleton Laboratory, Harwell Oxford, Didcot, UK
[3] Área de Química Inorgánica-CIESOL, Universidad de Almería, Almería, Spain

The advantages of using water as a solvent in catalysis are obvious: it is abundantly available, cheap and easily recyclable. However, the majority of homogeneous catalytic processes mediated by metal complexes take place in organic solvents which is due to the insolubility of many complexes and the easy decomposition of most of the catalytically active metal complexes in water. In order to shed light on the reaction mechanism of catalytic processes in water two things are of key interest: the complex/substrate conformation and the interaction with water. Aqueous solutions pose a challenge for many classical analytic methods. Experimental techniques like NMR or theoretical approaches like DFT can give some indications on complex conformation. By taking into account the electronic structure, AIMD (*ab initio* molecular dynamics) simulations with explicitly described water are able to give a detailed picture of coordination of single water molecules, their influence on solute conformation and their evolution over time. Small angle neutron scattering is capable of detecting hydrogens and is predestined to examine molecules in water. The EPSR (Empirical Potential Structure Refinement) simulations use data from the neutron scattering measurements to refine structure and determine probabilities of water distribution.
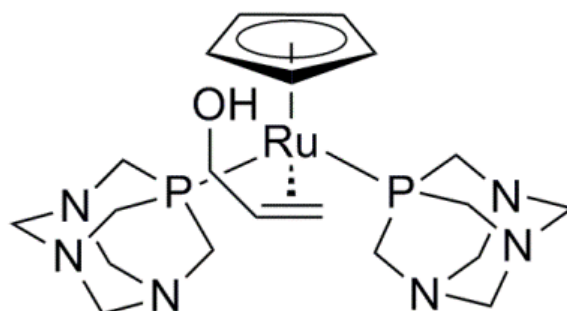
Figure 3.15.1: Schematic representation of [RuCp(PTA)2]+ with 1-propen-3-ol

On the example of the water soluble complex $[RuCp(H_2O\text{-}\kappa O)(PTA)_2]^+$ (PTA = 1,3,5-triaza-7-phosphaadamantane) (Figure 3.15.1 with substrate 1-propen-3-ol) that catalyses the isomerization of allylic alcohols to aldehydes or ketones and that shows increased catalytic efficiency in the presence of more than a stoichiometric amount of water [1,2], we combined AIMD and EPSR simulations (Figure 3.15.2) that can aid identifying catalyst and substrate conformation and water participation in aqueous solutions.

This way we were able to identify the factors responsible for the stabilisation of a specific conformer in water solution and we could demonstrate the direct involvement of water molecules in the formation of this species. In particular, we showed that long-lived bonded chains of water molecules play a crucial role in influencing the conformation and, potentially, the chemical reactivity of the complex [3].
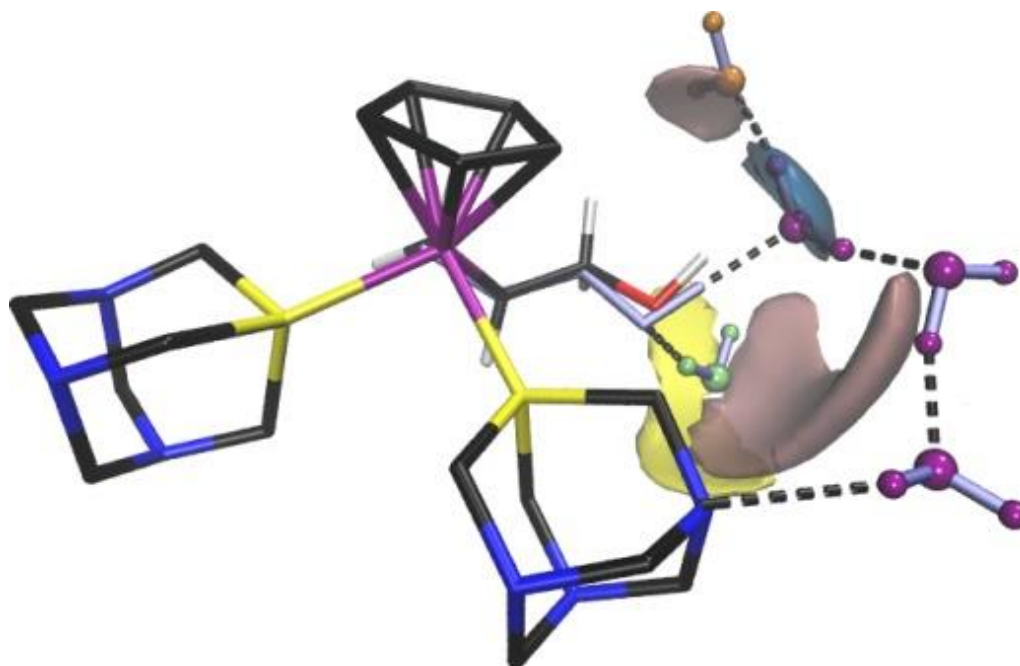
Figure 3.15.2: Overlay of AIMD snapshot and EPSR spatial density functions of water

Our study demonstrated that a combination of AIMD simulations and total neutron scattering is a powerful tool for identifying unusual solvation motifs for complex solutes and for studying the role of individual water molecules in the stabilisation of reaction intermediates. This is of particular importance as aqueous solutions often pose a challenge to many classical analytical methods. Our approach provides a potentially general method for characterising the conformation of key intermediates in catalytic reactions in water solution, as well as for studying how solute-solvent interactions affect the reaction outcomes, and open new research lines also for the study of catalytic reactions in other solvents.

Geometry optimisations of different substrate-catalyst conformers, charge analysis and short preliminary AIMD simulations were carried out on SCARF before moving the molecular system to a National Supercomputing Service for creating the computationally more expensive trajectories.

References

[1] M. Serrano-Ruiz, P. Lorenzo-Luis, A. Romerosa, A. Mena-Cruz, *Dalton Trans.* 42, 7622 (2013).
[2] F. Scalambra, M. Serrano-Ruiz, A. Romerosa, *Dalton Trans*. 46, 5864 (2017).
[3] F. Scalambra, N. Holzmann, L. Bernasconi, S. Imberti, A. Romerosa, *ACS Catalysis, submitted* (2017).

3.16 Computational Prediction of Muon Stopping Sites in Silicon.

L. Liborio, S. Sturniolo, D.B. Jochym, B. Montanari

Theoretical and Computational Physics Group, Scientific Computing Department, RAL, STFC, UK

There are some experimental techniques that can determine the muon stopping sites, but these techniques are limited to certain specific cases, and combinations of experiments and calculations have been applied to this problem with mixed success. In this work, we propose a method that combines machine learning techniques with a computational technique known as ab initio random structure searching (AIRSS). The example presented here focuses on the paramagnetic states formed by muons in pure Silicon.

The method first applies AIRSS to generate a number of Si super-cell structures where the muon is placed in random positions, and then uses machine learning techniques to classify these structures combining energetic and geometric parameters. This classification is motivated by our interest in all potential muon stopping sites and not just the lowest energy one. As a result of this process, a set of clusters is formed with structures that are grouped around potential muon stopping sites.

Figure 3.16.1 shows the clusters that our method obtained for Si. The clusters are represented by circles whose diameter indicates the number of structures contained in each cluster. Muons cluster due to the actions of the attraction basins formed around the potential energy surfaces' local minima of each cluster. A small standard deviation for the average energy of a cluster is an indication of a consistent cluster, with structures that are more similar to each other than the structures around a site with a larger standard deviation. Hence, sites with small standard deviations are likely to be representing a local energy minimum and, consequently, a muon stopping site. Furthermore, as our methodology is based on DFT calculations that are performed at 0K, these stopping sites are likely to be low-temperature stopping sites.

In Figure 3.16.1, the largest standard deviation is ≈0.001 eV, which indicates that all of the clustering sites are potential muon stopping. Experimental evidence suggests that, at low temperatures (T≤100K), the system cannot be in thermal equilibrium between all possible sites and charge states and, as muonium centres are never formed in sufficient concentration, the muonium centres never equilibrate among themselves. Under these conditions, our purely theoretical method predicted the experimentally well-known "bond centered" (Mu_{BC}) and "tetragonal" (Mu_T) stopping sites of muonium in Si, which is in agreement with experimental results.
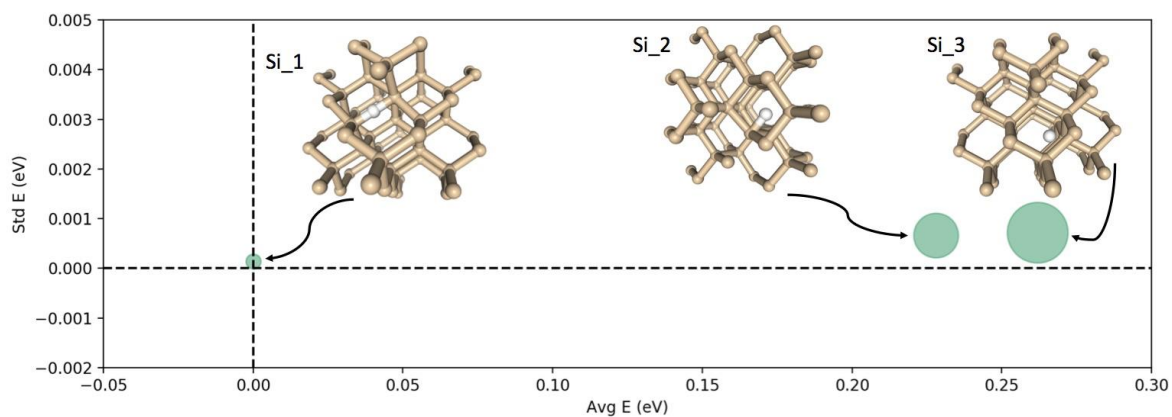
Figure 3.16.1: 3 circles representing the 3 clusters obtained by our method. The crystalline structures shown correspond to the most stable structure in each of the clusters. The diameter of each circle represents the number of structures contained in each cluster. The x coordinate of the centre of each one of the circles indicates the average energy of the corresponding cluster - relative to the lowest energy structure in the cluster-, while the y coordinate of the centre indicates the standard deviation of the average energy of that cluster.

3.17 Exploring the Temperature Dependent Solid-State ALC Spectrum of the C6H6Mu• Radical with Ab-Initio Simulation Techniques

S. Sturniolo[1], L. Liborio[1], F.L. Pratt[2], S.P. Cottrell[2], D.B. Jochym[1], B. Montanari[1]

[1] *Theoretical and Computational Physics Group, Scientific Computing Department, RAL, STFC, UK*
[2] *Muons Group, ISIS, RAL, STFC, UK*

Longitudinal field Avoided Level Crossing (ALC) is a suitable technique for the study of organic radicals. The ALC spectrum can be used to estimate the values of HFCCs and, in particular, the ALC spectrum of crystalline benzene is found to exhibit multiple complex features that strongly depend on temperature. In this work, a number of different computational techniques were used in conjunction to explain this behavior.

Benzene, (C_6H_6), is solid under 278.6 K. It forms a crystal with four C_6H_6 molecules per unit cell with space group *Pbca*. Inside the crystal, muonium will bond with a benzene ring. This bond breaks one of the double bonds between carbons and leaves one unpaired electron that couples, via hyperfine interaction, to both the muon and the Hydrogens in the molecule. While in an isolated C_6H_6 molecule all possible bonding sites would be equivalent, in crystalline C_6H_6 there are six inequivalent positions, which are nonetheless related by symmetry. The hydrogen that is bonded to the same carbon as the muon is called the 'ipso hydrogen'. Its role in determining the final ALC spectrum is especially important, as two transitions can give rise to ALC lines - the 1-quantum muon spin flip (called the $\Delta 1$ line) and the 0-quantum muon-ipso hydrogen flip-flop (or $\Delta 0$ line).
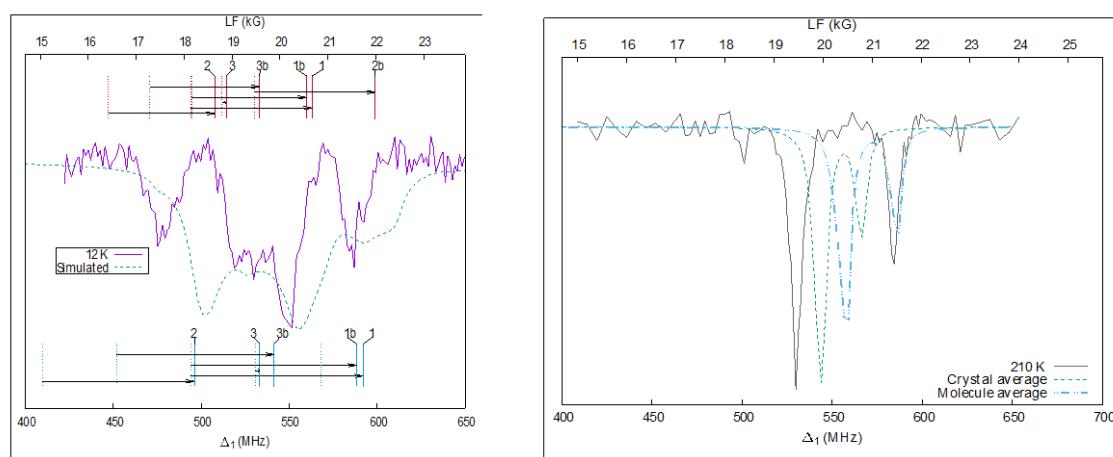
Figure 3.17.1: (Left) Experimental ALC spectrum for solid benzene at 12 K (solid line) and static simulated spectrum (dashed). The red lines on the top of the plot represent the predicted positions for the $\Delta 1$ peak at the various sites, before (dashed) and after (solid) the quantum corrections. The ones at the bottom are the same for the $\Delta 0$ peaks. (Right) Experimental ALC spectrum for solid benzene at 210 K (solid line), and simulated spectra with averaged crystal tensors (dashed line) and single molecule tensors (dash and dot).

In this work, we focused on the experimental ALC spectrum for benzene at 12 K and at 210 K. These are considered as the low and high temperature limits for the main dynamical processes affecting the spectrum, and figure 1 shows the experimental and calculated ALC spectrums.

Overall, our methodology can be used to calculate the ALC spectrum at different temperatures for an organic radical. The method gives predictions that are reasonably close to the experimental results, taking into account corrections for quantum and classical dynamical effects. Ongoing work is aimed towards refining this method and eventually delivering tools that would enable a larger audience of users to apply it in a general way as an aid to the interpretation of measured ALC spectra for this class of compounds.

3.18 The structures of liquid pyridine and naphthalene: the effects of heteroatoms and core size on aromatic interactions

T. F. Headen[1], P. L. Cullen[2], R. Patel[2], A. Taylor[2], N. T. Skipper[2]

[1] ISIS Neutron Facility, STFC Rutherford Appleton Laboratory, Harwell Campus, Didcot, Oxon, UK
[2] University College London, Dept. Physics and Astronomy, Gower Street, London, UK

Aromatic intermolecular interactions are of fundamental importance across the chemical sciences, for example in biomolecular recognition, crystal engineering, macromolecular interactions, carbon nanostructures, petroleum phase behaviour, and solvation by common organic solvents. Total neutron scattering from the SANDALS instrument at ISIS has been used to determine the detailed liquid-state structures of the aromatic liquids pyridine (at 25°C) and naphthalene (at 85°C). Analysis of the data using Empirical Potential Structure Refinement (EPSR) was conducted in part on SCARF. The additional computational resources facilitated simulations to investigate how significantly the structural features observed in the simulations are present in the experimental data. The EPSR analysis has allowed us to interrogate the full six-dimensional spatial and orientational correlation surfaces in these systems, and thereby to deduce the fundamental effects of a heteroatom and aromatic core-size on intermolecular π-π interactions. We found that the presence of a nitrogen heteroatom, and concomitant dipole moment, in pyridine induces surprisingly subtle departures from the structural correlations observed in liquid benzene: in both cases the most probable local motif is based on perpendicular (edge-to-face) intermolecular contacts, while parallel-displaced configurations give rise to a clear shoulder in the correlation surface. However, the effect of the heteroatom is revealed through detailed analysis of the intermolecular orientational correlations. This analysis shows a tendency for neighbouring pyridine molecules to direct one meta- and one para-hydrogen towards the neighbouring aromatic π-orbitals in edge-to-face configurations (Figure 3.18.1 right), while head-to-tail alignment of adjacent nitrogen atoms is favoured in face-to-face configurations. In contrast to this, increasing aromatic core size from one to only two rings has a clear and profound effect on the π-π interactions and liquid structure. Our experiments show that naphthalene-naphthalene contacts are dominated by parallel-displaced configurations (Figure 3.18.1 left), akin to those found in graphite. This marks a fundamental difference with the structure of liquid benzene, in which perpendicular geometries are favoured.
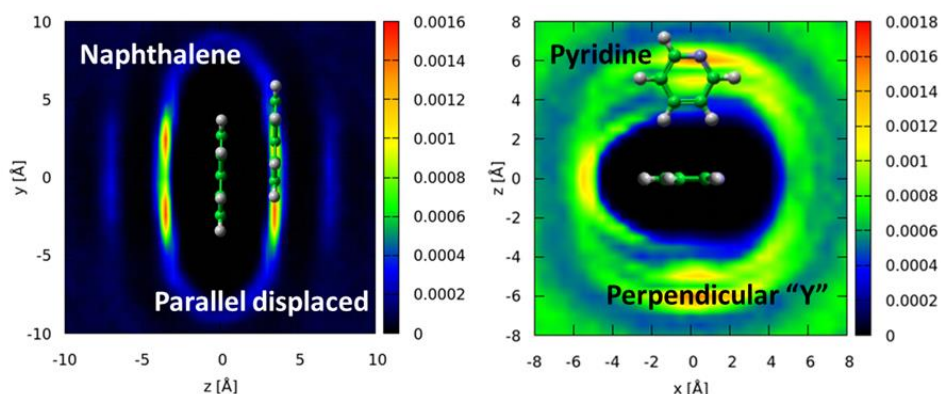
Figure 3.18.1: Two-dimensional cut-through spatial density functions for: parallel molecules in liquid naphthalene, showing preference for parallel-displaced configurations (left), and; perpendicular molecules in liquid pyridine showing preference for "Y-shaped" configuration with meta- and para-hydrogens pointing towards the aromatic ring (right).

3.19   Vibrational Spectroscopy of Organic Photo-Voltaic Materials PCBM

Sanghamitra Mukhopadhyay,[1,2] Jeff Armstrong[1,3], Fernando Bresme[3], and Felix Fernandez-Alonso[1,4]

[1] *ISIS Facility, Rutherford Appleton Laboratory, Chilton, Didcot, Oxfordshire*
[2] *Department of Materials, Imperial College London, Exhibition Road, London*
[3] *Department of Chemistry, Imperial College London, Exhibition Road, London*
[4] *Department of Physics and Astronomy, University College London, London*

PCBM (Phenyl-C61-butyric acid methyl ester) is widely known as the most promising electron-acceptor material for solution processed organic solar photovoltaic devices (PVDs) [1]. It is a fullerene derivative with a very interesting and distinct set of physical properties. It has been reported that for devices with a thickness of 200 nm, PCBM and poly(3-hexylthiophene-2,5-diyl) blends can achieve solar-energy harvesting efficiencies of up to 10%. One of the key factors for PCBM's success in such devices is the ability to optimize its structure and morphology through solvent and thermal annealing. Classical molecular-dynamics simulations have recently shown that the resultant structure of solid and amorphous PCBM is very dependent on the solvent and temperature annealing process used in its synthesis. It has been also recently shown experimentally that films of PCBM have the lowest thermal conductivity of any known solid. Atomistic knowledge of this material is thus important to understand the microscopic origin for this industrially important material.

We have performed electronic structure calculations of PCBM using first principles DFT. Plane wave basis set and norm conserving pseudo potentials are used as implemented in CASTEP code. A geometry optimised monoclinic crystal with P_21/C symmetry and space group number 14 is used for all calculations. The unit crystal consists of four PCBM molecules, which comprises of 352 atoms. Geometry optimisations are done using PBE+D following Grimme formula of dispersion corrections agree within 1% of its structure measured experimentally. Vibrational calculations are done using linear response theory as implemented in CASTEP code. The atom projected vibrational densities of states (VDOS) are compared with experimentally obtained inelastic neutron scattering (INS) spectra and have produced satisfactory agreement. The computed IR spectra are also compared well with experimentally obtained spectrum. These calculations are executed on SCARF computers using 256 processors for few weeks.
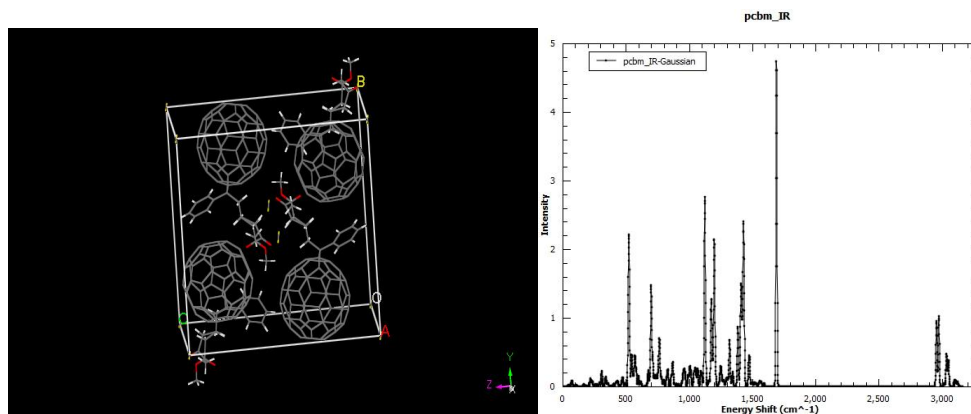
Figure 3.19.1: Left: Unit cell of PCBM, Right: IR spectrum of PCBM calculated using DFT+D and linear response.

Results show that IR and INS spectrum of PCBM is very different from that of C-60, which is the main building block of PCBM. At low energy transfer region (up to 500cm^{-1}) C-60 related peaks are dominated, but from medium (up to 2000cm^{-1}) to high (up to 3200cm^{-1}) energy transfer region the hydrogen rich tail of PCBM dominates.

Recently we have shown that the tail of the PCBM is very reactive and melts before its head C-60 [2]. Simulations help us to understand the microscopic nature of the dynamics of head and tail separately [3]. This knowledge will help to design the promising material further.

References

[1] N. Asim, K. Sopian, S. Ahmadi, K. Saeedfar, M. A. Alghoul, O. Saadatian and S. H. Zaidi, Renewable Sustainable Energy Rev., 16, 5834 (2012).
[2] J. Armstrong, S. Mukhopadhyay, F. Bresme and F. Fernandez-Alonso, Phys.Chem.Chem.Phys. 18, 17202 (2016).
[3] S. Mukhopadhyay, J. Armstrong, F. Bresme and F. Fernandez-Alonso, Phys.Chem.Chem.Phys (to be submitted)

3.20   Effect of Isotopes on Vibrational Properties of Halogenomethanes

Oriol Abril Pla,[1] Daniel Moreno García,[1] Jonathan F. Gebbia[1], Sanghamitra Mukhopadhyay,[2,3] Felix Fernandez-Alonso[2,4] and Josep Lluís Tamarit,[1]

[1] *Grup de Caracterització de Materials, Departament de Física i Enginyeria Nuclear, Universitat Politècnica de Catalunya*
[2] *ISIS Facility, Rutherford Appleton Laboratory, Chilton, Didcot, Oxfordshire*
[3] *Department of Materials, Imperial College London, Exhibition Road, London*
[4] *Department of Physics and Astronomy, University College London, London*

Calorimetrically, halogenomethanes CBr_nCl_{4-n}; n=0;1;2 show a series of thermally induced solid-solid phase transitions that are due to thermally activate rotational degrees of freedom within the crystalline state [1]. Weak intermolecular forces allow this kind of reorientation within crystal. Inelastic neutron scattering spectroscopy (INS) help to understand this weak intermolecular forces. To analyse INS experiment microscopically, first principles lattice dynamics simulations are performed.

Electronic structures calculations are performed using first principles DFT as implemented in the CASTEP code. Plane waves basis sets and norm conserving pseudopotentials are used in these calculations. Dispersion corrected functionals such as PBE+D are used because those predict the structure of this molecular crystal within 2% of the experimentally determined lattice parameters. The unit cell of the crystal consists of 80 atoms and the integration of the Brillouin–Zone are done on 10 irreducible k-points. In calculations of vibrational frequencies at Γ point, linear-response theory is used as implemented in the CASTEP code. A total of 240 vibrational modes present in that crystal comprise of four different symmetries. SCARF computers are used for these calculations using 256 processors for several weeks.

Inelastic neutron scattering (INS) experiments were performed on solid CCl_2Br_2 below 10K on the TOSCA instrument at ISIS. Results show that calculated peaks are redshifted with respect of the experimental ones around by about 10-40 cm^{-1}. The most redshifted peaks are a triplet around 800 cm^{-1}. Those were C-Cl stretching frequencies as seen from the atom projected VDOS. It is found that the shift is strongly dependent on the percentage of different isotopes present in the solid CCl_2Br_2.

References

[1] M. Zuriaga et al "New Microscopic Mechanism for Secondary Relaxation in Glasses". Phys. Rev. Lett., 103 075701 (2009).
[2] O. A. Pla, D. M. García, J. F. Gebbia, S. Mukhopadhyay, F. Fernandez-Alonso and J. L. Tamarit, (under preparations)

3.21   Inelastic Neutron Scattering Spectroscopy and Ab-initio Calculations for CCl3Br

Daniel Moreno García[1], Oriol Abril Pla[1], Sanghamitra Mukhopadhyay[2,3], Felix Fernandez-Alonso[2,4] and Josep Lluís Tamarit[1]

[1] *Grup de Caracterització de Materials, Departament de Física i Enginyeria Nuclear, Universitat Politècnica de Catalunya*
[2] *ISIS Facility, Rutherford Appleton Laboratory, Chilton, Didcot, Oxfordshire*
[3] *Department of Materials, Imperial College London, Exhibition Road, London*
[4] *Department of Physics and Astronomy, University College London, London*

Molecular crystals are known for their rich polymorphism due to rotational and intramolecular degrees of freedom [1]. Among them, tetrahalomethanes have been the focus of many studies. These molecular compounds exhibit a series of thermally induced solid-solid phase transitions before melting that are attributed to the ability to gain rotational degrees of freedom in the crystalline state [2]. An atomistic knowledge of this material helps to understand its structure and temperature dependent relaxation mechanisms.

Inelastic neutron scattering (INS) experiments were performed on solid CCl_3Br at 10K on the TOSCA spectrometer at ISIS. First principles simulations are performed to interpret the INS data. The plane-wave basis set and norm-conserving pseudopotentials are used as implemented in CASTEP to do these calculations. Various functionals including local density approximations (LDA), generalised gradient approximations (GGA) within PBE, and dispersion corrected functionals were used for optimising crystal structures and calculations of phonons at Γ point. In calculations of vibrationals frequencies linear-response theory was used as implemented in CASTEP code.
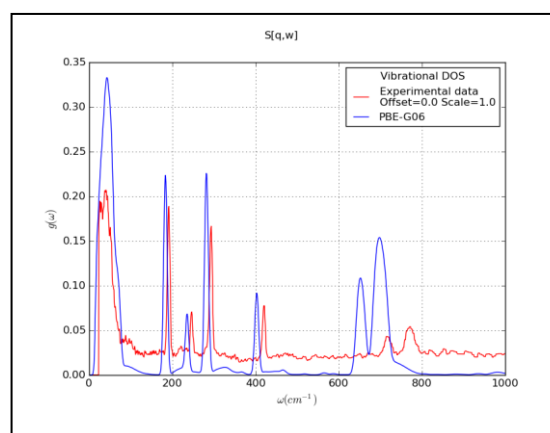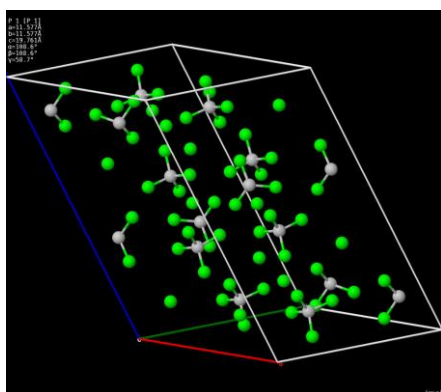
A comparison of these computational results for CCl_3Br crystal with INS experiments is shown in the figure. Results show that simulated peaks are redshifted with respect of the experimental ones around frequency 800 cm^{-1}. Those were C-Cl stretching frequencies. The shift is independent of methodology of dispersion corrections, however, calculations using the LDA functionals seems agree well with experiments.

Thermodynamics calculations on the solid CCl_3Br crystal comprise on different isotopes of Br and Cl show that a combination of ^{37}Cl and ^{79}Br can produce the trend of experimental temperature dependence of specific heat. On the basis of these calculations it has been interpreted that the anomalous increase of specific heat at low temperature is due to the presence of different isotopes in the solid state form of CCl_3Br.

References

[1] Benjamin Parat et al "Polymorphism of CBrCl3".Chemestry of Materials, 17 3359 (2005).
[2] Armin Bunde, et al. "Vibrational models for the Boson peak", J. Non-Cryst. Solids 307 - 310 96 (2002).

3.22 Anharmonic vibrations of hydrogen on Pt(111) catalytic surfaces

Sanghamitra Mukhopadhyay[1,2], and S. F. Parker[1]

[1] *ISIS Facility, Rutherford Appleton Laboratory, Chilton, Didcot, Oxfordshire*
[2] *Department of Materials, Imperial College London, Exhibition Road, London*

The use of Pt as heterogeneous catalyst of hydrogenation reactions is well known [1,2]. Apart from this technological importance, hydrogen on metal surfaces provides a unique opportunity to observe the crossover from classical to quantum dynamics at relatively elevated temperatures [3]. For this reason hydrogen on metal surfaces, and in particular on Pt(111), has received considerable experimental and theoretical interest.

We have performed first principles DFT simulations of Pt(111) surface on two different unit cells having 7 layers and 9 layers of Pt, respectively. One monolayer of H –coverage without any surface reconstructions is considered. A vacuum gap of 15 A is maintained to eliminate the interactions of different slabs in this periodic DFT calculations. Lattice dynamics calculations are done on geometry optimised surfaces within generalised gradient approximations (GGA) using CASTEP. The calculated vibrational spectrum, however, doesn't explain the experimental INS spectrum done at ISIS. There are about 150 cm^{-1} blue shifts in all peaks related with vibrations of H. Further, only one peak is obtained in simulations, rather than three observed in INS experiments. To understand whether this shift is due to anharmonicity in the interatomic potential of vibration of hydrogen, we performed first principles molecular dynamics (MD) simulations as implemented in CASTEP.

Molecular dynamics simulations within first principles DFT are performed on the geometry optimised unit cell using NVT ensemble. The temperature of the simulations cell is kept at 87K, which is the experimental temperature of the INS spectroscopy. The Langevin thermostat, which generates stochastic dynamics via a Brownian motion model, has been used. The central three layers of the slab are kept fixed using constrains for convenience of MD simulations. The vibrational densities of states are calculated by Fourier transforming the velocity autocorrelation on a trajectory of 15ps.
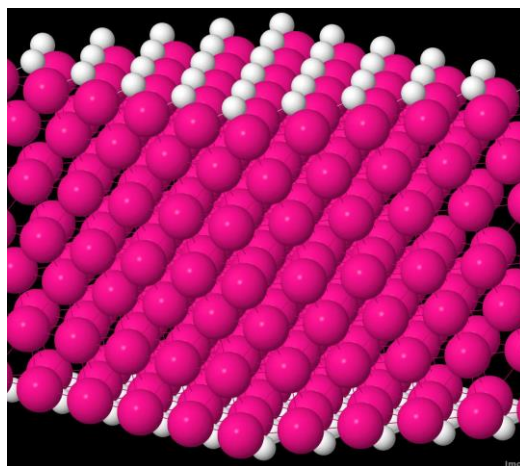
Figure 3.22.1: H on Pt(111) surface. The image of the 7 layers simulations box

References:

[1] A. P. Graham, A. Menzel, and J. P. Toennies, J. Chem. Phys.111, 1676 (1999).

[2] S. C. Bˇadescu, S. C. Ying, and T. Ala-Nissilä, Phys. Rev. Lett. 86, 5092 (2001).

[3] S. Mukhopadhyay and S. F. Parker, *(under preparation).*

3.23   Interactions of skin lipids with glycerol

Judith Anyiam and Anna Akinshina

Biomedical Research Centre, School of Environment & Life Sciences, University of Salford, Salford, Manchester

Glycerol (glycerin) is a small and not toxic molecule; it is one of the components of skin Natural Moisturising Factors (NMFs), a common component in pharmaceutical and cosmetic formulations and considered to play a role of penetration enhancer [1].

The projects investigates the interactions between glycerol and the model skin membranes in a whole range of glycerol concentration in water (from 0 mol % - only water to 100 mol % - only glycerol). Two types of skin membranes are used: a pure ceramide 2 (CER2) membrane and a mixed CER2:CHOL:FFA membrane in 1:1:1 composition [2].

25% glycerol in water   50% glycerol in water   75% glycerol in water
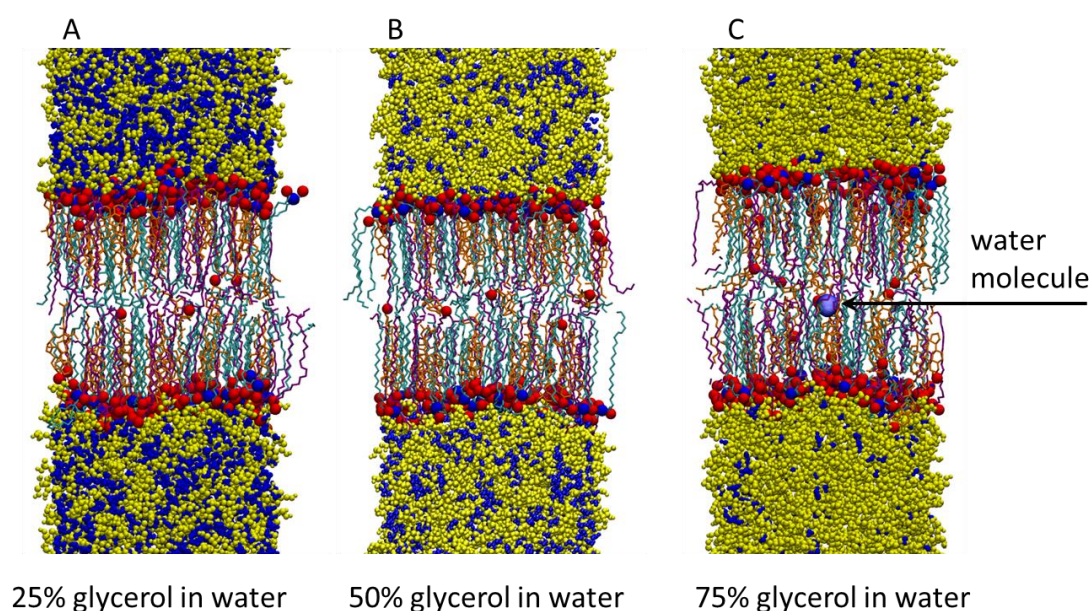
Figure 3.23.1: Representative snapshots of mixed skin lipid bilayer in water–glycerol solution. The concentration of glycerol (A) 25 mol %, (B) 50 mol % and (C) 75 mol %. Lipids colour code: CHOL – orange, CER2 – cyan, FA – purple. Water is shown as blue balls and glycerol – as yellow balls above and below the bilayer. Red and blue balls represent O and N atoms of headgroups. Red balls inside the membrane are oxygen from cholesterol. A water molecule permeated into the membrane at the 75 mol % of glycerol is shown as a large blue ball.

It is well known that glycerol is capable of forming an extensive hydrogen bond network. Our results reveal that due to this H-bond network, the increasing glycerol concentration (> 50 mol %) leads to a strong decrease in the molecular mobility of the system. This affects the mobility of glycerol molecules, water and lipids. At very high glycerol concentrations lipids behave as they are "glued" by glycerol in the headgroup area. This results to a very strong (probably unphysical) increase in the area compressibility modulus, κ_A. However, the H-bonds formed between the lipids remain unaffected by the presence of glycerol. Also, the mobility and the order of lipid tails inside the bilayer (unreachable for glycerol) does not change with increase of glycerol concentration. These

results are in a contradiction with most of the experimental and theoretical studies that suggest fluidisation of the membrane upon addition of glycerol. [3-5]

Additional calculations with different force field (e.g. CHARMM) and free energy calculations for transferring molecules of water and glycerol inside the bilayer from solvent phase are required for better understanding of these result.

These results are the basis of MSc dissertation of Judith Anyiam, ELS, University of Salford.

These results are to be discussed at the CECAM workshop "Insights into skin permeation: from theory to practice" 16-18 October 2017, where I am a member of the organising team.
https://www.cecam.org/workshop-1418.html

The simulations are performed with the help of STFC (SCARF) computational facilities.

References

[1] Björklund, S., Engblom, J., Thuresson, K. and Sparr, E., 2013. *Eur J Pharm Sci*, 50(5), pp.638-645.

[2] Das, C., Noro, M. G., & Olmsted, P. D. 2009. *Biophysical journal*, 97(7), 1941-1951.

[3] Rawlings, A.V. and Matts, P.J., 2005. *Journal of Investigative Dermatology*, 124(6), pp.1099-1110.

[4] Malajczuk, C.J., Hughes, Z.E. and Mancera, R.L., 2013. *Biochimica et Biophysica Acta (BBA)-Biomembranes*, 1828(9), pp.2041-2055.

[5] Björklund, S., Andersson, J.M., Pham, Q.D., Nowacka, A., Topgaard, D. and Sparr, E., 2014. *Soft Matter*, 10(25), pp.4535-4546.

3.24 Interactions of terpenes with aqueous alcohol solutions.

Anna Akinshina[1] and Michael Seaton[2]

[1] *Biomedical Research Centre, School of Environment & Life Sciences, University of Salford, Salford, Manchester*
[2] *STFC, Sci-Tech Daresbury, Keckwick Lane, Daresbury, Warrington, Cheshire,*

This project is focused on terpenes – natural antimicrobial agents. Terpenes are primary components of essential oils produced by some plants, conifer trees and insects. They are natural antimicrobial agents and also known for their ability to promote penetration of drugs through biological membranes (penetration enhancement) [1]. From experimental observations, terpenes are insoluble in water but soluble in alcohol solutions. Understanding the interactions between terpenes and organic solvents at the molecular level is of key importance for future research in drug formulation and drug delivery [2].

Two different computational methods are used in this study: Dissipative Particle Dynamics (DPD) and atomistic molecular dynamics (MD) [3,4]. The DPD model for terpenes will be developed in the framework of this project (in collaboration with Dr Michael Seaton, STFC) and validated by MD simulations.

A set of mono-terpenes under study is: menthol, thymol, carvacrol, limonene and terpineols. These compounds have similar chemical structure but different functional groups and hydrophobicity that affect their activities. Examples of two terpene molecules are shown in Figure 3.24.1.
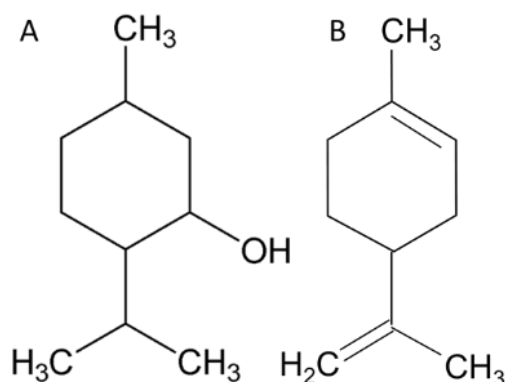
Figure 3.24.1: Chemical structure of two monoterpenes: (A) menthol, (B) limonene

This project is currently on the initial stage. The preliminary results obtained by MD simulations are shown in the Figure 3.24.2. These results were obtained for menthol [4] and clearly show the aggregation of menthol molecules in aqueous solutions and following dissolution upon addition of ethanol. Different concentrations of terpenes and alcohols will be investigated.
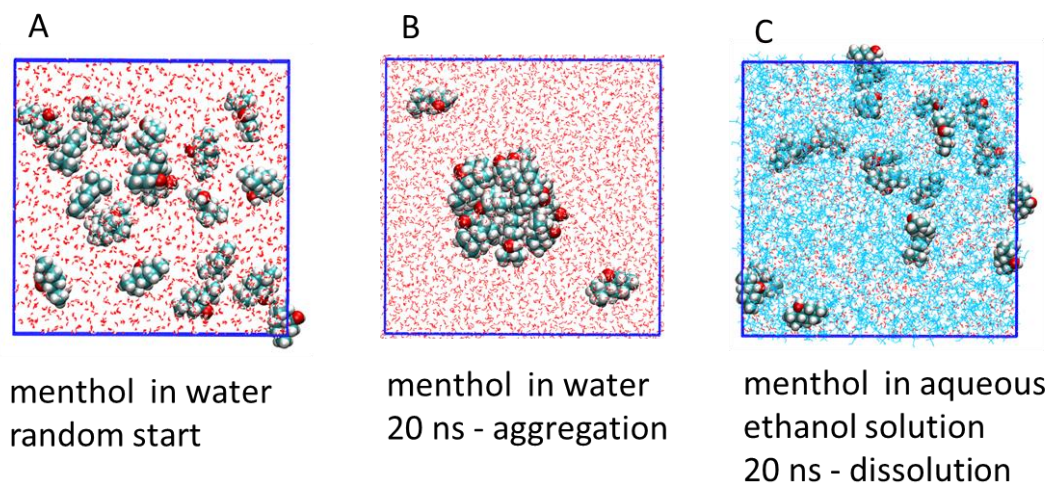
Figure 3.24.2: (A) Starting configuration with randomly placed menthol molecules, (B) Menthol aggregation into a cluster after 20ns and (C) menthol dissolution upon replacing some water with ethanol.

A part of this project serves as research projects for the final year students of the School of Environment & Life Sciences, University of Salford. Also, this collaborative project (with STFC Daresbury Lab) was awarded Salford University Internal Grant Funding (£2,000) in July 2017.

The simulations are performed with the help of STFC (SCARF) computational facilities.

References

[1] Kopeć, W., Telenius, J., & Khandelia, H. 2013. *FEBS Journal*, 280(12), 2785-2805.
[2] Kang, L., Kumar, V.H., Lim, P.F.C., Cheong, H.H. and Chan, S.Y., 2013. Terpenes and Improvement of Transdermal Drug Delivery. In *Natural Products* (pp. 3757-3774). Springer Berlin Heidelberg.
[3] Seaton, M. A., Anderson, R. L., Metz, S., & Smith, W. 2013, *Molecular Simulation*, 39(10), 796-821.
[4] Jasik, M. and Szefczyk, B., 2016. *Journal of molecular modeling*, 22(10), p.234.

3.25 Reagents confined in catalyst support pores - structural studies by total neutron scattering

Marta Falkowska[1], Daniel T. Bowron[2], Haresh Manyar[3], Tristan G. A. Youngs[2], Chris Hardacre[1]

[1] *School of Chemical Engineering and Analytical Science, University of Manchester*
[2] *STFC ISIS Facility, Rutherford Appleton Laboratory, Harwell Campus, Oxford*
[3] *School of Chemistry and Chemical Engineering Queen's University Belfast*

Confined liquids are subject of research in many areas such as geology, biology, food and drug preservation, and heterogeneous catalysis. Due to reduced dimensionality and large surface interface effects, liquids that are subjected to some geometric constraints, usually on nanoscale, can have different properties than in standard bulk conditions. Understanding the structure of confined liquids can explain why these properties change. Comprehending the local environment of liquids in catalyst pores will also reveal information necessary to understand the behaviour of the reacting system during the heterogeneous process. Heterogeneous catalysts are almost four times more frequently used than homogeneous systems, but the design of industrial catalytic processes involving these systems is largely empirical. Understanding the effects of confinement on the reagents structure could lead to significant improvements of these processes.

Molecular-scale structure of three complex disordered systems comprising liquid reagents, *i.e.* benzene-d_6, cyclohexene-d_{10} and cyclohexane-d_{12}, confined in a porous catalyst has been studied by total neutron scattering. MCM-41 was used as the catalyst support. The neutron experiments were undertaken on the Near and InterMediate Range Order Diffractometer (NIMROD) on the ISIS Second Target Station at the Rutherford Appleton Laboratory. Analysis of total neutron scattering data of disordered systems requires constructing three dimensional atomistic models of the studied systems constrained by the experimental data, and herein was done using Empirical Potential Structure Refinement (EPSR; available on SCARF). The complexity of the systems under investigation required establishing the correct model for catalyst support (MCM-41) by varying density, system composition, pore diameter and unit cell size. This was followed by obtaining the correct model of pores filled with the given compound, in which different numbers of molecules had to be inserted into the prepared MCM-41 matrix. Determination of the correct parameters for the models required setting up and running a whole range of EPSR simulations, so a lot of computing power was necessary and the use of the STFC cluster SCARF was crucial. The obtained models were used to calculate structural information expressed by radial, site-site and angular radial distribution functions as well as spatial density functions for confined liquids. These were compared with the corresponding bulk phases. Additionally, cylindrical distribution functions showing the arrangement of atoms and molecules across a pore and orientational cylindrical distribution functions showing the preferred orientations of molecules with respect to the pore walls were calculated.

For the first time, to our knowledge, three liquid reagents in confinement have been fully examined by total neutron scattering. The obtained structural properties show that the structure of liquid in confinement is significantly different than in corresponding bulk phase. Developing the procedure for analysing confined liquids in catalyst support pores enables subsequent modelling of reacting systems structure in snapshots.
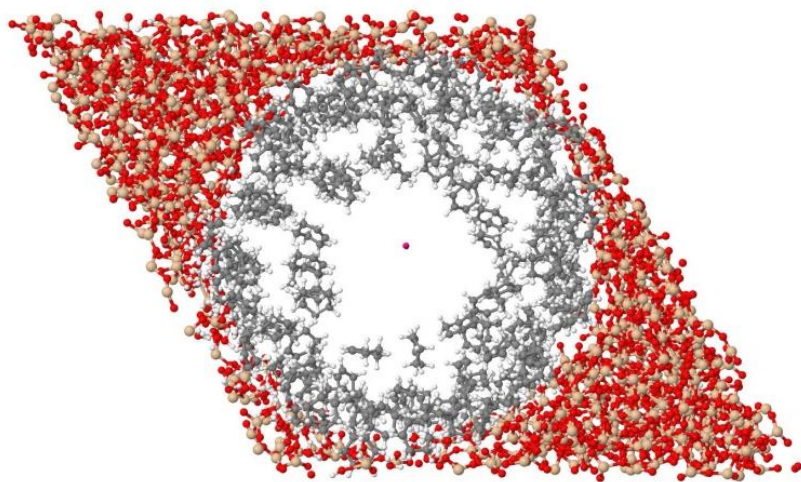
Figure 3.25.1: EPSR model of cyclohexane-d12 confined in MCM-41

3.26   Ion Thruster Simulations using VSIM on SCARF

Scott Lawrie and Dan Faircloth

STFC ISIS Facility, Rutherford Appleton Laboratory, Harwell Campus, Oxford

The VSIM particle in cell (PIC) code from Tech-X Corp. was purchased recently, with the aim to run high power plasma simulations on the SCARF cluster. This makes the first real foray into the use of SCARF for the ISIS low energy beams (LEB) Group. As such, it was sometimes a problematic experience learning how to interface with SCARF, optimise the software license, submit VSIM jobs and post-process the results using VisIt. Enormous thanks go to the SCARF admins for their brilliant work liaising with Tech-X and the LEB Group to achieve a smooth workflow.

Since June 2017, the LEB Group have been using VSIM on SCARF to simulate two different ion thrusters for long-term space applications, using funding from the UK Space Agency's third national space technology programme (NSTP-3) grant. The University of Southampton are developing an integrated microwave propulsion architecture for telecommunication satellites (IMPULSE), which will use a novel xenon microwave electro-thermal thruster (XMET) for the satellites' reaction control system (RCS). The LEB Group have been using VSIM to determine the resonant cavity modes and their sensitivity on geometry changes caused by thermal expansion. Thereafter, plasma was introduced into the cavity and the electrons accelerated by the microwave field. Electron impact ionisation led to an increase in the number density of xenon ions and secondary electrons, such that the plasma distribution could be determined. The large number of processing cores available on SCARF has allowed many simulations to be run in parallel, or one large simulation to be run much quicker than on a desktop PC.

Surrey Satellite Technologies Ltd (SSTL) and Added Value Solutions (AVS) are leading another NSTP-3 project to deliver an ion thruster which uses water propellant: the AQUAJET. Although not delivering as high performance as traditional xenon thrusters, the AQUAJET has the advantage of refuelability throughout the solar system from abundant water sources such as comets, the Moon or Mars; whereas xenon can only be produced on Earth. The LEB Group have been using the power of SCARF to run high resolution VSIM simulations of the AQUAJET to estimate its thrust efficiency.
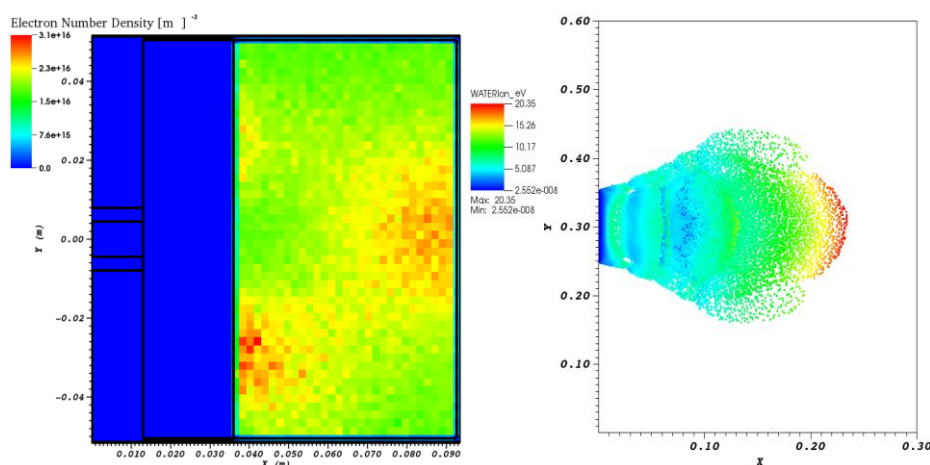
Figure 3.26.1: Electron density in the XMET plasma increasing due to microwave acceleration (left). Water ion plume escaping the AQUAJET and undergoing ambipolar acceleration (right).

3.27 Optimisation of Electron Storage Ring Performance using a Multi-Objective Genetic Algorithm

I.P.S. Martin

Diamond Light Source, Oxfordshire, UK

The Diamond Light Source provides photon beams of exceptional quality to a broad range of scientific users for experiments ranging from studies of condensed matter physics to investigating new medicines and treatments to innovative engineering and cutting-edge technology. As part of this operation, for several days each year the storage ring is configured to reduce the electron bunch length for the generation of short x-ray pulses and coherent THz radiation. This mode of operation requires a re-tuning of all the quadrupole and sextupole magnets to produce the desired effect, and results in a much lower lifetime and injection efficiency than the standard mode of operation.

During 2018 the Diamond storage ring is due to be upgraded by replacing one of the sextupole magnets with a short multipole wiggler, thereby adding a new beamline to the facility for in-situ imaging and diffraction experiments (the so-called DIAD beamline, [1, 2]). The removal of this sextupole is anticipated to have a strong impact on the performance of the storage ring in short pulse / THz mode, requiring a careful re-tuning of the magnet strengths in order to mitigate this effect.

In previous years the SCARF cluster has been used extensively to perform particle tracking simulations in order to optimise the performance of Diamond in a variety of operating modes (see [3] for more details). This optimisation is typically carried out with the aid of multi-objective evolutionary algorithms such as the Non-Dominated Sorting Genetic Algorithm (NSGA-II, [4]). The usual method is to allow the optimisation algorithm to vary the magnet set-points in the model, then to track large numbers of particles over thousands of turns in order to estimate the likely injection efficiency and lifetime for each specific configuration. Based on these results, the optimisation algorithm uses a process of selection, mutation and cross-over to allow a population of potential solutions to evolve over time, gradually improving the performance of the whole. At the end of each optimisation run, a so-called Pareto-optimal front is generated, illustrating the trade-off between two or more competing objectives (in this case the lifetime and injection efficiency).

One of the specific questions analysed by the present study was to investigate the potential improvement in performance that could be gained by replacing the power supply of the sextupole local to the one removed to increase the strength from the present limit of 64 m^{-3} up to 81 m^{-3}. The results presented in Fig. 3.26.1 show a clear benefit for raising this limit, and indeed a value of 110 m^{-3} would allow the injection efficiency to be increased further still. However, to do so would require the magnet itself to be replaced alongside the power supply. A further study was conducted into the potential benefits of splitting the sextupoles from the existing 12 families into 20 (blue Pareto-front in Fig. 3.27.1), again showing a clear increase in performance.

Trials of the new operating mode identified by this study are due to begin in early 2018, with the new beamline to be installed in Summer 2018. The ability to exploit the computing power of clusters such as SCARF has had a transformative effect in the way storage rings are studied and optimised, opening up new and demanding operating modes for the benefit of the broader scientific community.
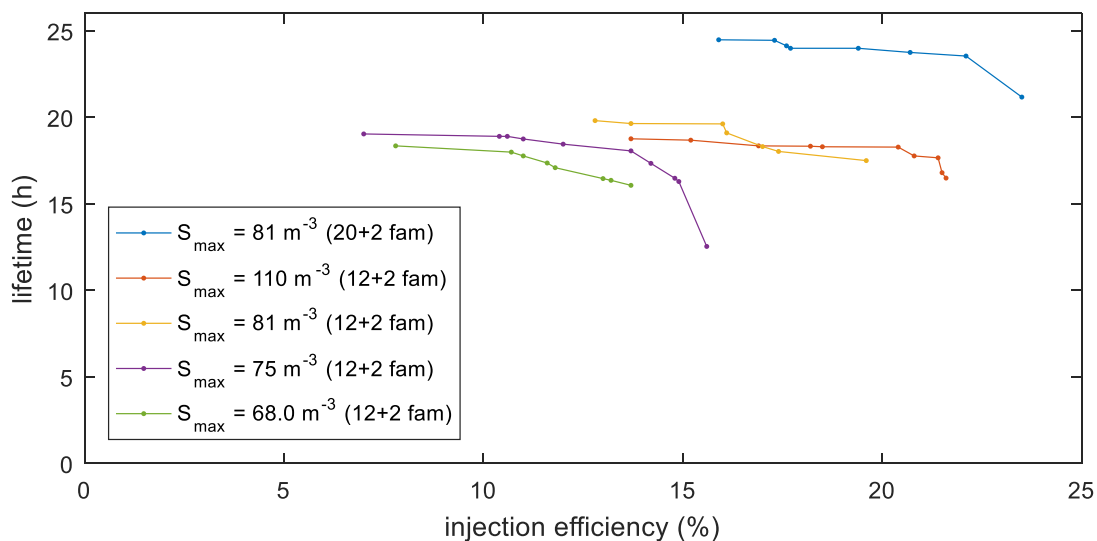
Figure 3.27.1: Pareto fronts for NSGA-II optimisations of the Diamond storage ring with a variety of constraints. The results show a clear increase in predicted injection efficiency with higher sextupole strengths. The lifetime is expected to increase further still if the sextupoles are split into 20 families rather than the standard 12.

References

[1] http://www.diamond.ac.uk/Beamlines/Engineering-and-Environment/DIAD.html

[2] B. Singh et al., Proc. Intl. Particle Accelerator Conference 2016, Busan, Korea, THPMR050, p. 3518, (2016)

[3] I.P.S. Martin et al., SCARF Annual Report, RAL-TR-2017-001, (2016)

[4] K. Deb, A. Pratap, S. Agarwal, T. Meyarivan, IEEE Trans. On Evolutionary Computation 6, 2, pp 182-197, (2002)

3.28 Quantitative Characterisation of High-resolution Broadband Neutron Molecular Spectrometers

M. Zanetti[1, 2], R.S. Pinna[1, 2], S. Rudić[1], D. Colognesi[3], G. Škoro[1], S.F. Parker[1], G. Gorini[2] and F. Fernandez-Alonso[1,4]

[1] *ISIS Neutron and Muon Source, Rutherford Appleton Laboratory, Chilton, Didcot, UK*
[2] *Università degli Studi di Milano-Bicocca, Milan, Italy*
[3] *Consiglio Nazionale delle Ricerche, Istituto di Fisica Applicata "Nello Carrara", Sesto Fiorentino, Italy*
[4] *University College London, London, UK*

It is an exciting time for neutron molecular spectrometers: the TOSCA primary upgrade has been successfully completed at ISIS, the redesign of the secondary is underway, and the joint Italy-UK VESPA project for the European Spallation Source (Lund, Sweden) is gaining momentum.

TOSCA and VESPA are high-resolution, indirect-geometry inelastic neutron spectrometers that can operate up to energy transfers of ca. 500 meV in neutron-energy loss. TOSCA has been operational at ISIS since the beginning of the century, while the latter is being designed for the ESS by the Italian Research Council and ISIS. The original conceptual design and subsequent scientific specification of this kind of spectrometers were settled decades ago, and were solely performed on the basis of analytical calculations, a task that necessarily relied on a number of hard-to-test assumptions at the time. Using modern neutron-transport codes offers the exciting prospect of assessing in quantitative and unprecedented detail the performance of this type of instrument, as well as provides a powerful tool for instrument design and further optimisation. We, therefore, anticipate that the lessons that we are learning from joint computational modelling and experimental campaigns will have important implications for the optimal neutronic design of similar instrumentation in the foreseeable future.

In the past, our work was primarily devoted to TOSCA [1] upgrade paths, in particular the neutron-guide design, as well as the benchmarking of the moderator model and the development of the secondary-spectrometer design by means of the McStas ray-tracing software [2] – see previous SCARF reports for additional details. Some of the latest calculations have been focused on the design of a new doubly curved analyser, which would replace the flat analyser currently installed in the TOSCA inelastic-scattering modules. This innovative analyser will be able to focus the scattered neutrons in both horizontal and vertical directions, in order to increase the solid-angle coverage after the sample and, thus, improve the collection efficiency of the instrument in a significant manner. Additionally, comparison of experimental data from the upgraded beamline with simulation has provided further insights into the reliability of our simulation tools and on second-order effects such as the neutron profile at the moderator surface or the orientation of the guide.

To reach the current stage in the design of VESPA, several simulations have been run in order to determine the optimal beamline orientation at ESS, and to design the 50-m neutron guide and the secondary spectrometer, thus completing a sound baseline as a robust basis for a subsequent detailed design of the spectrometer. During this process, several configurations have been explored in order to identify the best way of accommodating engineering constraints. VESPA will have the

unprecedented ability of trading flux for resolution thanks to its pulse-shaping choppers, and this new capability has been put to the test with these simulations.

The modelling of the secondary instrument on TOSCA and VESPA has also included the development and study of the spectroscopic response of virtual samples (Fig 3.28.1-a) and the evaluation of the instrumental resolution (Fig 3.28.1-b). The trade-off between increased sensitivity and resolution has been thoroughly investigated, in particular with reference to the selection of the mosaicity for the crystal analyser.

We have also performed experiments on the TOSCA spectrometer in order to calibrate the simulation results, so as to validate the computational models used [3], with a view to attaining a satisfactory and quantitative description of experimental data (Fig. 3.28.1).

(a)   (b)
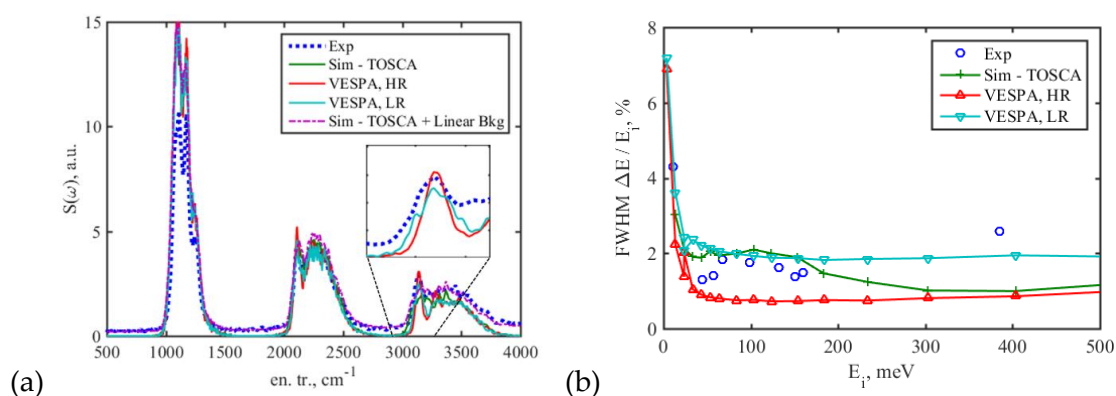
Figure 3.28.1: (a) Simulated TOSCA and VESPA spectra of ZrH2 compared with recent TOSCA data (the inset shows the two resolution modes on VESPA); (b) Simulation of the instrumental resolution of TOSCA and VESPA with a virtual "delta sample," and comparison with experimental data (2.5- diiodothiophene standard).

The simulations performed on the SCARF cluster required very high statistics in order to generate high-quality results. Depending on the case, we used up to 1,200 cores for up to fifteen-hour runs. SCARF was essential to these simulations because the physical processes involved are manifold and difficult to disentangle without recourse to detailed simulations, *i.e.*, neutron moderation, reflection in the neutron guides, scattering processes and Bragg diffraction onto the analyser.

These activities to attain a sound description of the instruments using simulation and parallel experimental campaigns continue apace. The next stages involve the development of beryllium-filter models for TOSCA and VESPA, followed by a systematic evaluation of background sources.

References

[1] S. F. Parker, F. Fernandez-Alonso, A. J. Ramirez-Cuesta, J. Tomkinson, S. Rudić, R. Pinna, G. Gorini, and J. Castañon, 2014. Recent and future developments on TOSCA at ISIS. *Journal of Physics: Conference Series* 554, 012003.

[2] P. Willendrup, E. Farhi, K. Lefmann, 2004. McStas 1.7 - a new version of the flexible Monte Carlo neutron scattering package, *Physica B* 350 e735-e737.

[3] R. S. Pinna, S. Rudić, M. J. Capstick, D. J. McPhail, D. E. Pooley, G. D. Howells, G. Gorini, F. Fernandez-Alonso, 2017. Detailed characterisation of the incident neutron beam on the TOSCA spectrometer. *Nuclear Instruments and Methods A*, 870, 79-83.

4. APPENDIX: SCARF HARDWARE DETAILS

Host group	CPU type and frequency	Nodes	Cores /node	Total cores	Interconnect	Total memory
SCARF17/ DeRevolutionIbus	Intel E5-2650v4 @ 2.2GHz	201	24	4824	EDR Infiniband	25728 GB
SCARF16/ MagnaCarta/ IBIS	Intel E5-2650v3 @ 2.30GHz	56	20	1120	FDR Infiniband	7168 GB
SCARF15	Intel E5-2650v3 @ 2.30GHz	68	20	1360	FDR Infiniband	8704 GB
SCARF14	Intel E5-2650v2 @ 2.60GHz	56	16	896	QDR Infiniband	7168 GB
SCARF13	Intel E5-2660 @ 2.20GHz	84	16	1344	QDR Infiniband	5376 GB
SCARF12	Intel X5675 @ 3.06GHz	20	12	240	QDR Infiniband	960 GB
SCARF11	Intel X5660 @ 2.8GHz	32	12	384	QDR Infiniband	768 GB
Lexicon-2/ SCARF10	Intel E5530 @ 2.40GHz	104	8	832	DDR Infiniband	2496 GB
Grand Totals		623		11000		58188 GB

5. APPENDIX: INDEX OF FIGURES

6. APPENDIX: PUBLICATIONS AND PRESENTATIONS

6.1 Publications

	Title	Authors	Journal
1	*Association of aescin with β- and γ-cyclodextrins studied by DFT calculations and spectroscopic methods*	A. I. Ramos, P. D. Vaz, S. S. Braga, A. M. S. Silva	Beilstein J. Nanotechnol., 8 (2017), 348–357; DOI:10.3762/bjnano.8.37
2	*Inelastic neutron scattering study of reline: shedding light on the hydrogen bonding network of deep eutectic solvents*	A. C. F. Araújo, J. A. P. Coutinho, M. M. Nolasco, S. F. Parker, P. J. A. Ribeiro-Claro, S. Rudić, B. I. G. Soares, P. D. Vaz	Phys. Chem. Chem. Phys., 19 (2017), 17998–18009. DOI: 10.1039/c7cp01286a
3	*Vibrational profile of next generation biodegradable polymers: polyethylene furanoate*	C. Araújo, M. Nolasco, P. Ribeiro-Claro, P. Vaz, S. Rudić, A. Silvestre, A. F. Sousa	manuscript in preparation
4	*Inelastic neutron scattering spectra of cellulose forms*	C. Araújo, M. Nolasco, P. Ribeiro-Claro, P. Vaz, S. Rudić, A. Silvestre, C. Freire	manuscript in preparation
5	*Solventless oxidation of olefins by Mo@surface of carbon waste material*	C. Petit, M. Velez, A. S. Mestre, P. D. Vaz, A. P. Carvalho, C. D. Nunes	manuscript in preparation
6	*Active-Site Protein Dynamics and Solvent Accessibility in native Achromobacter cycloclastes Copper Nitrite Reductase*	K. Sen, S. Horrell, D. Kekilli, C.W. Yong, T.W. Keal, H. Atakisi, D.W. Moreau, R.E. Thorne, M.A. Hough and R.W. Strange	IUCrJ 2017, 4, 495
7	*Unravelling exceptional acetylene and carbon dioxide adsorption within a tetra-amide functionalized metal-organic framework*	F. Moreau, I. da Silva, N.H. Al Smail, M. Savage, H.G.W. Godfrey, S.F. Parker, P. Manuel, S. Yang and M. Schröder	Nature Communications 8 (2017) 14085 [doi: 10.1038/ncomms14085]
8	*Vibrational spectra of buta-1,3-diene iron tricarbonyl: comparison to surface species*	S.F. Parker, C. Carias and J. Tomkinson	Catalysis, Structure & Reactivity 3 (2017) 119-127. [doi: 10.1080/2055074X.2017.1278870]
9	*Structure and vibrational spectra of 2,5-diiodothiophene: a model for polythiophene*	S.F. Parker, J.L. Parker and M. Jura	Journal of Physical Chemistry C 121 (2017) 12636-12642. [doi: 10.1021/acs.jpcc.7b03803].

10	*Topological triplon modes and bound states in a Shastry-Sutherland magnet*	P. A. McClarty, F. Krüger, T. Guidi, S. F. Parker, K. Refson, A.W. Parker, D. Prabakharan and R. Coldea	Nature Physics (2017) [doi:10.1038/nphys4117]
11	*Selective production of arenes via direct lignin upgrading over a niobium-based catalyst*	Y. Shao, Q. Xia, L. Dong, X. Liu, X. Han, S.F. Parker, Y. Cheng, L.L. Daemen, A.J. Ramirez-Cuesta, S. Yang and Y. Wang	Nature Communications 8 (2017) 16104. [doi: 10.1038/ncomms16104]
12	*Vibrational spectroscopy with neutrons: recent developments*	S.F. Parker, A.J. Ramirez-Cuesta and L. Daemen	Spectrochimica Acta A: Molecular and Biomolecular Spectroscopy (2017). [doi: 10.1016/j.saa.2017.09.057]
13	*Catalysis*	P.W. Albers. D. Lennon and S.F. Parker	"Neutron Scattering – Applications in Biology, Chemistry, and Materials Science", F. Fernandez-Alonso and D.L. Price (eds.), Academic Press, 2017, Vol 49, Ch. 5, 279-348.
14	*Detecting Molecular Rotational Dynamics Complementing the Low-Frequency Terahertz Vibrations in a Zirconium-Based Metal-Organic Framework*	M. Ryder, B. Van de Voorde, B. Civalleri, T.D. Bennett, S. Mukhopadhyay, G. Cinque, F. Fernandez-Alonso, D. De Vos, S. Rudić, J. Tan	Phys. Rev. Lett., 118, 255502 (2017). DOI:10.1103/PhysRevLett.118.255502
15	*Tracking thermal-induced amorphization of a zeolitic imidazolate framework via synchrotron in situ far-infrared spectroscopy*	M.R. Ryder, *et al.*,	Chem. Commun., 53, 7041 (2017).
16	*Large elastic recovery of zinc dicyanoaurate*	C.S. Coates, M.R. Ryder, *et al.*,	APL Mater., 5, 066107 (2017).
17	*Arrest of Landau damping in the 1+1D Vlasov–Poisson system*	J. T. Parker and P. J. Dellar	manuscript in preparation
18	*Quasielastic neutron scattering measurements and ab initio MD-simulations on single ion motions in molten NaF*	F. Demmel and S. Mukhopadhyay	J. Chem. Phys., 144, 14503. (2016) DOI: 10.1063/1.4939072

19	*Heads or tails: how do chemically substituted fullerenes melt?*	F. Bresme and F. Fernandez-Alonso	Phys. Chem. Chem. Phys., 18, 17202 (2016). DOI: 10.1039/c6cp01333c
20	*Detailed characterisation of the incident neutron beam on the TOSCA spectrometer. In Nuclear Instruments and Methods in Physics Research Section A: Accelerators, Spectrometers, Detectors and Associated Equipment*	R. S. Pinna, S. Rudić, M. J. Capstick, D. J. McPhail, D. E. Pooley, G. D. Howells, G. Gorini, F. Fernandez-Alonso	*Nuclear Instruments and Methods in Physics Research Section A: Accelerators, Spectrometers, Detectors and Associated Equipment*, Volume 870, 2017, Pages 79-83, ISSN 0168-9002. Url: doi.org/10.1016/j.nima.2017.07.018.
21	*The TOSCA Spectrometer at ISIS: Guide Upgrade and Beyond*	R.S. Pinna, M. Zanetti, S. Rudić, S.F. Parker, J. Armstrong, S.P. Waller, D. Zacek, C. Smith, S.M. Harrison, G. Gorini, F. Fernandez-Alonso	Proceedings of the *22nd International Collaboration on Advanced Neutron Sources ICANS XXII* (accepted for publication in the *Journal of Physics: Conference Series*).
22	*Chemical Dynamics and Spectroscopy at the ISIS Pulsed Neutron and Muon Source*	F. Fernandez-Alonso	S. Abbas, M.N. Rao, and S. Basu Eds., Proceedings of the *6th Conference on Neutron Scattering CNS2016*, Bhabha Atomic Research Centre, Mumbai, India, 2016, p. 16. Url: inis.iaea.org/search/search.aspx?orig_q=RN:48017235
23	*The neutron guide upgrade of the TOSCA spectrometer*	R.S. Pinna, S. Rudić, S. F. Parker, J. Armstrong, M. Zanetti, G. Škoro, S. P. Waller, D. Zacek, C. A. Smith, M. J. Capstick, D. J. McPhail, D. E. Pooley, G. D. Howells, G. Gorini, and F.Fernandez-Alonso	(manuscript in preparation)
24	*TOSCA Secondary Spectrometer Upgrade*	R.S. Pinna, S. Rudić, M. Zanetti, D. Zacek, S.F. Parker, G. Gorini, F. Fernandez-Alonso	(manuscript in preparation)

6.2 Presentations

	Conference	Title	Presenter
1	XXV Encontro Nacional da SPQ, Lisbon, July, 2017	(Poster) *Cellulosic nanostructured materials: an inelastic neutron scattering*	M. Nolasco, C. F. Araújo, P. Ribeiro-Claro, P. D. Vaz, S. Rudić
2	Research Day 2017, University of Aveiro, Aveiro, Portugal, June 2017	(Poster) *Inelastic Neutron Scattering study of Reline: shedding light on the hydrogen bonding network of deep eutectic solvents*	C. Araujo, J. A. P. Coutinho, M. M. Nolasco, S.F. Parker, P. J. A. Ribeiro-Claro, S. Rudić, B. I. G. Soares, P. D. Vaz
3	PATh Spring Workshop 2017 – 2nd edition – Deep Eutectic Solvents (DES), Aveiro, Portugal, June 2017	*Architecture of deep eutectic solvents – lessons learned from vibrational spectroscopy*	C. Araujo, J. A. P. Coutinho, M. M. Nolasco, S.F. Parker, P. J. A. Ribeiro-Claro, S. Rudić, B. I. G. Soares, P. D. Vaz
4	19th IUPAB Congress and 11th EBSA Congress, 2017, Edinburgh, UK	(Poster) *Solvent Accessibility and Ligand Binding in Native Achromobacter cycloclastes Copper Nitrite Reductase*	K. Sen
5	11th Triennial Congress of the World Association of Theoretical and Computational Chemists, 2017, Munich, Germany	(Poster) *Solvent Accessibility and water Binding in Native Copper Nitrite Reductases*	K. Sen, M. A. Hough, R. W. Strange, C. W. Yong, T. W. Keal
6	QM/MM Methods and Applications, 2017, University of Manchester, UK	(Poster) *Solvent Accessibility and water Binding in Native Copper Nitrite Reductases*	
7	QM/MM Methods and Applications, 2017, University of Manchester, UK	*QM/MM modelling of heterogeneous and enzymatic catalysis*	T. W. Keal
8	DEFect NETwork Materials Science and Engineering, Diamond Light Source, 8th February 2017	*Inelastic neutron scattering: applications in microporous materials*	

| 9	9th International Conference on Advanced Vibrational Spectroscopy (ICAVS9), 14/6/17, Victoria, Canada	*Vibrational spectroscopy with neutrons: recent developments*	S.F. Parker
10	Dielectrics 2017, National Physical Laboratory, Teddington, UK – April 2017	*Dynamic Dielectric Characteristics of Zeolitic Metal-Organic Frameworks via Synchrotron Reflectivity Measurements*	M.R. Ryder
11	40th Annual Meeting of the British Zeolite Association, Preston, UK – April 2017	*Terahertz Vibrations and Mechanical Properties of Metal-Organic Frameworks*	M.R. Ryder
12	Royal Society of Chemistry (RSC) Theoretical Chemistry Group Meeting, Southampton, UK – May 2017	*Terahertz Vibrations and Mechanical Properties of Metal-Organic Frameworks*	M.R. Ryder
13	Oak Ridge National Laboratory, Tennessee, USA – August 2017	*Revealing the Secrets Hidden Within the Lattice Dynamics of Next-Generation Materials*	M.R. Ryder
14	Northwestern University, Evanston, USA – September 2017	*Revealing the Secrets Hidden Within the Lattice Dynamics of Next-Generation Materials*	M.R. Ryder
15	EuroMat 2017, Thessaloniki, Greece– September 2017	*Revealing the Link Between Terahertz Vibrations and Mechanical Properties*	M.R. Ryder
16	Muon Site Calculation meeting, 28th November, 2016. Rutherford Appleton Laboratory,	*The magnetic state of MnP under pressure: a new case for DFT with muons*	R. De Renzi
17	Muon Site Calculation meeting, 28th November, 2016. Rutherford Appleton Laboratory	*Ab-initio calculation of the contact hyperfine fields for muon spin rotation spectroscopy*	I. J. Onuorah, P. Bonfà, R. De Renzi
18	14th International Conference on Muon Spin Rotation, Relaxation and Resonance μSR2017, 25th-30th June,	*Ab-inito calculation of the hyperfine field at the muon site in metallic systems*	I. J. Onuorah, Pietro Bonfà, Roberto De Renzi

	2017, Sapporo, Hokkaido Japan		
19	14th International Conference on Muon Spin Rotation, Relaxation and Resonance µSR2017, 25th-30th June, 2017, Sapporo, Hokkaido Japan	*$Yb_2Pd_2In_{1-x}Sn_x$: A study of the p-T-x phase diagram*	G. Lamura, T. Shiroka, I. Onuorah, P. Bonfà, S. Sanna, Z. Shermadini, R. Khasanov, R. De Renzi, I. Curlik, A. Dzubinska, G. Pristas, M. Reiffers, F. Gastaldo, M. Giovannini,C. Ritter, M. Putti ,T. Goko, R. Sheuermann, E. Bauer
20	14th International Conference on Muon Spin Rotation, Relaxation and Resonance µSR2017, 25th-30th June, 2017, Sapporo, Hokkaido Japan	*Determining muon stopping sites and the temperature dependence of the muon's hyperfine parameters using computational methods*	L. Liborio, S. Sturniolo
21	QENS 2016 meeting, Berlin, Germany	*Application of ab-initio Molecular Dynamics in Modelling of QENS data on Functional Materials*	S. Mukhopadhyay
22	Molecular Spectroscopy Science Meeting (MSSM) 2016	*INS Spectroscopy and ab-initio calculations for CCl_3Br*	S. Mukhopadhyay
23	Molecular Spectroscopy Science Meeting (MSSM) 2016	*INS Spectroscopy and ab-initio Calculations for CBr_nCl_{4-n},n=0,1,2*	J. F. Gebbia
24	Faraday Joint Interest Group Conference 2017, 11-13 April 2017, Warwick, UK	*Structure and Vibrations of Hydrogen Bonds in Organic Anti-ferroelectric Squaric Acid*	S. Mukhopadhyay
25	IOP Workshop: Self-Assembly, Recognition, and Applications (SARA 2016), Edinburgh		
26	Showcase: Health, Wellbeing and Society Research at The University of Salford, Salford,	(Poster)	
27	CECAM workshop: Designing Force fields in an Age of Cheap Computing,	(Posters)	

	Sheffield, 26-28 July 2017		
28	ISIS Disordered Materials Group meeting, 14-15 February 2017, Abingdon, UK pores	*Structure of liquids in the MCM-41 pores*	M. Falkowska, D. T. Bowron, C. Hardacre, T. G. A. Youngs
29	3rd UK Catalysis Conference, 4-6 January 2017, Loughborough, UK	*Confined liquids studied by total neutron scattering*	M. Falkowska, D. T. Bowron, H. Manyar, T. G. A. Youngs, C. Hardacre
30	Faraday Joint Interest Group Conference 2017, 11-13 April 2017, Warwick, UK	*Structural studies on aromatic and aliphatic liquids under confinement by total neutron scattering*	M. Falkowska, D. T. Bowron, H. Manyar, T. G. A. Youngs, C. Hardacre
31	*22nd International Collaboration on Advanced Neutron Sources ICANS XXII,* March 27-31 2017, Oxford, United Kingdom	*The TOSCA Spectrometer at ISIS: Guide Upgrade and Beyond*	M. Zanetti
32	ICNS 2017, International Conference on Neutron Scattering 2017, July 9-13 2017, Daejeon, South Korea	*TOSCA Neutron Guide and its Effect on the Instrument*	S. Rudić
33	*6th Conference on Neutron Scattering CNS2016,* 20-24th November 2016, Mumbai, India (invited talk).	*Chemical Dynamics and Spectroscopy at the ISIS Pulsed Neutron and Muon Source*	F. Fernandez-Alonso

7.   APPENDIX: SCARF QUEUE USAGE 2016-17

7.1   General SCARF Queue

The scarf queue is the generally accessible queue, to which all users have access. A second queue, scarf-rhel7, has been added to allow access to the hardware which is installed with a new version of the operating system that runs on SCARF nodes. Over time more hardware will be migrated to the new operating system.
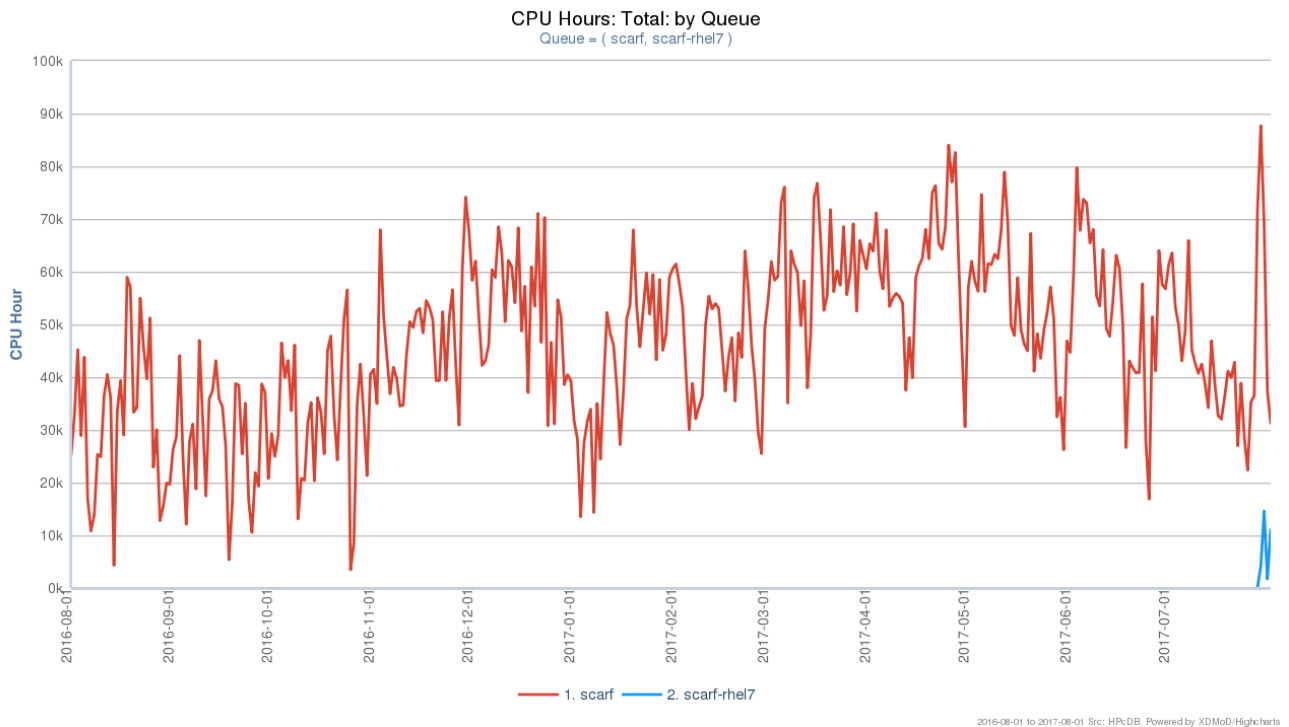
Figure 7.1.1: SCARF Queue Usage

The LSF "SLA" mechanism is used to allow groups of users to get preferential access to portions of hardware they have contributed money to purchase, while still making the hardware available to other users' jobs up to 24 hours in length. This is currently in place for ISIS on SCARF13 and SCARF17 and ISIS and CLF FBI on SCARF14 and SCARF15.

The following graphs show the usage on each combination of user community and hardware. The blue line shows the level that is guaranteed to the user community. The red line shows usage by the community of their guarantee. The yellow line shows the community's usage of the hosts covered by the particular SLA.
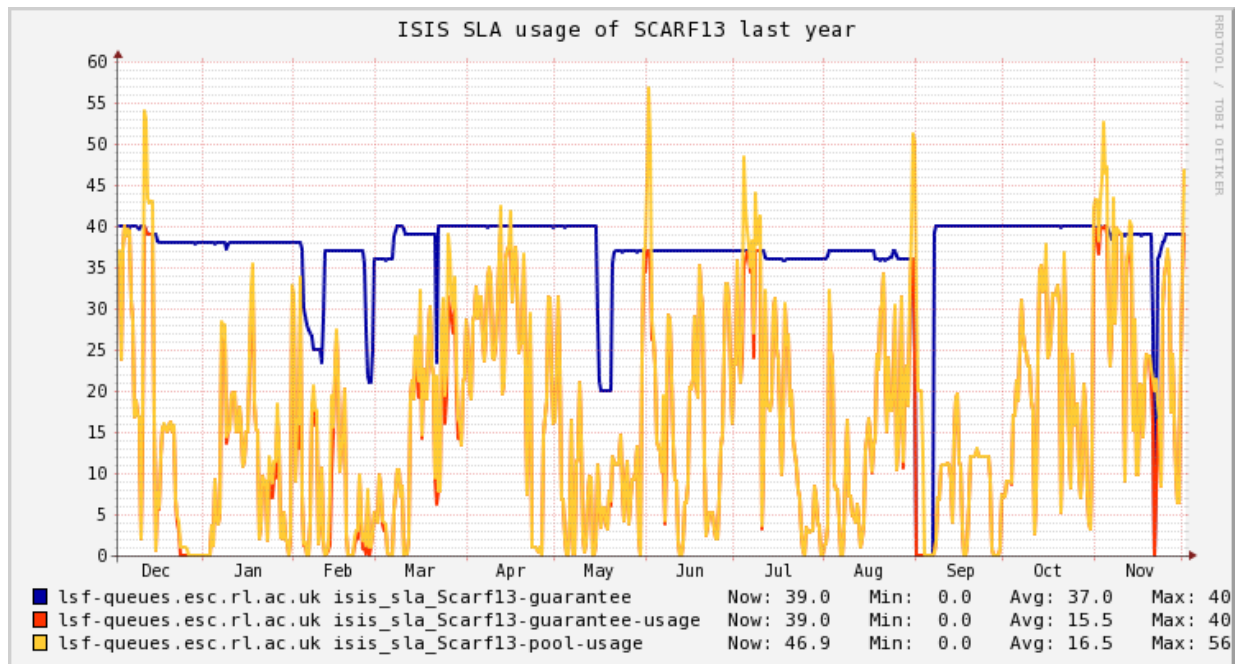
Figure 7.1.2: ISIS SLA Usage of SCARF 13

While the yellow line does exceed the blue line on a number of occasions, for the most part ISIS usage of SCARF13 has been well under that guaranteed to them, averaging at less than half of the guaranteed hosts.
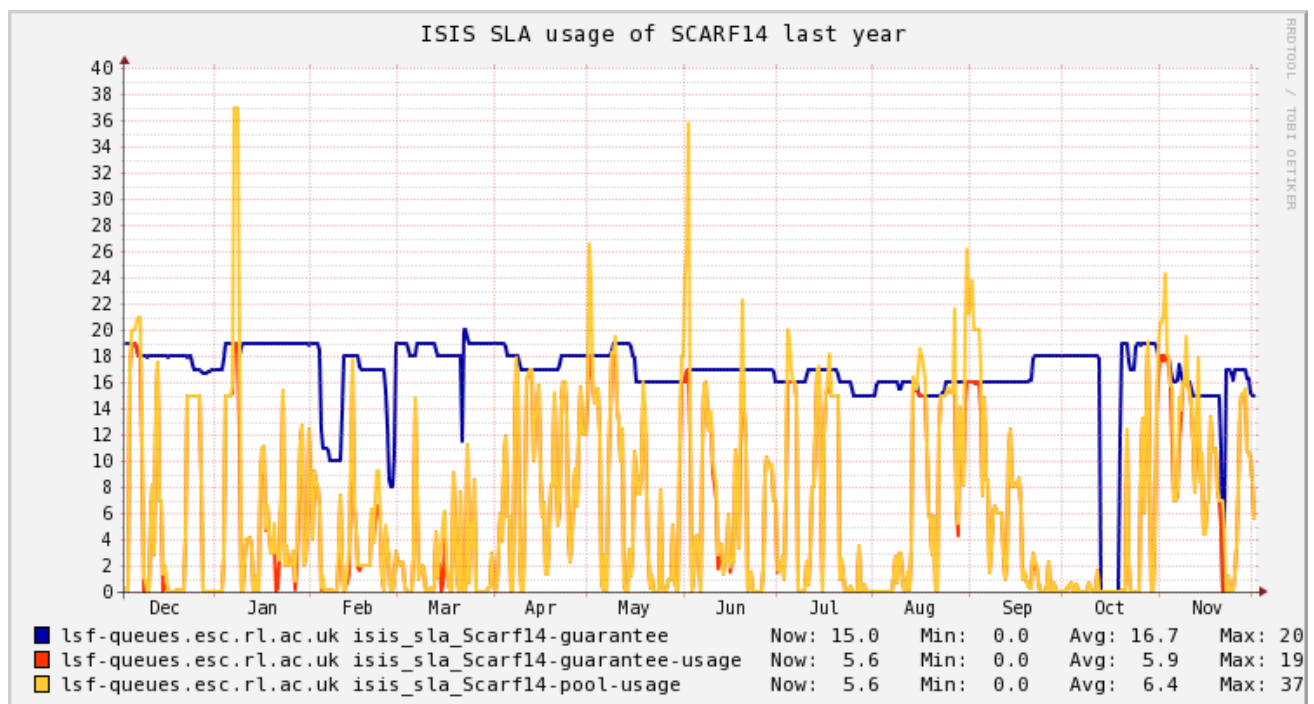

Figure 7.1.3: ISIS SLA Usage of SCARF 14

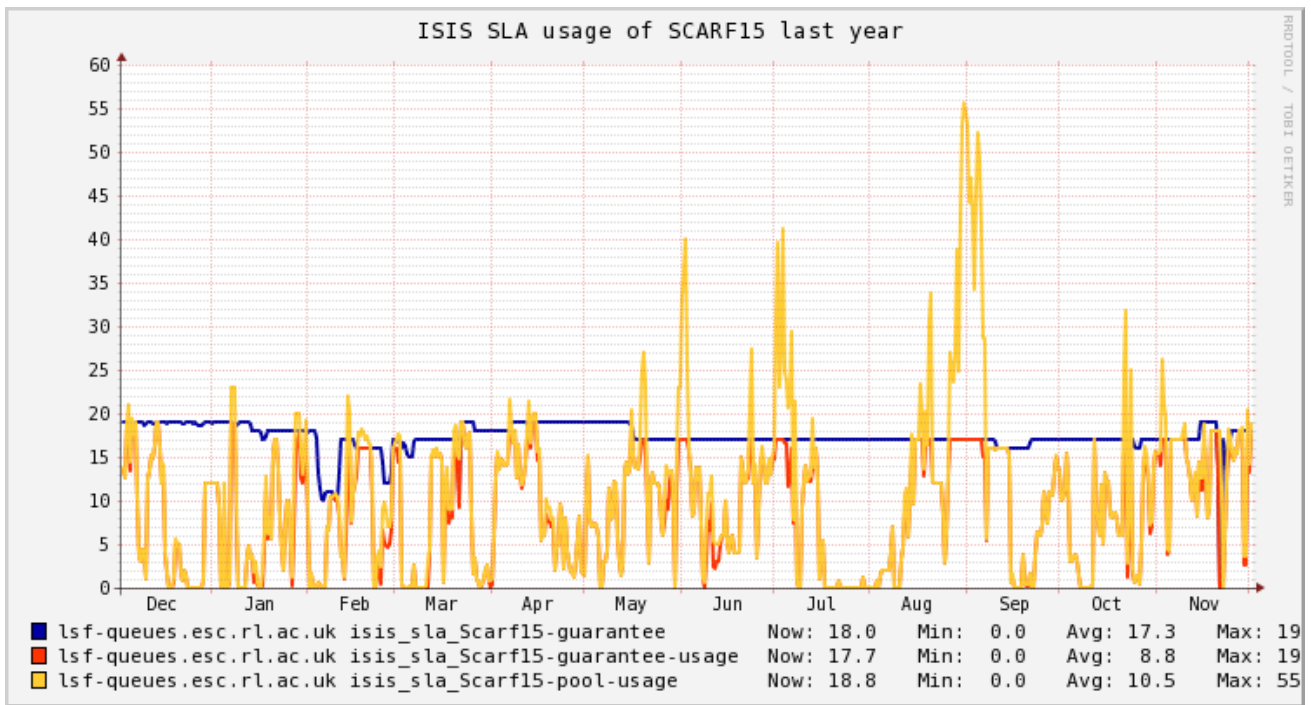The SCARF14 SLA for ISIS shows a similar usage level to that of SCARF13 above.

Figure 7.1.4: ISIS SLA Usage of SCARF 15

While the SCARF15 usage broadly fits the same pattern as SCARF13 and SCARF14, the periods where usage exceeds the guarantee are much larger.
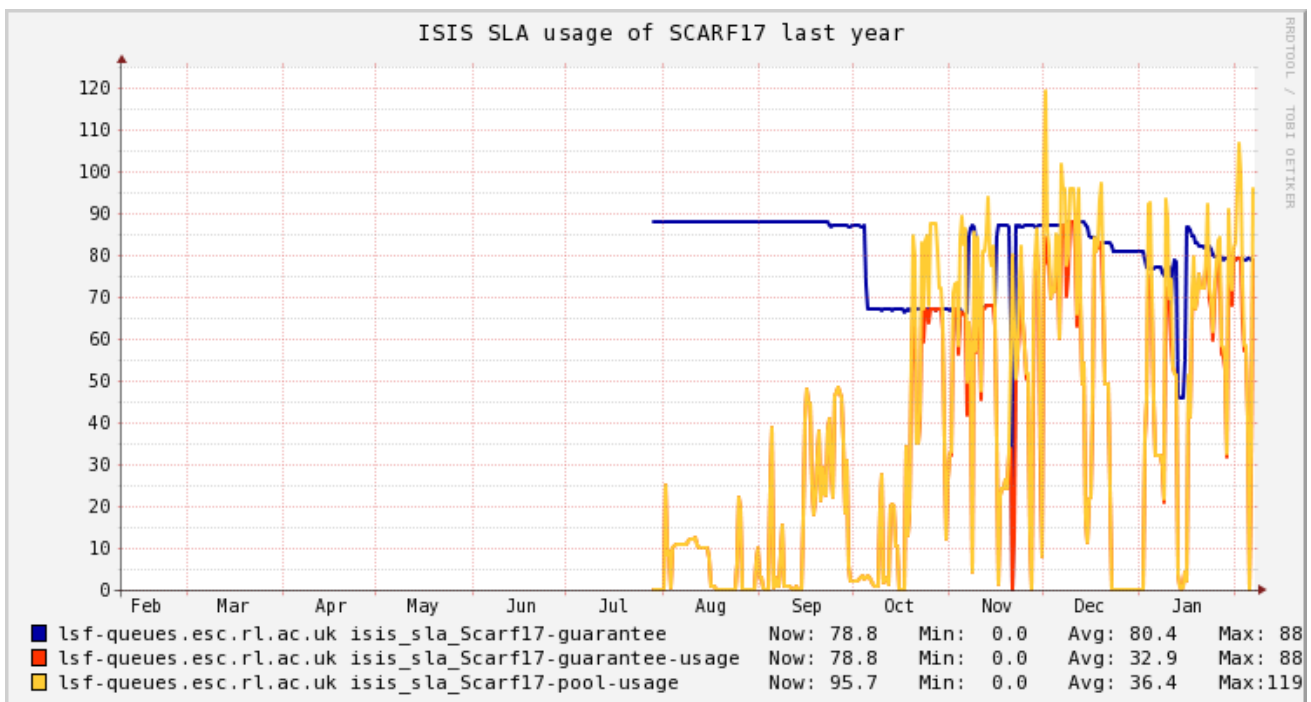

Figure 7.1.5: ISIS SLA Usage of SCARF 17

While initially usage of SCARF17 by ISIS is low, it rapidly ramps up in mid-October and is then frequently exceeding the guaranteed host count. The lower usage for other SLAs may reflect that

newer hardware is available and is more attractive to run as it is more performant and has more cores allowing for larger workloads.
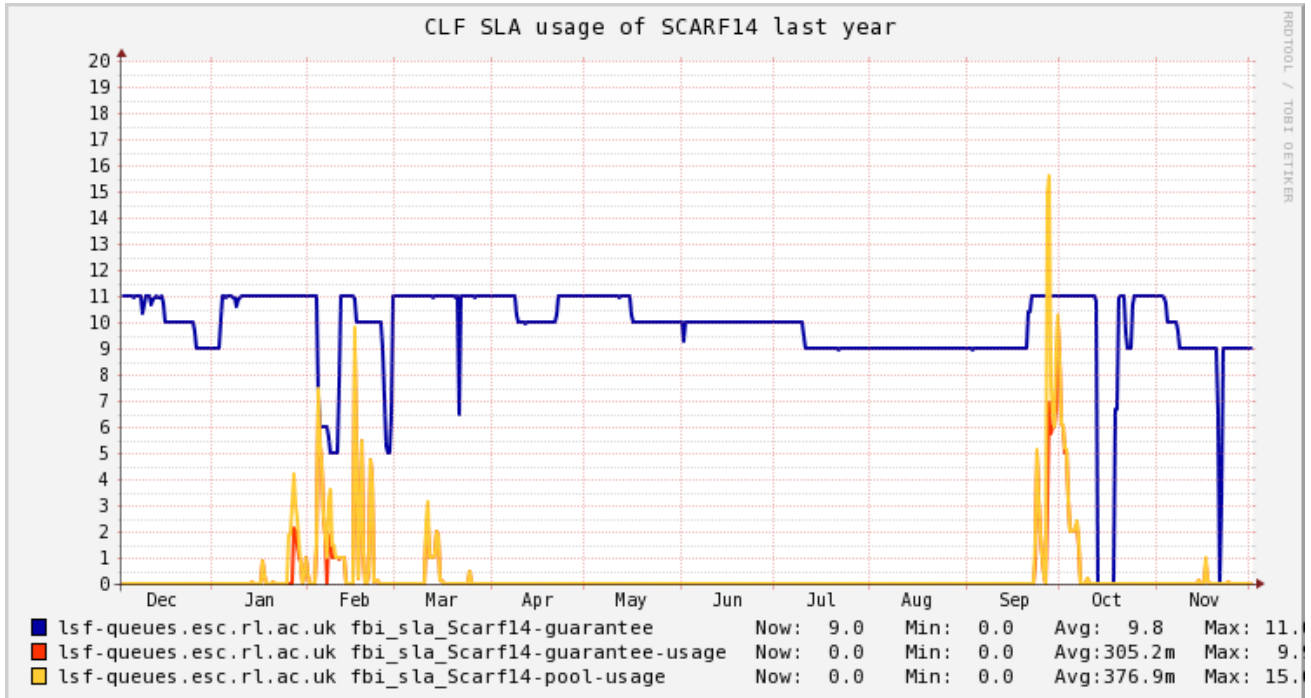

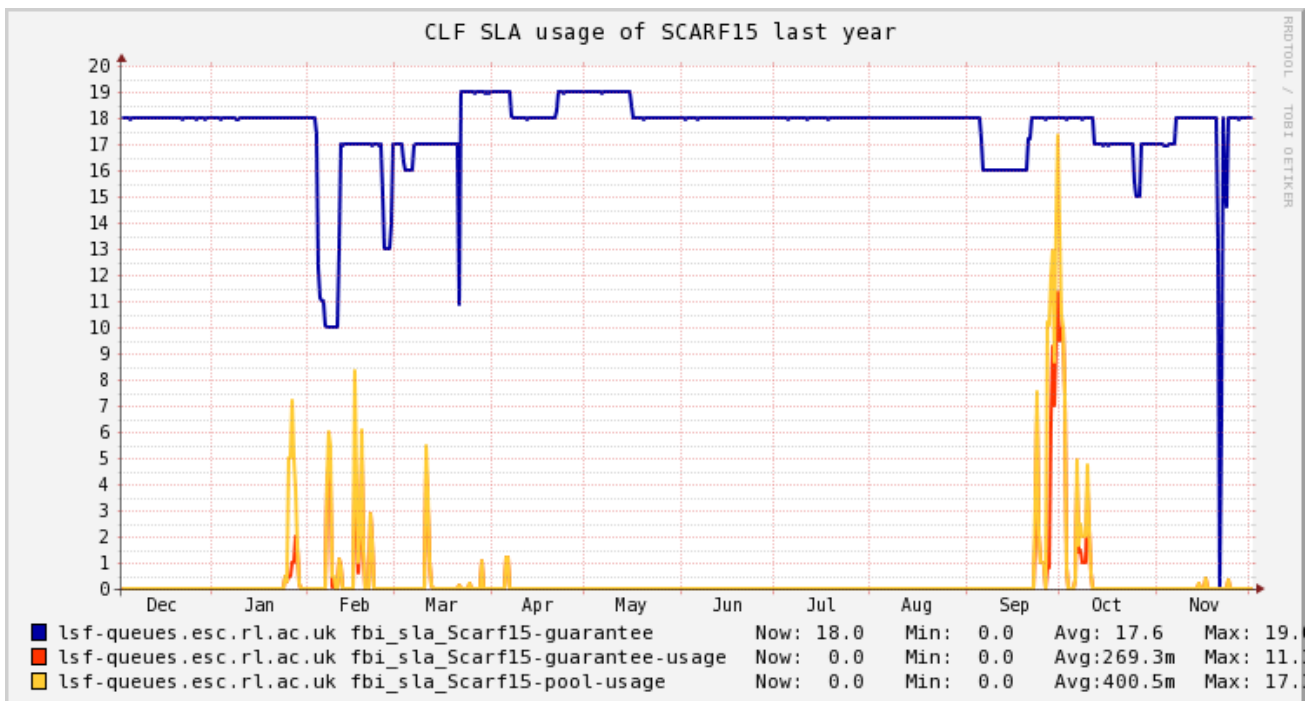**Figure 7.1.6: CLF SLA Usage of SCARF 14**

Figure 7.1.7: CLF SLA Usage of SCARF 15

The SCARF14 and SCARF15 plots for CLF FBI show that while they are not regularly making use of their guaranteed hosts, there have been some bursts of activity throughout the year.

7.2   MagnaCarta, Lexicon2 and DeRevolutionibus Queues

These queues are primarily for CLF Plasma Physics use. MagnaCarta has 480 cores purchased in 2016. Lexicon2 has 544 cores purchased in 2010. DeRevolutionibus is a new service based around 1608 cores purchased in 2017.
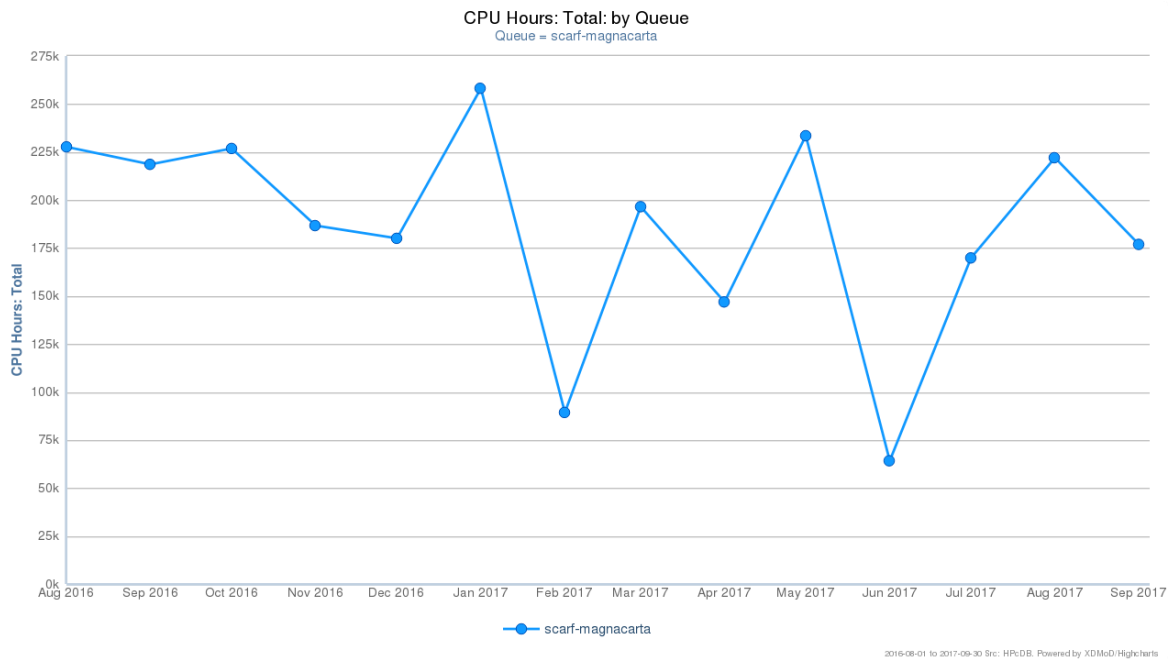

Figure 7.2.1: SCARF-MagnaCarta Usage

The graph for the SCARF-MagnaCarta queue shows significant usage, as it is available to CLF external collaborators.
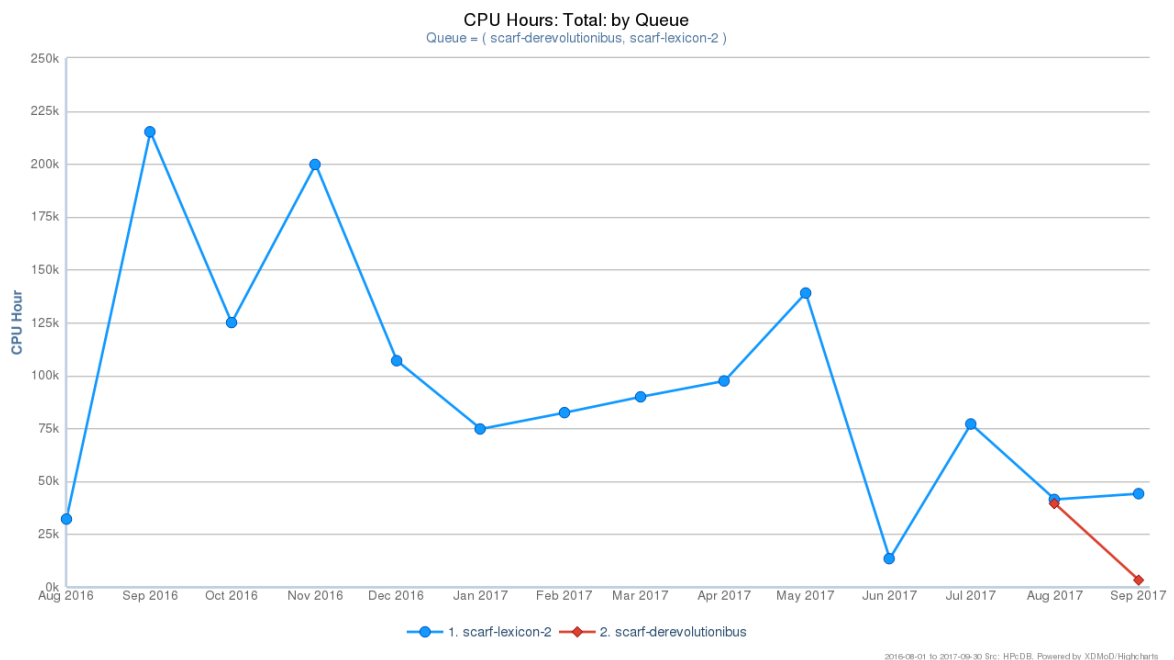

Figure 7.2.2: SCARF Lexicon-2 and DeRevolutionIbus Usage

SCARF-Lexicon-2 and DeRevolutionibus continue to be used for higher priority MagnaCarta users and on demand to support CLF experiments.

7.3   SCARF-IBIS

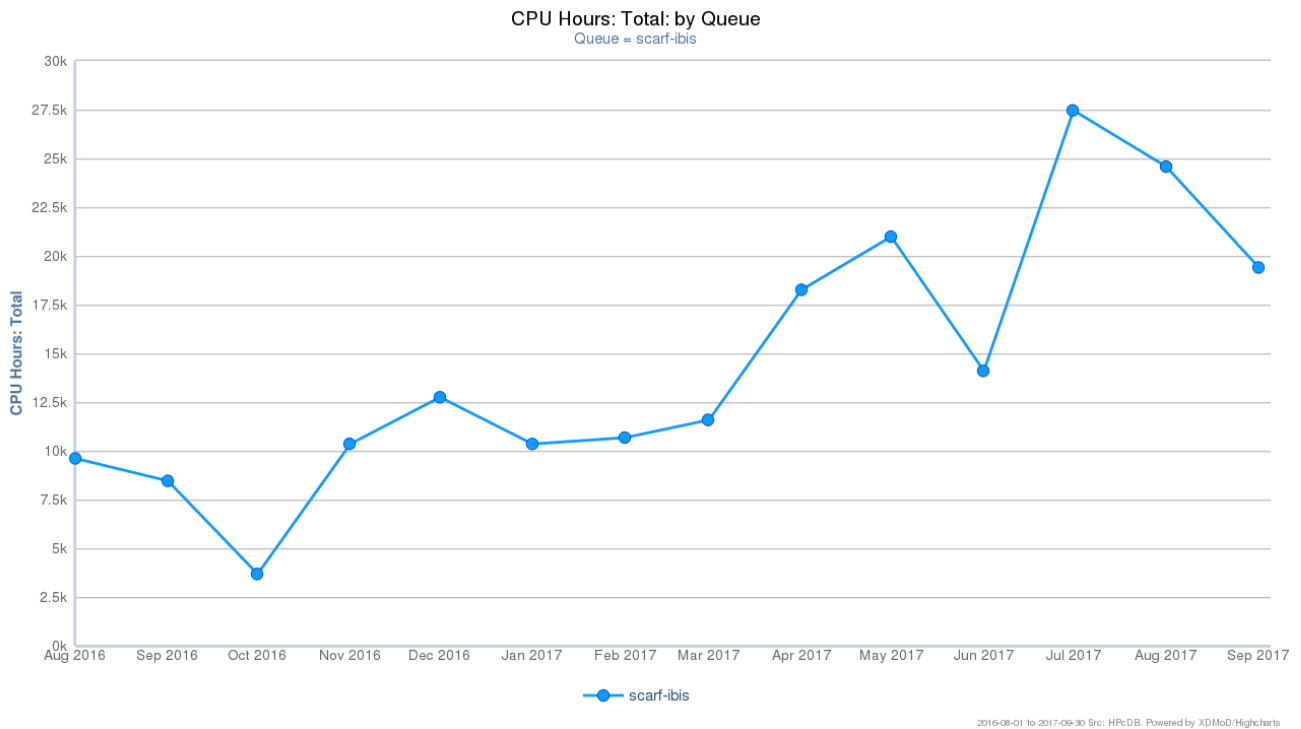SCARF-IBIS has a capacity of 240 CPU cores. They are used for the Intense Beams in Synchrotrons collaboration.

Figure 7.3.1: SCARF-IBIS Usage
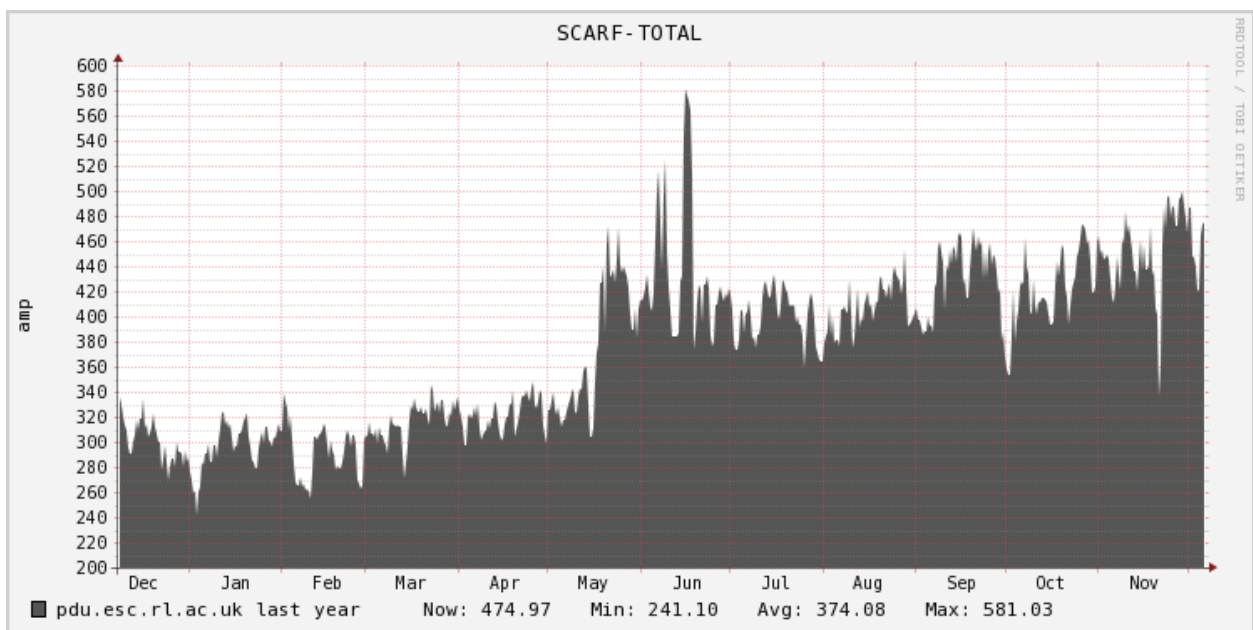
7.4   SCARF Total Power draw

Figure 7.4.1: SCARF Power Usage

The approximate average power draw of the SCARF cluster (including Lexicon) is about 375 amps or 90 kW. This excludes the power needed to cool, pump and move cold air. The efficiency of SCARF in terms in Gflops/W is giving in the table below.

Year Purchased	Gflops/W
2010	0.32
2011	0.48
2012	0.50
2013	0.59
2014	0.98
2015	1.95
2016	1.95
2017	5.26

Figure 7.4.2: GFlops/W for SCARF generations of equipment

From the above table it is clear that the Gflops/W achieved increase per generation of the SCARF equipment. This supports the continual refresh rate of SCARF hardware rather than a big bang approach. SCARF16 is the same hardware as SCARF15 which accounts for the identical Gflops/W.

7.5   Filesystem Usage

The plot below outlines the use of the Panasas filespace on the SCARF service. The filespace is shared across a number of projects therefore not all space is available to SCARF users, but SCARF users benefit as increasing the amount of space also increases the bandwidth to the storage as files are redistributed around the Panasas system automatically.
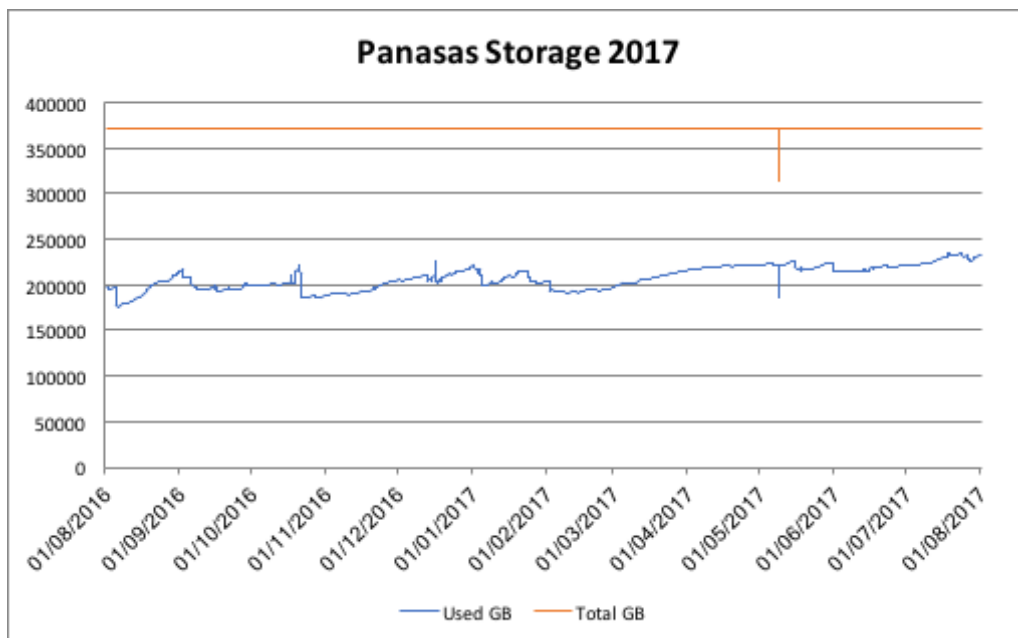
Figure 7.5.1: Filespace usage on the Panasas Storage

7.6   Networking

The diagram below shows the SCARF compute clusters embedded in the larger Research Infrastructure group's networking infrastructure. A change that has been taking place gradually has been the migration of SCARF equipment one step away from the core RIG network infrastructure to the switch labelled "HPC switch" in the diagram. This was necessary as the latest SCARF hardware now has faster host connections – up from 1 gigabit to 10 gigabit, which means that a faster uplink is required to cope with the greater bandwidth demands from that equipment. As the faster host connections will become the new default, additional network capacity was required.
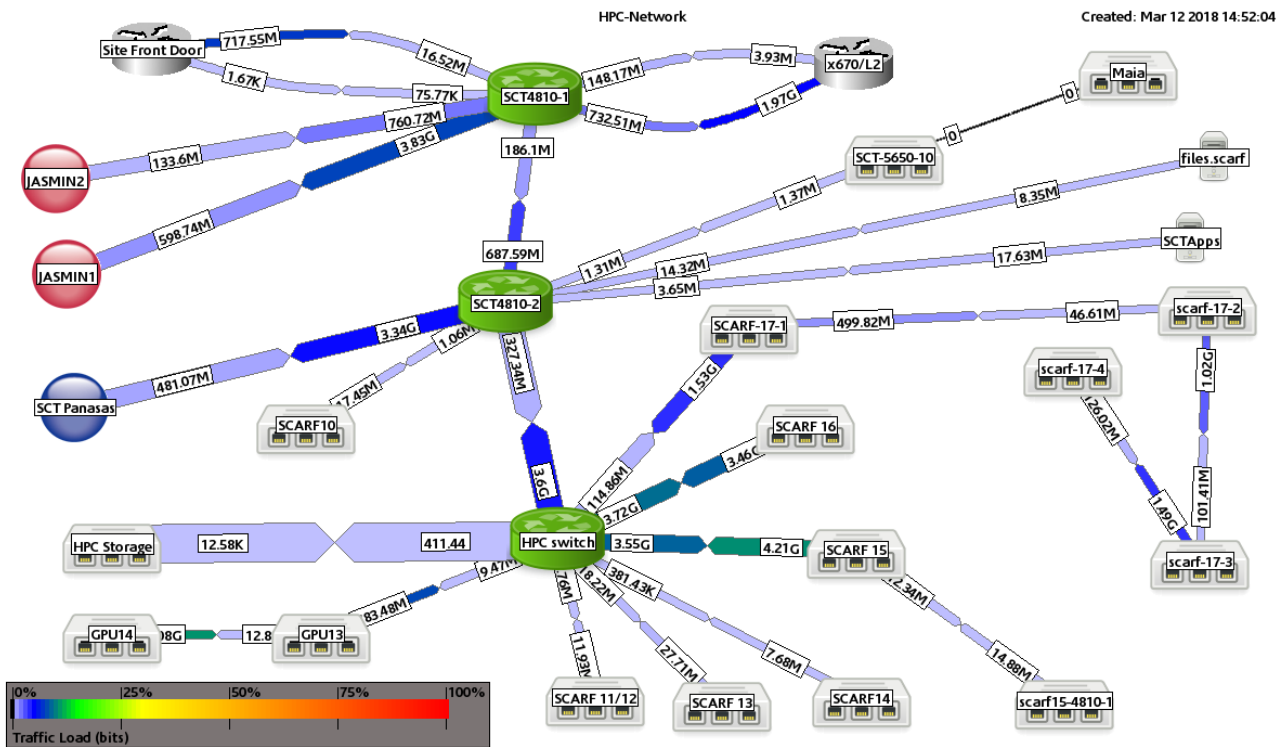

Figure 7.6.1: SCARF Network Topology

8. APPENDIX: SCARF DEVELOPMENTS

It has been a busy year for the SCARF service. Users' will have noticed most impact with the additional of capacity and upgrades to applications. However, a lot of effort goes into improving the management of SCARF.

8.1   Technical Developments

- In July 2017 the hardware tranche of dual Intel E5-2650v4, providing 1120 cores was made available.
- The SCARF service migrated to a new helpdesk system based on the RequestTracker software.
- The RHEL7 service was installed and configured using the Aquilon configuration management system, this should ensure that configuration skew between nodes is reduced.

8.2   Application Stack

A selection of new or updated applications is in the table below:

Application	Area	Version
Fluka	Monte Carlo simulation package for the interaction and transport of particles and nuclei in matter	2011.2c.6
GNU compiler	Fortran, C, C++ compilers and Maths libraries	6.2.0
PGI compilers	Fortran, C, C++ compilers and Maths libraries	17.5
CASTEP	Computational Chemistry	17.2.1
VSim	Electromagnetic, electrostatic, magnetostatic, and plasma simulations in the presence of complex dielectric, magnetic, and metallic shapes	8.0 & 8.1

A full list of the available software on SCARF can be found on the SCARF website:
http://www.scarf.rl.ac.uk/applications-libraries